



## 저작자표시-비영리-변경금지 2.0 대한민국

이용자는 아래의 조건을 따르는 경우에 한하여 자유롭게

- 이 저작물을 복제, 배포, 전송, 전시, 공연 및 방송할 수 있습니다.

다음과 같은 조건을 따라야 합니다:



저작자표시. 귀하는 원저작자를 표시하여야 합니다.



비영리. 귀하는 이 저작물을 영리 목적으로 이용할 수 없습니다.



변경금지. 귀하는 이 저작물을 개작, 변형 또는 가공할 수 없습니다.

- 귀하는, 이 저작물의 재이용이나 배포의 경우, 이 저작물에 적용된 이용허락조건을 명확하게 나타내어야 합니다.
- 저작권자로부터 별도의 허가를 받으면 이러한 조건들은 적용되지 않습니다.

저작권법에 따른 이용자의 권리는 위의 내용에 의하여 영향을 받지 않습니다.

이것은 [이용허락규약\(Legal Code\)](#)을 이해하기 쉽게 요약한 것입니다.

[Disclaimer](#)

공학박사학위논문

**터블의 운동에너지와 화염면 구김의 주요  
인자 분석에 기반한 불꽃 점화 엔진의  
0D 모델 개발**

**Development of a Comprehensive 0D Model for an SI Engine  
Based on the Analysis of the Kinetic Energy of Tumble and  
the Critical Factors for Flame Wrinkling**

2022 년 2 월

서울대학교 대학원

기계항공공학부

김 명 수

# 텀블의 운동에너지와 화염면 구김의 주요 인자 분석에 기반한 불꽃 점화 엔진의 0D 모델 개발

Development of a Comprehensive 0D Model for an SI Engine  
Based on the Analysis of the Kinetic Energy of Tumble and  
the Critical Factors for Flame Wrinkling

지도교수 송 한 호

이 논문을 공학박사 학위논문으로 제출함

2021 년 10 월

서울대학교 대학원

기계항공공학부

김 명 수

김명수의 공학박사 학위논문을 인준함

2021 년 12 월

위 원 장 : 민 경 덕 (인)

부위원장 : 송 한 호 (인)

위 원 : 임 홍 근 (인)

위 원 : 라 영 철 (인)

위 원 : 한 동 희 (인)

## **Abstract**

# **Development of a Comprehensive 0D Model for an SI Engine Based on the Analysis of the Kinetic Energy of Tumble and the Critical Factors for Flame Wrinkling**

**Myoungsoo Kim**

Department of Mechanical and Aerospace Engineering

The Graduate School

Seoul National University

Notwithstanding the continuous technological development of spark-ignition (SI) engines, the physics of in-cylinder phenomena has not been well clarified to date. Furthermore, the advent of diverse combustion technologies has increased difficulty in understanding these phenomena using existing analysis methods. Under those circumstances, the modeling based on fundamental physics becomes critical for analyzing the behavior of an SI engine. By means of the simulation built upon the fundamental physics, the understanding of the phenomena in the engine might be extended immensely, thereby contributing to optimizing engine designs and operations.

Unfortunately, there have been lots of modeling uncertainties in the numerical simulations of premixed turbulent flame. In three-dimensional (3D) simulations, the rigorous validation of turbulence and combustion models in an extensive range of operating conditions still remains a challenging task despite the remarkable evolution of computing power. By enhancing the accuracy of turbulence prediction, however, zero-dimensional (0D) simulations could be utilized as a powerful tool for validating the built-in models over numerous experimental data due to their incomparably fast computing speeds. Therefore, in this study, attempts are made to understand the underlying physics of in-cylinder phenomena by applying the 0D simulation with the proposed physics-based models, evidenced by a variety of direct numerical simulations and experiments to date. The dissertation mainly consists of two parts: turbulence and combustion models.

On the one hand, the proposed turbulence model is principally built upon the kinetic energy analysis of tumble, differing from the existing 0D turbulence models based on the angular momentum perspective of tumble. The analysis of tumble behavior is first presented. Then, an intake model capable of reflecting various intake manifold designs is established based on the analysis. The models for spinning up and vortex breakdown, well-known tumble behaviors critically affecting in-cylinder turbulence, are subsequently proposed. Therefore, this study develops the physics-based turbulence model accurately predicting a variety of modifications in the engines without changing any model constants; those variances include valve strategies (timing, duration, lift), cylinder geometries (connecting rod length, bore, stroke, compression ratio), manifold designs (valve diameter and port design), and engine operating conditions (intake manifold pressure and engine speed).

On the other hand, the proposed combustion model attempts to reproduce a vast majority of combustion behaviors revealed to date, such as differential diffusion, flame instabilities, cutoff scales, and distributed reaction. This study also suggests an expression for fully-developed turbulent flame speed by inspecting the factors which influence flame wrinkling. As a result, in conjunction with the proposed

turbulence model, the 0D simulation successfully predicted the combustion behavior of 245 experimental data points of four different SI engines including extremely lean gasoline/air mixture up to  $\phi=0.53$ . Furthermore, with the aid of continuously variable valve timing modules, the models were extensively validated over a wide range of thermodynamic conditions; the pressure and the calculated temperature of the unburned mixture at ignition timing are varied from 4.5-28.6 bar and 559-794 K, respectively.

Lastly, the analysis of combustion is conducted with the simulation embedding the developed models, thereby identifying several distinctive features of stoichiometric and lean-burn operating points. More specifically, the analysis helps to identify the critical factors for three flame development periods: the burn durations from ignition timing to CA10, CA10 to CA50, and CA50 to CA90. Above all, this study reveals the importance of the effect of inner cutoff on the early stage of flame propagation, differing from the conventional analysis of an SI engine that only concerns two factors: planar laminar flame speed and turbulent intensity.

**Keyword:** Zero-dimensional simulation, spark-ignition engine, tumble, turbulence model, premixed turbulent flame, combustion model

**Student Number:** 2016-20674

# Table of Contents

<b>Abstract...</b>	<b>i</b>
<b>Table of Contents .....</b>	<b>iv</b>
<b>List of Figures .....</b>	<b>vii</b>
<b>List of Tables .....</b>	<b>xv</b>
<b>Nomenclature.....</b>	<b>xvi</b>
<b>Chapter 1. INTRODUCTION.....</b>	<b>1</b>
1.1. Introduction to 0D simulation .....	1
1.1.1. 0D turbulence model .....	1
1.1.2. 0D combustion model .....	6
1.2. Reviews of in-cylinder phenomena.....	9
1.2.1. Behaviors of tumble .....	9
1.2.2. Premixed laminar flame .....	11
1.2.3. Premixed turbulent flame .....	13
1.3. Research objective and implication .....	15
1.4. Organization of the dissertation .....	16
<b>Chapter 2. FUNDAMENTAL STUDY OF TUMBLE</b>	
<b>    BEHAVIORS .....</b>	<b>18</b>
2.1. Methodology .....	18
2.1.1. Base setup for 3D simulation .....	18
2.1.2. Definition of tumble energy .....	21
2.2. The analysis of the intake of tumble energy .....	23

2.2.1.	Reverse tumble .....	23
2.3.	The analysis of the velocity field during the compression stroke .....	27
2.3.1.	The period between BDC and IVC .....	28
2.3.2.	The period between IVC and firing TDC .....	29
2.3.3.	Movement of the tumble center .....	32
2.4.	The analysis of tumble energy during the compression stroke .....	36
2.4.1.	Piston effect coupled with the viscous decay effect .....	38

## **Chapter 3. TURBULENCE MODEL .....45**

3.1.	Methodology .....	45
3.1.1.	Simulated cases .....	45
3.1.2.	The overall schematic of turbulence model .....	47
3.1.3.	Dependency of the turbulent properties on numerical schemes .....	49
3.2.	Intake model .....	51
3.2.1.	Determination of the effective flow area .....	51
3.2.2.	Loss coefficient .....	59
3.3.	Turbulence production model .....	67
3.4.	Spinning up model .....	71
3.5.	Result and discussion .....	77
3.5.1.	Sensitivity analysis of the validation constants .....	77
3.5.2.	Variable valve operation results .....	82
3.5.3.	Engine geometry results .....	84
3.5.4.	Engine operating condition results .....	87
3.5.5.	Comparison with GT-power .....	90

## **Chapter 4. COMBUSTION MODEL .....92**

4.1.	Methodology .....	92
4.1.1.	Experimental setup .....	92
4.1.2.	Simulation setup .....	95
4.1.3.	Laminar properties .....	98



4.1.4.	Simulation methodology .....	100
4.2.	Turbulence/flame interaction model .....	103
4.2.1.	Flame surface density (FSD) model.....	103
4.2.2.	Efficiency function and cutoff scales .....	107
4.2.3.	Distribution of turbulence .....	114
4.3.	Determination of turbulent flame speed.....	120
4.3.1.	Strained laminar flame speed .....	121
4.3.2.	Closure of the fully-developed turbulent flame speed .....	129
4.3.3.	Transition of the inner cutoff.....	140
4.4.	Flame/wall interaction model.....	141
4.4.1.	Influence zone model .....	142
4.4.2.	Hypothesis for the transient behaviors of flame thickness .....	147
4.5.	Result and discussion .....	153

## **Chapter 5. CRITICAL FACTORS FOR ENGINE**

### **COMBUSTION ..... 157**

5.1.	Influencing factors for BD0010 .....	157
5.2.	Additional analysis for BD1050 and BD5090 .....	162

## **Chapter 6. CONCLUSION..... 165**

### **BIBLIOGRAPHY..... 168**

### **국문 초록 ..... 182**

# List of Figures

<b>Figure 1.1</b> The description of in-cylinder acceleration profiles. ....	5
<b>Figure 2.1</b> Refined mesh during the intake stroke, with the contours of velocity magnitude. ....	20
<b>Figure 2.2</b> Engine geometry and coordinates. ....	20
<b>Figure 2.3</b> Intake valve lift profiles, tumble energy, and kinetic energy results of the reference case and low-maximum-valve-lift cases (2 mm and 3 mm). ....	25
<b>Figure 2.4</b> Velocity vector fields at 400 CAD, 450 CAD, and 500 CAD along the valve plane: (a) reference valve profile, (b) valve profile with a maximum valve lift of 3 mm, and (c) valve profile with a maximum valve lift of 2 mm. ( $l_v$ is instantaneous valve lift) ....	26
<b>Figure 2.5</b> Velocity vector fields across the central plane for the 1 mm intake valve open condition. ....	29
<b>Figure 2.6</b> Velocity vector fields in the central plane for the closed intake valve condition. ....	31
<b>Figure 2.7</b> Distortion of tumble velocity from the reference case: (a) 600 CAD and (b) 660 CAD. ....	31
<b>Figure 2.8</b> Bore-to-height ratio and the kinetic energy ratio between the x-direction and y-direction for the reference case. ....	32

<b>Figure 2.9</b> Virtual velocity fields before IVC during the compression stroke: (a) tumble velocity, (b) piston-induced velocity, and (c) resultant velocity. ....	34
<b>Figure 2.10</b> Virtual velocity fields after IVC during the compression stroke: (a) tumble velocity, (b) piston-induced velocity, and (c) resultant velocity. ....	34
<b>Figure 2.11</b> Intake valve lift profiles with different IVC timings. ....	35
<b>Figure 2.12</b> Velocity vector fields across the valve plane: (a) tumble velocity at BDC, (b) resultant velocity at 630 CAD for the IVC 600° case, and (c) resultant velocity at 630 CAD for the IVC 660° case. ....	36
<b>Figure 2.13</b> Velocity vector fields at the TDC: (a) resultant velocity for the IVC 600° case, (c) resultant velocity for the IVC 660° case. ....	36
<b>Figure 2.14</b> Accumulated energy and piston acceleration in the reference case. ...	38
<b>Figure 2.15</b> Velocity and acceleration vectors along the line parallel to the x-direction. ....	41
<b>Figure 2.16</b> Kinetic energy and accumulated energy with different values of $C_{\mu}$ . ..	44
<b>Figure 2.17</b> Mass-specific angular momentum, tumble energy, and turbulent kinetic energy under different IVC conditions. ....	44
<b>Figure 3.1</b> Schematic of the kinetic energy flow in the 0D model. ....	48
<b>Figure 3.2</b> Integral length scale, tumble energy, and turbulent intensity obtained from different numerical schemes. ....	50

<b>Figure 3.3</b> Steady CFD simulation with the valve curtain area divided into four regions: red (division 1), yellow (division 2), green (division 3), and blue (division 4). .....	53
<b>Figure 3.4</b> Discharge coefficient (a) and fractions of mass flow rate (b) at the fixed valve lifts obtained from the steady CFD simulation (Reference case). .....	54
<b>Figure 3.5</b> Velocity vector fields at various valve lifts (2 mm, 6 mm, 10 mm) with the engine geometry of the reference case. ....	57
<b>Figure 3.6</b> Comparison of the effective flow areas obtained from different port designs. The solid lines and markers indicate the quantities obtained from the 0D and CFD simulations, respectively, with the assumption of cutoff velocity. ....	59
<b>Figure 3.7</b> Dissipation rate at different valve lifts (2 mm, 6 mm, and 10 mm) with the engine geometry of the reference case. ....	63
<b>Figure 3.8</b> The fractions of accumulated kinetic energy intake from the 0D simulation (left) and the first peaks of tumble energy for the 3D CFD and 0D simulations (right): (a) 0D results with loss coefficient in Eq. (3.14), (b) 0D results with a single tuning constant. ....	65
<b>Figure 3.9</b> 3D virtual velocity fields (modified barrel swirl) for the turbulence production model. Each cylinder height is 80 mm (left) and 30 mm (right), and the bore is 75.6 mm. The colors in the scale bar indicate the relative magnitudes of velocity normalized by the maximum velocity. ....	70

<b>Figure 3.10</b> Accumulated energy and spinning up after IVC at the reference case obtained from 3D CFD.....	71
<b>Figure 3.11</b> One-dimensional velocity profiles along the line parallel to the x-direction. ....	73
<b>Figure 3.12</b> Comparison of the accumulated quantities of spinning up obtained from the 3D CFD and 0D simulations. ....	77
<b>Figure 3.13</b> Comparison of tumble energy and turbulent intensity for the reference case.....	78
<b>Figure 3.14</b> Tumble energy and turbulent intensity results with validation constants ( $C_{ex}$ , $C_{non}$ , $C_{rot}$ ) multiplied by weight factors. ....	80
<b>Figure 3.15</b> Tumble energy and turbulent intensity of the 0D simulation at different validation constants ( $C_l$ , $C_{prod}$ , $C_{spin}$ , $C_{out}$ ) multiplied by weight factors.....	81
<b>Figure 3.16</b> All valve profiles explored in this study. Solid and dashed lines indicate valve profiles in the reference case and the intake valve profiles in cases 2-12, respectively. ....	82
<b>Figure 3.17</b> Tumble energy (2nd column) and turbulent intensity (3rd and 4th columns), obtained from the 3D CFD and 0D simulations at various intake valve lift profiles. 1st row: cases with different IVC, 2nd row: cases with different IVO, 3rd and 4th rows: cases with different valve lifts.....	84

**Figure 3.18** Tumble energy (2nd column) and turbulent intensity (3rd and 4th columns), obtained from the 3D CFD and 0D simulations with various engine geometries. 1st row: cases with different connecting rods, 2nd row: cases with different strokes, and 3rd row: cases with different intake port designs. ....86

**Figure 3.19** Tumble energy (2nd column) and turbulent intensity (3rd and 4th columns), obtained from the 3D CFD and 0D simulations for different engine operating conditions. 1st row: cases with different intake manifold pressures, 2nd row: cases with different engine speeds. ....89

**Figure 3.20** Averaged turbulent intensity using crank angle during  $700^\circ$  (bTDC  $20^\circ$ )~ $720^\circ$ (TDC). ....91

**Figure 4.1** Operating ranges of temperature, pressure, and residual mass fraction at ignition timing. ....102

**Figure 4.2** Combustion regime diagram for a premixed turbulent flame.  
(a) Conditions of all operating points at ignition timing and (b) example cases (Engines A and D) for the trajectory of the condition during combustion. ....102

**Figure 4.3** Efficiency functions in previous studies at different length ratios ( $r/\delta_L$ ) and velocity ratios ( $v/S_L^0$ ). (a):  $v/S_L^0 = 0.5$ , (b):  $v/S_L^0 = 5.0$ . ....113

**Figure 4.4** Comparison of BD0010 with a total of 245 points for four different engines. The abscissa and ordinate indicate BD0010 obtained from the 0D simulation and experiment, respectively. ....113

**Figure 4.5** The distribution of in-cylinder turbulence at the reference case. The leftmost figure shows the distributions of turbulent kinetic energy cut through the x-y and y-z planes at firing TDC. The markers and dotted lines in the middle and rightmost figures indicate the average turbulent intensities at the plane perpendicular to the respective directions and  $u'_{avg}$ , respectively. .... 115

**Figure 4.6** The standard deviations (dashed line) of turbulent intensity and volume-averaged turbulent intensities (solid line) at various engine operating cases. (a) Different IVC timings, (b) engine geometries, and (c) engine speeds. The numbering of cases is listed in Table 3.1. .... 117

**Figure 4.7** Turbulent intensities and mass fraction burned. Detailed explanations regarding the terms are presented in the main body of the paper. .... 120

**Figure 4.8** 0D simulation results for the laminar flame speeds ( $S_L^0$ ,  $S_L$ , and  $S_{L,mod}$ ) at the left ordinates and the reaction zone Karlovitz number ( $Ka_r$ ) at the right ordinates. (a) One instance for the stoichiometric point with Engine A, and (b) one instance for the lean-burn point with Engine D. .... 128

**Figure 4.9** Coefficient of determination (leftmost) and the slope of regression lines (middle) from the simulation results of stoichiometric points at different sets of ( $C_1$ ,  $C_2$ ). The rightmost figure shows the one instance: ( $C_1$ ,  $C_2$ ) = (0.7, 0.3). .... 134

**Figure 4.10** Comparison of BD1050s obtained from the experiment and simulation results. The right and left figures show the stoichiometric and lean-burn points, respectively. .... 137

<b>Figure 4.11</b> Coefficient of determinations at different sets of validation constants ( $C_1$ , $C_3$ ). The value of $C_2$ is fixed at 0.3 and 0.4 in (a) and (b), respectively. ....	139
<b>Figure 4.12</b> Comparison of BD1050s obtained from the experiment and simulation results using exponents ( $C_1$ , $C_2$ , $C_3$ ) as (0.8, 0.4, 2.0). ....	139
<b>Figure 4.13</b> Comparison of the $\delta L$ and $8\eta$ values at all operating points considered in this study. The position in the abscissa indicates the relative timing during each burn duration period. ....	141
<b>Figure 4.14</b> Description of the flame/wall interaction. The wrinkling factor ( $\mathcal{E}$ ) is plotted alongside the distance from the wall ( $d$ ). ....	142
<b>Figure 4.15</b> Description of the outer and inner flame surfaces with the boundary of the influence zone. ....	146
<b>Figure 4.16</b> Correlations with BD5090 and combustion properties. (a) Pressures obtained from experiments, (b) products of the flame power at MFB50 and the Zel'dovich flame thicknesses. ....	148
<b>Figure 4.17</b> Comparison of BD5090s obtained from experimental and simulation results. ....	152
<b>Figure 4.18</b> Comparison of the experiment and simulation burn duration results. (a) BD0010, (b) BD1050, and (c) BD5090. ....	155



**Figure 4.19** Comparison of the engine performance parameters of the experimental and simulation results. (a) Net indicated thermal efficiency, (b) indicated specific fuel consumption, and (c) indicated mean effective pressure. .... 156

**Figure 5.1** Sensitivity analysis of BD0010 with varying designated variables. (a)  $S^{\theta}_L$ , (b)  $\delta^{\theta}_L$ , (c)  $u'$ , and (d)  $P$ ..... 159

**Figure 5.2** Normalized BD0010 at the unperturbed case obtained through the sensitivity analysis of four different variables. .... 160

**Figure 5.3** One instance for the evolution of wrinkling factor during BD0010 with varying  $S^{\theta}_L$ ,  $\delta^{\theta}_L$ ,  $u'$ , and  $P$  factors. The left and right figures show the variations resulting in enhanced and lowered flame propagation speeds, respectively. .... 161

**Figure 5.4** Normalized wrinkling factors by their equilibrium values with the flame radius as the abscissa. (a) All cases of Engine A and their average profile, and (b) average profiles of normalized wrinkling factors. .... 162

**Figure 5.5** Correlation of BD5090 with the Zel'dovich flame thickness at the ignition timing  $\delta^{\theta}_{L,ign}$  and the averaged flame power over BD5090  $Q_{\Sigma,BD5090}$ . The dotted lines indicate the contours where the products of  $\delta^{\theta}_{L,ign}$  and  $Q_{\Sigma,BD5090}$  have identical values..... 164

## List of Tables

<b>Table 2.1</b> Reference engine operating conditions .....	21
<b>Table 3.1</b> Simulated cases in this study.....	46
<b>Table 3.2</b> Discharge coefficients for the valve curtain area and valve area at different port designs.....	56
<b>Table 3.3</b> Validation constants used in the model.....	78
<b>Table 4.1</b> Engine specifications and operating conditions.....	94
<b>Table 4.2</b> Closure forms of turbulent flame speed from experimental studies. $P^0$ and $T^0$ denote the reference values for pressure and unburned zone temperature, respectively. Exact values are referred to in the literature.....	130

# Nomenclature

## Latin

$A$	area	$D_{i,\text{mix}}$	mass diffusivity of unburned mixture
$A_{\text{eff}}$	effective flow area	$E_{11}$	one-dimensional energy spectrum
$A_L$	unwrinkled flame surface	$\hat{\mathbf{F}}$	force
$A_{L,\text{in}}$	inner unwrinkled flame surface	$f_p$	Pao spectrum
$A_{L,\text{out}}$	outer unwrinkled flame surface	$H$	cylinder height
$A_l$	valve curtain area	$\Delta H_f$	heat of combustion
$A_T$	wrinkled flame surface	$I$	moment of inertia
$A_v$	valve area	$I_{\text{eff}}$	efficiency parameter
$\hat{\mathbf{a}}$	acceleration	$\hat{\mathbf{i}}, \hat{\mathbf{j}}, \hat{\mathbf{k}}$	unit vectors in Cartesian coordinates
$B$	cylinder bore	$K$	kinetic energy, mean kinetic energy
$C$	efficiency function	$K_{\text{loss}}$	dissipated energy
$C_{d,l}$	discharge coefficient at valve curtain area	$K_{\text{rot}}$	tumble energy
$C_{d,v}$	discharge coefficient at valve area	$K_{\text{spin}}$	increased energy by spinning up
$C_{\text{loss}}$	loss coefficient	$Ka$	Karlovitz number
$c$	progress variable	$Ka_{\text{lam}}$	laminar Karlovitz stretch factor
$D$	valve diameter	$Ka_r$	reaction zone Karlovitz number
$D_2, D_3$	fractal dimensions		
$D_{ij}$	mass diffusivity		

$Ka_{\text{turb}}$	turbulent Karlovitz stretch factor	$\bar{Q}_{\Sigma, \text{BD5090}}$	average flame power during BD5090
$k$	turbulent kinetic energy	$Re_l$	Reynolds number ( $= 4u'l_t/(S_L^0 \delta_L^0)$ )
$k_{\text{rot}}$	turbulence production from tumble energy	$r$	vortex size, radial distance from the geometric center of cylinder
$k_{\text{nonrot}}$	turbulence production from non-tumble energy	$\hat{\mathbf{r}}$	distance vector from cylinder's volume center
$L_b$	Markstein length	$r_f$	flame radius
$Le$	Lewis number	$S_L$	stretched laminar flame speed
$Le_{\text{eff}}$	effective Lewis number	$\bar{S}_L$	strained laminar flame speed
$Le_{i, \text{mod}}$	Lewis number for species $i$ with Ka effect	$\bar{S}_{L, \text{mod}}$	strained laminar flame speed with Ka effect
$l_t$	integral length scale	$S_L^0$	planar laminar flame speed
$l_v$	valve lift	$S_T$	turbulent flame speed
$\mathbf{M}$	angular momentum	TR	tumble ratio
Ma	Markstein number	$T^0$	crossover temperature
$m$	mass	$T_b$	burned gas temperature
$m_{\text{out}}$	backflow mass	$T_{\text{ph}}$	preheat zone temperature
$n$	correcting factor	$T_u$	unburned gas temperature
$n_v$	number of valves	$t$	time
$\hat{\mathbf{n}}$	normal vector to the flame front	$U$	maximum x-dir speed at modified barrel swirl
$P$	in-cylinder pressure	$U_d$	displacement speed
Pe	Peclet number		
$Q_w$	wall heat flux at quenching		
$Q_{\Sigma}$	flame power		

$U_x, U_y, U_z$	velocity components for modified barrel swirl	$y_c$	y-coordinate of the cylinder volume center
$U_{y,m}$	maximum y-dir speed at modified barrel swirl ( $=U \cdot H/B$ )	$y_i$	mass fraction of species $i$
$\hat{\mathbf{u}}$	local velocity	$y_f$	mass fraction of fuels
$u'$	turbulent intensity at the location of flamelet	$Ze$	Zel'dovich number
<b>Greek</b>			
$u'_{\text{avg}}$	cylinder-averaged turbulent intensity ( $=\sqrt{2k/3m}$ )	$\alpha$	thermal diffusivity of unburned gas
$u'_{\text{flame}}$	average turbulent intensity within the flame thickness obtained from 3D CFD	$\alpha_i$	thermal diffusivity of species $i$
$V$	volume	$\Gamma$	integrated straining efficiency
$V_{\text{cyl}}$	cylinder volume	$\gamma$	specific heat ratio
$V_{\text{def}}$	deformed volume	$\delta_{\text{inf}}$	influence zone thickness
$v$	vortex speed	$\delta_L$	laminar flame thickness
$\hat{\mathbf{v}}$	velocity vector, resultant velocity	$\delta_L^0$	Zel'dovich flame thickness
$\hat{\mathbf{v}}_p, v_p$	piston-induced velocity, piston speed	$\delta'_L$	flame thickness defined by temperature
$\hat{\mathbf{v}}_t$	tumble velocity	$\delta_q$	quenching zone thickness
$\mathbf{w}_e$	engine angular velocity	$\delta_r$	reaction zone thickness ( $\sim\delta_L/2$ )
$X_b$	mass fraction burned	$\varepsilon$	dissipation
$x, y, z$	spatial coordinates	$\varepsilon_c$	inner cutoff scale
$x_i$	mole fraction of species $i$	$\varepsilon_o$	outer cutoff scale
		$\eta$	Kolmogorov length scale at unburned gas

$\eta_r$	Kolmogorov length scale at burned gas	in	intake
$\kappa$	wavenumber	inf	influence zone
$\bar{\kappa}$	nondimensional wavenumber	nonrot, non	non-tumble
$\kappa_s$	stretch rate	max, min	maximum, minimum
$\mathcal{E}$	wrinkling factor	$q$	quenching zone
$\mathcal{E}_{eq}$	equilibrium value of wrinkling factor	rot	tumble
$\lambda$	Taylor microscale	$u$	unburned gas
$\nu$	kinematic viscosity	$x, y, z$	spatial coordinates
$\nu_t$	turbulent viscosity		
$\phi$	equivalence ratio		
$\rho$	density		
$\bar{\Sigma}$	flame surface density		
$\sigma$	expansion ratio		

### ***Subscript***

$b$	burned gas
cum	cumulative quantity
den	density-related
ex	exhaust
ext	externally induced
$i$	$i$ -th component, species $i$
ign	ignition timing

# Chapter 1. INTRODUCTION

## 1.1. Introduction to 0D simulation

### 1.1.1. 0D turbulence model

Although various factors influence flame wrinkling, turbulence is undeniably involved in a vast majority of the production of wrinkled flame surfaces. In that respect, a turbulence model is of vital importance for determining flame propagation speed in numerical simulations. The intrinsic shortcoming of zero-dimensional (0D) simulations, however, lies in the uncertainties of local properties, e.g., turbulence. Therefore, numerous researches have been performed to enhance the predictability of turbulence in 0D simulations until the present. Herein, several representative studies of a 0D turbulence model will be introduced.

Borgnakke et al. [1] suggested an earlier form of the  $k$ - $\epsilon$  model applicable to a 0D scheme, which is a two-equation model for the dissipation of turbulence. They further derived the turbulence production term, occasionally denominated as “rapid distortion theory term,” with the assumptions regarding compressibility. This term is also consistent with the  $k$ - $\epsilon$  model proposed by T. Morel and Mansour [2], which accounts for the rapid compression of engines. Meanwhile, Mansouri et al. [3] proposed a one-equation model for the dissipation of turbulence by utilizing the common transfer expression of energy cascade. Specifically, this model does not necessitate an additional differential equation for solving dissipation contrary to the two-equation model. To date, the aforementioned two dissipation models have been used consistently in 0D simulations.

As for the turbulence production model, which is the energy transfer from mean to turbulent kinetic energy, various efforts have been made to accurately determine the total production of in-cylinder turbulence despite the inherent difficulty of 0D simulation in predicting the turbulence production of three-dimensional (3D) flow structure. Particularly, there have been two representative models for turbulence production until recently.

On the one hand, several studies have directly considered in-cylinder flow structure by establishing a virtual velocity field in determining turbulence production. Benjamin [4, 5] first proposed the equations of the velocity field, the so-called “barrel swirl,” resembling the structure of tumble and obtained the turbulence production thereof. Since then, this model [4, 5] has been frequently utilized in subsequent studies with various intake models. For instance, applying Benjamin’s turbulence production model, Achuth and Mehta [6] developed an intake model which uses the moment arm of intake gas reflecting the pentroof structure of SI engines. Furthermore, Ramajo et al. [7] considered the velocity distribution around the intake valve with the identical turbulence production model. More recently, Kim et al. [8] modified the equations of the barrel swirl in order to satisfy the mass conservation of in-cylinder gas, thereby reproducing the high decaying rate of tumble at the latter part of the compression stroke. Therefore, this modified model was able to reproduce the rapid decaying of tumble during compression, called the “vortex breakdown.”

On the other hand, Grasreiner [9] developed the turbulence production model which employs the “decaying function” obtained from 3D computational fluid dynamics (3D CFD). The decaying function determines the amount of turbulence production of tumble as a function of the length ratio, which is the instantaneous height to the cylinder bore. Specifically, this function imposes higher turbulence



production at the lower length ratio (corresponding to the latter part of the compression stroke), thereby reproducing the vortex breakdown. Besides, it is worth noting that similar concepts with the decaying function have been utilized in recent studies for determining turbulence production [10-12].

Under those circumstances, the present study makes use of the one-equation model for the dissipation of turbulence and the modified barrel swirl model for turbulence production. The reason for determining the one-equation model, to briefly explain, is associated with the dependency of turbulence properties on numerical schemes. The detailed rationale behind the determination is elaborated in the main body of the paper. In the aspect of turbulence production, this study employs modified barrel swirl model in two reasons. First, this model does not require an additional implementation of 3D CFD, contrary to the decaying function, thus reducing a computational cost. Second, since it is capable of replicating a 3D tumble structure and the turbulence production thereof, the author believes this method holds more physical implications than utilizing decaying function.

The evaluation of tumble strength is of great importance for establishing a turbulence model since tumble is a predominantly applied flow structure in SI engines. In the literature, a vast majority of 0D turbulence models [4-7, 10, 11, 13, 14] have interpreted tumble with an angular momentum perspective, i.e., preserving the angular momentum of tumble if excluding viscous dissipation. Therefore, the mean kinetic energy of tumble could increase during compression by shortening the moment arm accompanying the velocity increase, thereby reproducing the so-called “spinning up” phenomenon. Based on this perspective, various attempts have been made to develop the turbulence model applicable for engine parameters, such as valve strategies [10, 13], intake port designs [14], and stroke-to-bore (S/B) ratios [10, 13]. Besides, fairly good agreements with 3D CFD were obtained in these studies.

However, to the best of the author's knowledge, limitations still exist in those models since fine-tunings of the validation constants with little physical meaning were necessitated to reflect the variances of engine designs. Besides, a limited number of valve profiles were utilized for validating those models, insufficient to ensure universal applicability in various valve profiles; there is a discrepancy between the validated profiles and commonly applied profiles with variable valve actuation technologies. The author believes that the limitations stem from the reflections of tumble behaviors owing to the theory deficient in physics.

In order to preserve the angular momentum of tumble, all in-cylinder gas components should receive the centripetal forces directing towards the geometric center. Note that we are not addressing the angular momentum of individual components but the total quantity of the angular momentum of tumble. It is obvious to note that the gas with rotating motion retains the centripetal force. That being said, the point is whether all gas components are subject to centripetal forces that are inversely proportional to the moment arms, the distances between the components and the center, or not. To claim that the angular momentum of tumble is preserved, one needs to demonstrate that all gas components receive the centripetal forces, thereby forming a complete elliptic streamline. This is because the change in kinetic energy of the in-cylinder gas during compression is intimately related to the force exerted on the gas. Otherwise, the increase in kinetic energy during the compression stroke will not be equivalent to the required energy for preserving the total quantity of the angular momentum of tumble. For instance, provided a streamline of tumble is partially rounded (i.e., not a complete elliptic streamline) such that the center of rotation of the rounded components does not coincide with the geometric center, the angular momentum of tumble along the streamline need not be preserved during

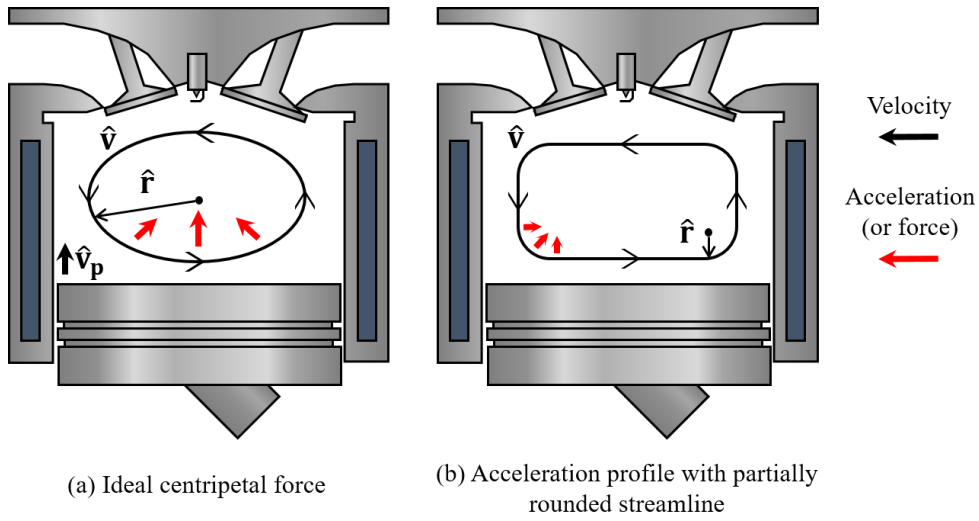


**Figure 1.1** The description of in-cylinder acceleration profiles.

compression. Figure 1.1 illustrates the example picture of the aforementioned statements. Considering the lack of verification of the phenomenon, we thus cannot assert that the theory is valid.

Inaccuracies can occur in two aspects when adopting the theory to a 0D model unless the theory is valid. First, when evaluating tumble as angular momentum quantity during the intake stroke, the moment arm utilized for calculating the amount of tumble intake can lead to an inaccurate prediction. This is because the moment arm is predominantly determined by engine geometry, having little to do with the properties of intake gas. Particularly, the misprediction can be pronounced in the case of various engine designs and valve strategies, whose intake characteristics differ significantly from each other. Second, as mentioned earlier, the actual change in kinetic energy during compression will not be identical to that required for preserving the total angular momentum of tumble. Since the 0D models adopting the theory interpret tumble as angular momentum quantity, tumble by itself enhances its own strength during compression by decreasing the moment of inertia and

simultaneously increasing angular velocity in those models. This can explain the phenomenological charge motion to a certain extent but lacks reflecting the factual cause of the spinning up, which is mostly due to the interaction of the in-cylinder charge motion and the piston acceleration. Accordingly, it can result in an inaccurate prediction on the amount of spinning up during compression.

Therefore, the turbulence model herein does not follow the angular momentum theory, and it is built upon the kinetic energy analyses of tumble previously conducted by Kim and Song [15]. With the aid of the earlier work, the models for spinning up and vortex breakdown are newly developed. As a consequence, the proposed physics-based model accurately predicts the variances of numerous engine parameters without changing any validation constants.

### **1.1.2. 0D combustion model**

As for 0D simulations, three combustion models have been representatively studied to the present: entrainment model (or eddy burn-up model) [16-20], fractal model [17, 21, 22], and flame surface density (FSD) model [23-26]. Note that, apart from those models including physical features of combustion, the celebrated Wiebe function [27] has been prevalently used for reproducing the combustion in SI engines. However, the author will not further address this function due to its deficiency in physics and the incapability of predicting combustion. Therefore, this section introduces only the three 0D combustion models mentioned earlier.

Blizard and Keck [16] first proposed the entrainment model wherein the flame front propagates and entrains an unburned gas at a designated speed. Although subsequent studies mostly utilized turbulent flame speed for the entrainment speed, typically with a classical expression proposed by Damköhler [28], this original

model correlated the flame speed with inlet gas velocity. Further, the entrained gas is burned at the speed of characteristic time, defined as the ratio of characteristic eddy radius to planar laminar flame speed. Due to its intriguing feature of entrainment similar to flame thickness, this model has been widely applied to various 0D simulations [1, 18-20] until recently notwithstanding the lack of experimental validation of the entrainment phenomenon [17].

Meanwhile, the fractal model has been studied consistently, which posits the fractal nature of flame morphology. Based on the assumption, the model attempts to predict the wrinkled flame surface using a fractal dimension. More precisely, it presumes the recursive self-similarity of the flame geometry within the length scales ranging from an outer cutoff and an inner cutoff. Since this concept has intrigued numerous researchers, a variety of fundamental studies have been performed to unveil the fractal nature of turbulent combustion experimentally [29-32] and numerically [33-35].

Built upon the fractal theory, the flame propagation speed has been diversely reproduced in 0D simulations. Since the model is exclusively dedicated to fully-developed turbulent flame speed, Santavicca et al. [22] used the additional factor to reproduce the transitional phase (laminar to turbulent). Specifically, this factor weakens the flame propagation speed by the competition of laminar burning and turbulent intensity. Therein, the inner cutoff and the outer cutoff were chosen to be the Kolmogorov length scale and integral length scale, respectively. Afterward, Bozza et al. [21] complemented the model to improve the predictability of early flame propagation speed by introducing additional terms, whereas Bellies et al. [17] utilized a similar model with some modification.

The FSD model has been widely applied in numerical simulations, e.g., 0D [23-26] and 3D CFD (RANS [36], and LES [37-39]). This model assesses the flame wrinkling in the unresolved volume by solving the filtered transport equation. Particularly, when using the approach by Charlette et al. [37], the model is capable of reflecting the transitional phase between laminar and turbulence states since it can adjust the efficiencies of the respective turbulent length scales on flame wrinkling. This proposition is of vital importance for modeling the transitional phase since the inner cutoff, the smallest ineffective turbulence scale for flame wrinkling, could vary significantly depending on combustion environments, e.g., reactant compositions and thermodynamic conditions.

Accordingly, the FSD model has been successfully simulated for a variety of fuels in 0D simulations. For instance, Bourgrine et al. [23] validated the model with the experimental data using various blends of gasoline/ethanol. Demesoukas et al. [24] further included differential diffusion effect in their simulation and validated the model using the experimental data of iso-octane, propane, and methane. Note that the description of the 0D FSD model utilized in these studies is elaborated in [26].

As this study aims to develop a universally applicable simulation for the extensive ranges of thermodynamic and chemical states, the capability for reflecting the intrinsic characteristics of various fuels should be essentially accommodated in the model. In that respect, the proposed simulation is built upon the 0D FSD model, and several sub-models are complemented based on the analyses herein. Lastly, it is worth noting that the fractal nature of turbulent flame is also identified in the expression for the fully-developed turbulent flame speed used in this study.

## **1.2. Reviews of in-cylinder phenomena**

### **1.2.1. Behaviors of tumble**

There have been lots of efforts to increase the turbulence in SI engines during combustion, and the flow structure called tumble has been predominantly applied to intensify turbulence to date. In addition to increasing the flame propagation speed, tumble affects transport phenomena such as heat transfer and air/fuel mixing and plays a crucial role in cycle-to-cycle variations of combustion.

Further, recent studies have revealed the effects of tumble on the characteristics of a spark channel such as restrike and stretching. It was observed that the stretching, the elongation of the spark channel by the convection of flow, increases the energy supply efficiency of the spark channel [40]. This finding was also identified by Jung et al. [41] in the cases with different tumble strengths, demonstrating elevated spark discharge energy by intensifying tumble strength. That is, as the misfire caused by low spark discharge energy at the lean-limited condition is a major challenge in a homogeneous lean-burn SI engine, one of the most promising high-efficient combustion technology [42], tumble eventually increases the thermal efficiency of the engine not only by shortening burn duration but by expanding the lean operation range of the engine.

In the recent automotive industry, various technologies such as turbocharging, variable valve actuation (VVA), and gasoline direct injection (GDI), have been developed for modern SI engines. Since tumble affects numerous in-cylinder phenomena, its variances induced by the abovementioned technologies could greatly influence the performance of the engine. In that respect, diverse studies have been

conducted to identify the changes of tumble with various engine parameters. As for the valve strategies, Bucker et al. [43] analyzed the effect of intake valve timing on tumble, whereas Wang et al. [44] investigated the effect of intake valve lift. Meanwhile, Alger et al. [45] revealed the effects of tumble and swirl on air/fuel mixing in a GDI engine with different injection timings. Considering the formation of tumble is also affected by discrete engine geometries, several works have been performed to control the strength of tumble with various piston shapes [46] and engine port designs [47].

Moreover, there have been consistent efforts to comprehend the physical behaviors of tumble. Some studies have focused on the movement of the tumble center and revealed that the tumble center moves toward the exhaust valve during the early phase of compression [15, 48, 49]. Afterward, the center returns to the geometric center of the cylinder during the latter phase of compression, as observed experimentally by Buschbeck et al. [49] and numerically by Kim and Song [15]. Furthermore, Zentgraf et al. [48] revealed that turbulence is concentrated on the peripheral to the tumble center during compression, which can be utilized as conducive evidence to configure the distribution of turbulence during combustion.

As reviewed by Arcoumanis et al. [47], previous studies revealed two in-cylinder phenomena associated with the kinetic energy of tumble during the compression stroke: “spinning up” and “vortex breakdown.” Specifically, spinning up refers to the increase in the kinetic energy of tumble by the piston during compression, whereas vortex breakdown refers to the rapid production of turbulence by breaking the tumbling vortex near the firing top dead center (TDC). During compression, the intensified tumble by spinning up decays and produces stronger turbulence through vortex breakdown near the firing TDC, contributing to an increase in flame propagation speed. These characteristics have been primarily



interpreted based on the angular momentum perspective thus far [47, 50]. As discussed earlier, however, this theory has limitations for interpreting tumble behaviors. Therefore, this study attempts to understand these phenomena with the kinetic energy analysis of tumble and establishes the model based on the analysis.

### **1.2.2. Premixed laminar flame**

Laminar flame speed, the flame speed unperturbed by any flow motion, is of paramount importance in that it characterizes the fundamental flame speed under specified chemical and thermodynamic conditions. In SI engines, it appreciably influences the early combustion phase, during which the flamelet is marginally wrinkled. In addition to the early combustion, it involves the determination of turbulent flame speed, given that the flamelet locally exhibits laminar-like behavior [51] typically in flamelets regimes. Accordingly, a thorough investigation of laminar flame speed is an undeniably crucial procedure for revealing the characteristics of premixed flame.

Above all, the effect of the flamelet curvature on the laminar flame speed [52], denominated as “preferential diffusion” or “differential diffusion,” has intrigued numerous researchers until recently. That is, laminar flame speed varies linearly with the flamelet curvature at the weak stretch rate but non-linearly at the intense stretch rate [53, 54]. This correlation is indeed crucial in the development of combustion models with different fuels since the slope representing the sensitivity of the laminar flame speed against the curvature, called the Markstein length, is an intrinsic property of reactant species. As the flame spherically propagates from the ignition spot in an SI engine, it inevitably experiences an intensely curved surface at the very beginning. Therefore, the flame does not retain its planar laminar flame speed and occasionally results in total quenching of the flame due to the decrease in speed [55],

particularly for the mixture with a high Markstein length. This phenomenon is worth discussing as it seems to increase the cycle-to-cycle variance in a lean-burn SI engine, which is the major challenge for the extremely lean gasoline/air mixture.

In the presence of differential diffusion, the sustainability of flame could be of far more significance in outwardly propagating spherical flame, the intrinsic structure of SI engines. In this regard, several recent studies have inspected the flammability limit of the reactants with Lewis numbers greater than unity (i.e., corresponding to higher Markstein lengths).

Chen and Ju [56] theoretically revealed the importance of radiation heat loss and Lewis number on the flammability limit. Using their analytical solutions of flame radius, they found the radiation loss significantly increases the critical radius, the smallest radius for a sustainable flame. Based on the theory [56] and numerical analysis, Chen et al. [57] subsequently demonstrated the strong dependency of Lewis number and critical radius. More specifically, they numerically showed the increase of critical radius with increasing Lewis number by varying the equivalence ratio of hydrogen/oxygen and the composition of the inert gases. Additionally, they found that the minimum ignition energy required for a sustainable flame is proportional to the cube of the critical flame radius, provided the Zel'dovich number is being fixed.

Kelly et al. [55] experimentally investigated the effect of pressure on critical radius. As the laminar flame thickness decreases with increasing pressure, the critical radius was found to decrease to a certain extent due to the decrease in stretch effect. However, at sufficiently high-pressure conditions, the critical radius was shown to increase with increasing pressure due to the increase in activation energy. On the other hand, Eisazadeh-Far et al. [58] quantitatively showed the individual contributions of various factors (e.g., spark energy, chemical energy, and radiation

loss) on the temporal development of early flame propagation speed by analyzing the energy balance equation.

It is worth noting that the model for discerning the flammability of reactants is of great utility when establishing the complete simulation as a virtual engine. The simulation in this study, unfortunately, does not include the flammability model and is exclusively dedicated to the prediction of the flame propagation speed assuming a sustainable flame. Therefore, the flammability model is expected to be embedded in the near future for completeness.

### **1.2.3. Premixed turbulent flame**

A turbulent flame, accounting for a majority of the engine combustion, is affected by a variety of factors such as the thermodynamic states of burned and unburned gases and the chemical states of reactants. Therefore, the nature of turbulent flame has not been explicitly elucidated due to its complexity; researches associated with bending effect, cutoff scales, flame instabilities, and so forth are still in progress. Here, the author will address several characteristics of turbulent flame and the previous analyses thereof.

As discussed elsewhere [29, 51, 59-69], turbulent flame speed has been observed not to increase linearly with the increase in turbulent intensity. More precisely, the increase in the speed typically decreases at sufficiently high turbulent intensity, portraying a bending profile. This phenomenon, called the “bending effect,” has been investigated extensively to elucidate the causes. Various factors such as differential diffusion [51, 62], local quenching [51], and inner cutoff (based on the laminar flame thickness [60, 63] and hydrodynamic instability [61, 70]) have been addressed for causes, although this has not been revealed explicitly.

Inner cutoff scale, the smallest turbulence length scale effective for flame wrinkling, has been diversely studied due to its relevance to the extent of wrinkled flame surface and thus turbulent flame speed. In that respect, it has been utilized for assessing the wrinkled flame surface in the fractal model. Particularly, this scale has been revealed to be proportional to the laminar flame thickness [60, 63], the Kolmogorov length scale [32, 33, 70, 71], or the characteristic scale of flame instability [61, 70], and accordingly, no consensus exists with respect to this scale as of today.

Meanwhile, there has been plenty of researches concerning flame instabilities, the self-wrinkling phenomena of the flamelet without the aid of turbulent flow. It is worth noting that two instabilities of flame, thermo-diffusive instability and hydrodynamic instability, have been primarily studied thus far. As for the thermo-diffusive instability, the production of flame surfaces is principally driven by the differential diffusion at curved flamelets. More specifically, the reactants with Lewis number less than unity exhibit more production of flame wrinkled flame surface than the reactants without the instability, and vice versa. Conversely, hydrodynamic instability, also known as Darrieus-Landau instability [72, 73], in principle arises from the gas expansion due to the density change across the flame. The detailed principle is explicated in the review by Law and Sung [74]. Note that, although the existence of those instabilities has been manifested in several studies [62, 75], the extent of their effects in turbulent conditions is still controversial [76].

In flamelets regimes, the corrugated flamelet exhibits laminar-like behavior. However, several distinctive flame characteristics in thin and distributed reaction zones, wherein the laminar flame thickness is lengthier than the Kolmogorov length scale, have been observed and debated in the literature. As small-scale turbulences can penetrate the flame thicknesses, the changes in reaction and preheat zone

thicknesses in these regimes have been studied numerously to date [77-81]. Some studies [82-84] found a decrease in the differential diffusion effect due to the enhancement of both thermal and mass diffusivities at high Karlovitz number conditions. Note that the lean combustions should be of special concern regarding those characteristics since they exhibit lower planar laminar flame speed than general stoichiometric combustions, leading to higher Karlovitz numbers.

### **1.3. Research objective and implication**

The first objective of this study is to propose a physics-based 0D turbulence model applicable to various valve strategies and engine designs without changing any model constant. This can be achieved by developing the models based on the kinetic energy analysis of tumble. The proposed simulation was thus able to reproduce the results of all the possible valve strategies with VVA modules and five engine geometries without changing model constants. Furthermore, the proposed 0D turbulence model has a significant implication in that it is the first model based on the kinetic energy of tumble, differing from the existing models based on the angular momentum of tumble.

The combustion phenomena occurring in SI engines are exceptionally complicated due to the time-variant environments with extremely broad ranges of thermodynamic and hydrodynamic states. Besides, the recent developments of engine technologies, such as highly-diluted exhaust gas recirculation, lean-burn, and uses of various fuels, further elevated the diversity of combustion environments. Under those circumstances, a variety of combustion phenomena in Sections 1.2.2 and 1.2.3, varying with combustion environments, could critically affect engine performances. The point is that the impacts of those phenomena on engine

combustion have not been well clarified to date and occasionally have been neglected in combustion models. As a consequence, the models without reflecting those phenomena might fail to predict the combustions resulting from the latest engine technologies.

Therefore, the second objective of this study is to establish a comprehensive model reflecting all the combustion phenomena, thereby securing the model's universality with respect to various combustion environments. This work has a significant implication considering it provides the first 0D modeling framework including a vast majority of the combustion phenomena evidenced by numerous fundamental studies. Furthermore, this model will help to quantitatively analyze the individual effects of combustion phenomena, thus revealing the critical factors on engine combustions.

Finally, the third objective of this study is to develop a virtual engine that can be utilized for the engine optimization process. In practice, lots of attempts have been made to develop a virtual engine by using a 0D simulation due to its low computational cost. Unfortunately, the major problem has lied in the inaccuracy of the simulation. However, by enhancing the simulation's fidelity, a 0D simulation could be the most powerful tool for optimizing engine designs and operating strategies. In that sense, the author believes that the proposed simulation could be of great utility for practical application in the future engine industry.

## **1.4. Organization of the dissertation**

This dissertation mainly comprises the developments of 0D turbulence and combustion models of an SI engine. Since the turbulence model is based on the novel interpretation of tumble behaviors that differed from the previous studies, a separate

chapter is presented to explicate the new theory of tumble. Conversely, the analyses and theories required for the combustion model are elaborated in each modeling section.

Chapter 2 presents the newly developed theory of tumble. In this chapter, tumble is analyzed from the perspective of kinetic energy using 3D CFD simulations. According to the theory, the causes for tumble behaviors, such as reverse tumble, the movement of tumble center, vortex breakdown, and spinning up, are addressed.

In Chapter 3, a turbulence model is developed based on the proposed theory and presented in three categories: intake, turbulence production, spinning up models. As for the intake model, reverse tumble and intake loss were considered with the additional analysis of effective flow area. In addition, the turbulence production model is built upon the virtual 3D velocity vector field, called the “modified barrel swirl,” capable of reflecting vortex breakdown. Lastly, the spinning up model is built upon the analysis of the piston effect on tumble energy.

In Chapter 4, a combustion model is developed based on the existing FSD model. The characteristics of laminar and turbulent flames described in Sections 1.2.2 and 1.2.3 are considered in this model. Herein, the 0D simulation with the proposed turbulence and combustion models is validated with numerous experimental data obtained from an extensive range of thermodynamic and hydrodynamic states.

Finally, Chapter 5 analyzes the combustion phenomena using the complete 0D simulation. The distinctive features of stoichiometric and lean combustions are revealed in this chapter.

## **Chapter 2. FUNDAMENTAL STUDY OF TUMBLE BEHAVIORS**

### **2.1. Methodology**

#### **2.1.1. Base setup for 3D simulation**

The commercial CONVERGE CFD code [85] was used for 3D CFD simulation. Unsteady Reynolds-averaged Navier-Stokes (URANS) equations applying the RNG  $k$ - $\epsilon$  model [86] were used for interpreting turbulence. The temperatures of the initial in-cylinder gas, intake gas, and exhaust gas with the composition of air were set to 300 K. Additionally, all wall boundary temperatures were kept constant at 300 K. The pressure of the initial in-cylinder gas was set to 1 atm, while the intake pressure was 0.7 bar. The simulation starts at the exhaust valve opening (EVO) and ends at the firing TDC.

The base grid size was chosen to be 3.2 mm, and the local grid size was adjusted to be refined until it became 0.4 mm according to the simulation state by fixed embedding and adaptive mesh refinement (AMR) techniques. In the general in-cylinder area, harsher fixed embedding was applied in the regions adjacent to the valves and the liner wall. AMR was active on the gradient of the velocity component with a subgrid criterion of 1 m/s and a maximum embedding level of three. Figure 2.1 shows one instance of the refined mesh area obtained by utilizing those techniques.



The Gamma 2 engine developed by Hyundai Motor Company was employed in the simulation. The detailed operating conditions are presented in Table 2.1. The engine geometry and the coordinates used in the later analysis are presented in Fig. 2.2. The intake ports of the engine are displayed on the right side of the figure. As the engine does not utilize any flow motion other than tumble, the engine is symmetrical about the x-y plane crossing the center of the bore.

The cross-sectional planes used to demonstrate the velocity vector fields in the later analysis are parallel to the x-y plane, where the tumble structure can be clearly observed. Two planes are employed in the analysis: a central plane and a valve plane. The central plane refers to the plane containing the center of the bore, and the valve plane refers to the plane containing the center of the intake valve.

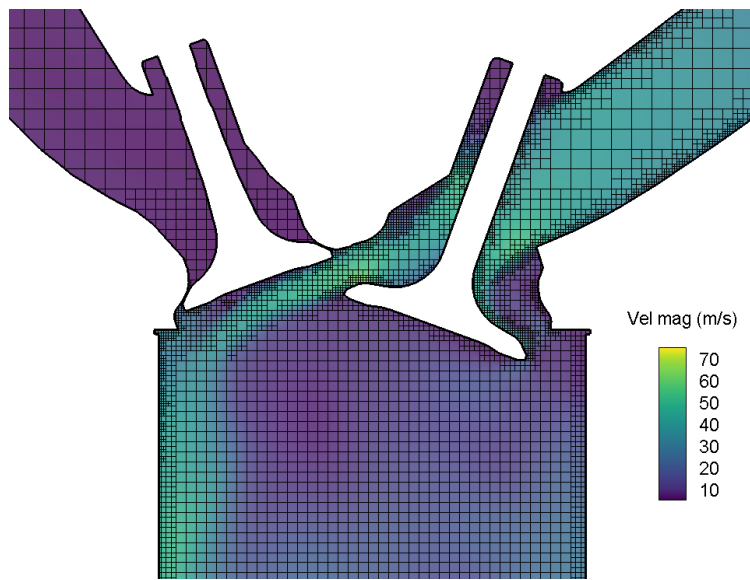


**Figure 2.1** Refined mesh during the intake stroke, with the contours of velocity magnitude.

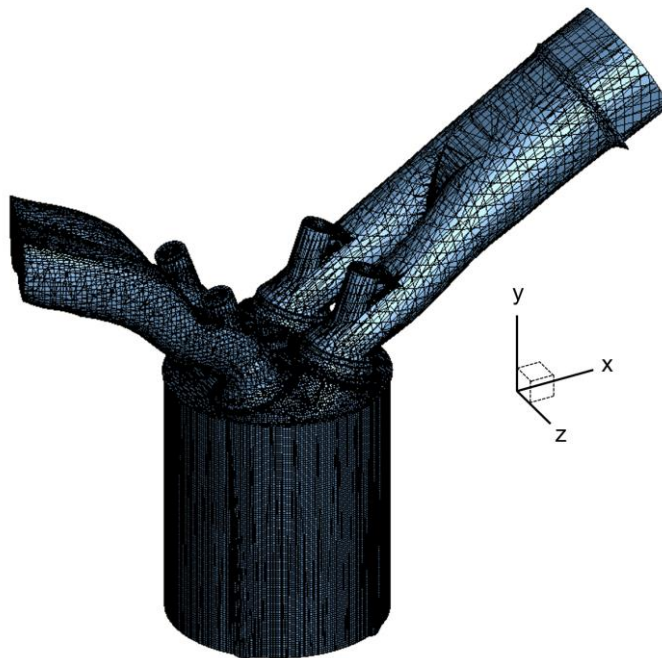


**Figure 2.2** Engine geometry and coordinates.

**Table 2.1** Reference engine operating conditions.

Operating condition	Value
Engine speed	1600 [rev/min]
Intake manifold pressure	0.7 [bar]
Compression ratio	10.5 [-]
Bore	75.6 [mm]
Stroke	89 [mm]
Connecting rod	145 [mm]
Intake valve diameter	30.5 [mm]
Exhaust valve diameter	25 [mm]
Exhaust valve opening (EVO)	160 [aTDC]
Exhaust valve closing (EVC)	391 [aTDC]
Intake valve opening (IVO)	343 [aTDC]
Intake valve closing (IVC)	600 [aTDC]

### 2.1.2. Definition of tumble energy

Angular momentum  $\mathbf{M}$  and tumble ratio TR have been commonly utilized to represent the strength of tumble in the automotive industry [44, 87]. The moment of inertia  $I$  and the above terms have the mathematical forms of Eqs. (2.1)-(2.3):

$$I = \sum_i \rho_i V_i |\hat{\mathbf{r}}_i \times \hat{\mathbf{k}}|^2, \quad (2.1)$$

$$\mathbf{M} = \sum_i \rho_i V_i (\hat{\mathbf{r}}_i \times \hat{\mathbf{v}}_i), \quad (2.2)$$

$$\text{TR} \equiv \frac{\mathbf{M}}{I\mathbf{w}_c} = \frac{\sum_i \rho_i V_i (\hat{\mathbf{r}}_i \times \hat{\mathbf{v}}_i)}{\mathbf{w}_c \sum_i \rho_i V_i |\hat{\mathbf{r}}_i \times \hat{\mathbf{k}}|^2}, \quad (2.3)$$

where  $\rho_i$ ,  $V_i$ ,  $\mathbf{w}_c$ , and  $\hat{\mathbf{k}}$  are the density, volume, engine angular velocity, and z-direction unit vector, respectively. The components with subscript  $i$  denote the property of the  $i$ -th cell. Additionally,  $\hat{\mathbf{v}}_i$  is a velocity vector, and  $\hat{\mathbf{r}}_i$  is the distance vector between the cylinder's volume center and the centroid of the  $i$ -th cell.

Nonetheless, the “tumble energy” is used in this study to indicate the intensity of tumble, instead of the angular momentum and tumble ratio. Tumble energy  $K_{\text{rot}}$  is determined as follows:

$$K_{\text{rot}} \equiv \frac{|\mathbf{M}|^2}{2I} = \frac{|\sum_i \rho_i V_i (\hat{\mathbf{r}}_i \times \hat{\mathbf{v}}_i) \cdot \hat{\mathbf{k}}|^2}{2 \sum_i \rho_i V_i |\hat{\mathbf{r}}_i \times \hat{\mathbf{k}}|^2}. \quad (2.4)$$

The primary reason for using tumble energy is that it minimizes the distance information such as the instantaneous height and bore, which is irrelevant to the kinetic energy of tumble. As opposed to the angular momentum and tumble ratio (refer to Eqs. (2.2)-(2.3)), the numerator and the denominator of tumble energy in Eq. (2.4) have an identical order of  $\hat{\mathbf{r}}$  that contains distance information. In that respect, the tumble energy  $K_{\text{rot}}$  is selected as the representative tumble metric. Accordingly, the mass-specific tumble energy  $k_{\text{rot}}$ , which is the quantity of tumble energy divided by the in-cylinder mass, is employed throughout the study.

## **2.2. The analysis of the intake of tumble energy**

### **2.2.1. Reverse tumble**

Kim et al. [14] showed that the mass flux across the valve curtain area tends to be evenly distributed at a low valve lift by using steady CFD results. Since the uniformly distributed mass flux gives an adequately strong momentum for forming the flow structure to the flows passing both the upper and lower sides of the valve curtain area, it generates two vortices: tumble and reverse tumble. These vortices were also identified experimentally in previous studies [44, 50] by using particle image velocimetry (PIV). These studies revealed the presence of the two vortices rotating in opposite directions during the early intake stroke under lower valve lift conditions [44] and the engine configuration with a low tumble ratio [50].

To demonstrate the effect of reverse tumble on the formation of tumble, three different intake valve profiles were employed, as shown in Fig. 2.3. Based on the reference valve profile, two profiles were created by constraining the maximum valve lift to two and three millimeters. As seen in Fig. 2.4, unlike the reference profile, those profiles generate unorganized flow structures containing two vortices during the entire intake process. The reverse tumble disturbs the formation of the tumble structure, and eventually, a small amount of tumble energy is generated in the lower valve lift cases. Even though the reference valve lift case in Fig. 2.3 is applied, the reverse tumble is also observed in the early intake period where the instantaneous valve lift is sufficiently low. Hence, tumble energy does not increase in that period. This finding is also demonstrated by the tumble energy results in Fig. 2.3. As three millimeters appears to be an adequately low valve lift for forming tumble in the given

engine geometry, the tumble energy in the reference case starts to increase when the instantaneous valve lift is higher than three millimeters.

In addition, the kinetic energy is calculated under the subjected volume excluding the pent-roof volume, as in Fig. 2.3. The selected volume is not intended to cover the momentary high-velocity components near the valve regions. The kinetic energies in the figure are high at approximately 450 crank angle degree (CAD) in all three cases, implying that an adequately strong momentum exists for forming tumble flow, even with the lower valve lifts. However, unorganized flow structures in the constrained cases lead to a high decay rate, and they abruptly lose their kinetic energies during the intake stroke.

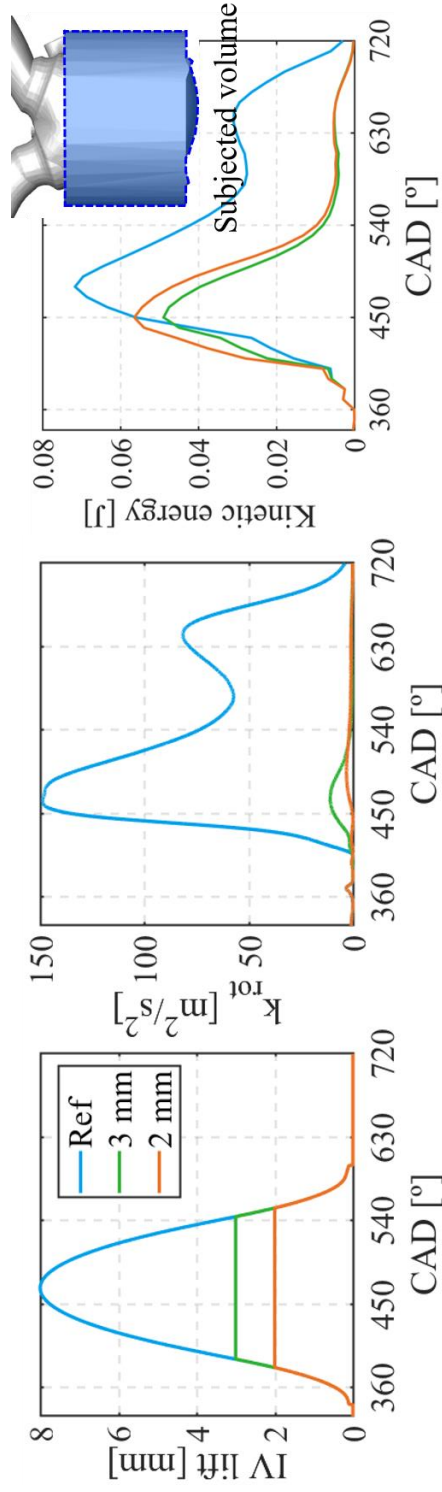


**Figure 2.3** Intake valve lift profiles, tumble energy, and kinetic energy results of the reference case and low-maximum-valve-lift cases (2 mm and 3 mm).

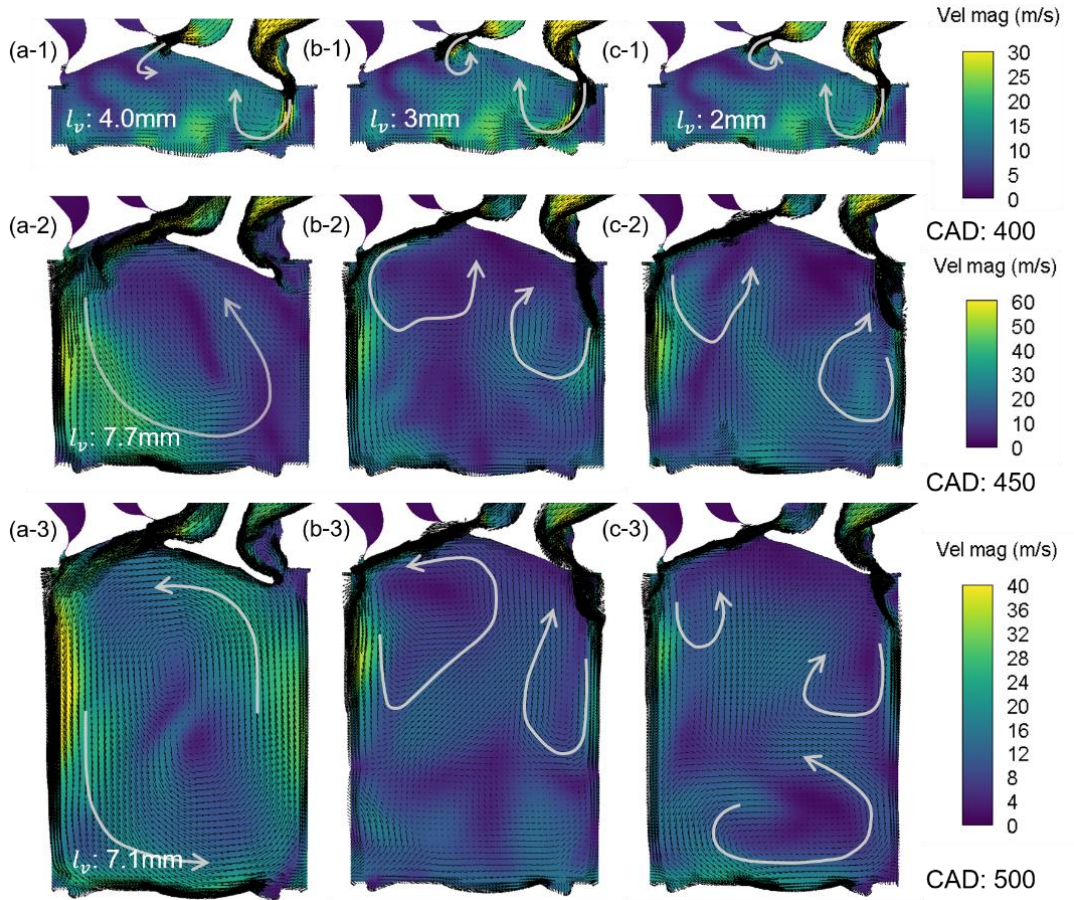


**Figure 2.4** Velocity vector fields at 400 CAD, 450 CAD, and 500 CAD along the valve plane: (a) reference valve profile, (b) valve profile with a maximum valve lift of 3 mm, and (c) valve profile with a maximum valve lift of 2 mm.  
( $l_v$  is instantaneous valve lift)



## 2.3. The analysis of the velocity field during the compression stroke

In proposing a new way of understanding the tumble behavior during the compression stroke, a uniformly distributed density over the cylinder is assumed since the in-cylinder temperature and pressure during compression are also fairly uniformly distributed. Then, the in-cylinder velocity is divided into two components, as shown in Eq. (2.5):

$$\hat{\mathbf{v}} = \hat{\mathbf{v}}_t + \hat{\mathbf{v}}_p, \quad (2.5)$$

where  $\hat{\mathbf{v}}_t$  and  $\hat{\mathbf{v}}_p$  are the tumble velocity and piston-induced velocity, respectively, and  $\hat{\mathbf{v}}$  is the resultant velocity. Tumble velocity corresponds to the flow structure with a rotational motion that satisfies the mass conservation in a stationary condition, and piston-induced velocity satisfies the mass conservation during the piston moving condition. Therefore, the resultant velocity representing the actual in-cylinder velocity also satisfies mass conservation.

Superposition helps to elucidate the changes in the velocity vector field during the compression stroke, which is not straightforward to predict otherwise. To check the validity of the superposition, the proposed velocity fields are examined in the following sections.

### 2.3.1. The period between BDC and IVC

It should be first noted that the timings of the IVC that occur after the bottom dead center (BDC) are exclusively considered throughout the study. While the intake valve is opened during the compression stroke between the BDC and IVC, the piston motion adds constant positive y-direction velocity to the overall vector field, only discharging the mass located on the upper side of the cylinder. That is, there is very little, if any, increment in tumble energy defined in Eq. (2.4) since the identical additional velocities at the x-z plane cancel each other when calculating the tumble energy. The piston-induced velocity before IVC is simplified as follows:

$$\hat{\mathbf{v}}_p = v_p \hat{\mathbf{j}}, \quad (2.6)$$

where  $v_p$  is the instantaneous piston speed and  $\hat{\mathbf{j}}$  is the y-direction unit vector.

For the validity of Eq. (2.6), a simulation of compression stroke with a fixed intake valve opening at one millimeter was conducted to verify the effect of the piston-induced velocity during an open valve period. The simulation was started at BDC (540 CAD) with no internal flow motion. Figure 2.5 presents the results of the velocity vector fields corresponding to 570, 600, and 630 CAD. As seen from the figure, the piston-induced velocity is fairly uniformly distributed in the vector fields, as proposed in Eq (2.6), excluding the upper side area of the cylinder near the intake valve where the mass is transferred out to the intake manifold.

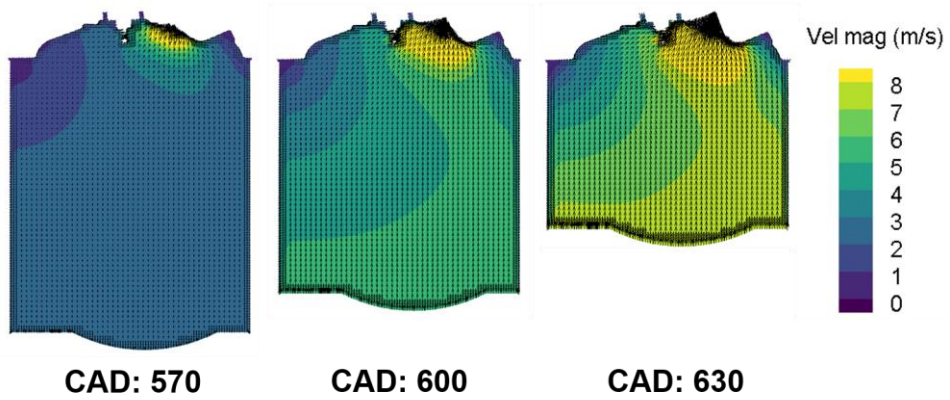


**Figure 2.5** Velocity vector fields across the central plane for the 1 mm intake valve open condition.

### 2.3.2. The period between IVC and firing TDC

When the valve is closed during the compression stroke, to satisfy the mass conservation in the trapped cylinder gas, the piston-induced velocity should have a linear profile across the  $y$ -direction, decreasing from the piston speed at the bottom to zero at the top. Therefore, the piston-induced velocity after IVC is simply expressed as described in Eq. (2.7):

$$\hat{\mathbf{v}}_p = v_p \left( \frac{1}{2} - \frac{(y - y_c)}{H} \right) \hat{\mathbf{j}}, \quad (2.7)$$

where  $y_c$  is the  $y$ -coordinate of the cylinder volume center and  $H$  is an instantaneous cylinder height.

To investigate the validity of Eq. (2.7), a simulation of the compression stroke with a closed intake valve was performed. Similar to the intake valve opening simulation in Section 2.3.1, the simulation was also started at BDC (540 CAD) with

no internal flow motion. The results of the velocity vector fields in Fig. 2.6 show that the velocity monotonically decreases along the positive y-direction, as proposed in the corresponding equation.

Since the flow occurs in a closed system, the profile of the tumble velocity  $\hat{v}_t$  in Eq. (2.5) also needs to satisfy mass conservation. Assuming a quasi-steady flow during compression, as the instantaneous cylinder height  $H$  becomes shortened, the effective flow area for the x-direction velocities decreases, while the area for the y-direction proportional to the cylinder bore remains unchanged. More precisely, the passage for the x-direction velocities proportional to  $H$  becomes thinner due to the compression. Then, provided that the kinetic energy is conserved along the streamline of the tumble velocity, the ratio between the magnitude of the x-direction velocity to that of the y-direction velocity increases. Therefore, more kinetic energy is distributed to the x-direction velocity rather than the y-direction velocity during compression; Figure 2.7 shows an example of the velocity magnitude distribution at different crank angle positions, thereby demonstrating the aforesaid distributions. Throughout the study, this phenomenon will be referred to as “distortion” of tumble velocity.

To reveal the degree of the distortion quantitatively, the kinetic energy ratio is introduced in Fig. 2.8. The ratio is determined by dividing the in-cylinder kinetic energy associated with the y-direction velocity by that of the x-direction velocity. This ratio clearly illustrates the distortion due to the change in the bore-to-height ratio.

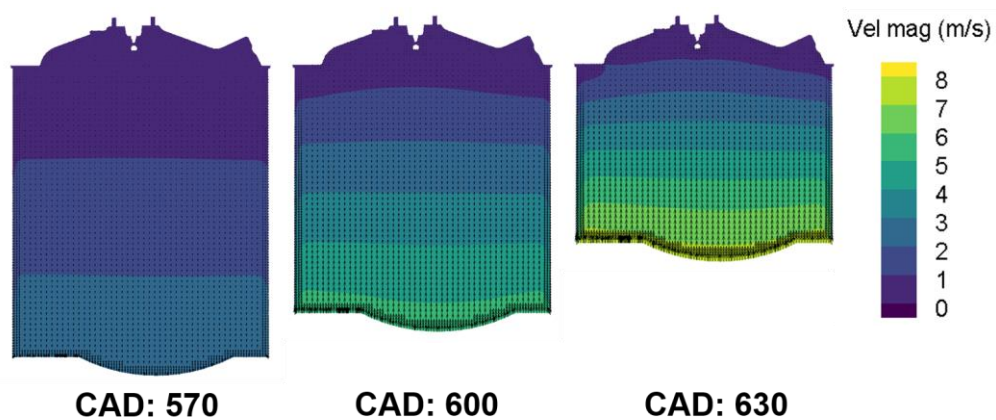


**Figure 2.6** Velocity vector fields in the central plane for the closed intake valve condition.

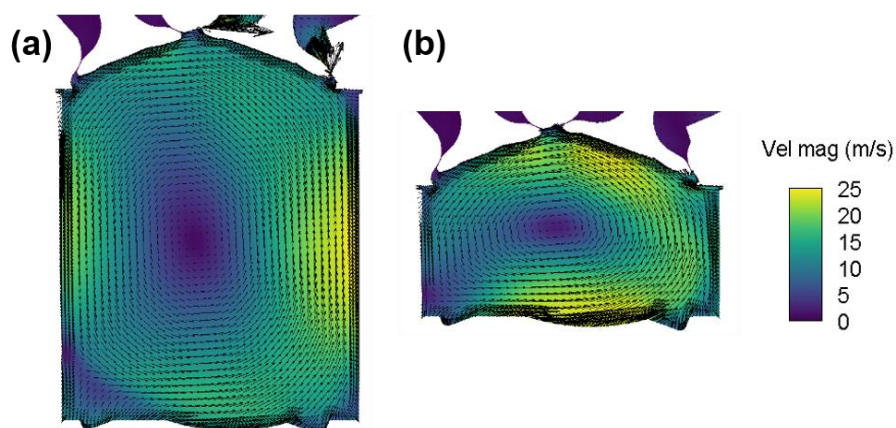


**Figure 2.7** Distortion of tumble velocity from the reference case: (a) 600 CAD and (b) 660 CAD.

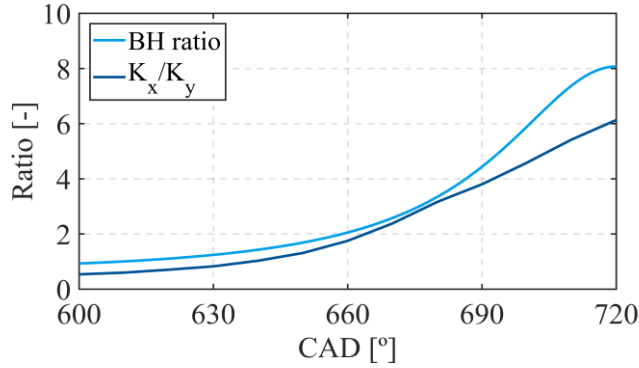


**Figure 2.8** Bore-to-height ratio and the kinetic energy ratio between the x-direction and y-direction for the reference case.

### 2.3.3. Movement of the tumble center

The tumble center, also known as the vortex center, is the major characteristic of the tumble structure. Zentgraf et al. [48] found that turbulence is concentrated at the tumble center during the compression stroke. Various studies have been performed to determine the location of the tumble center. Kang and Baek [88] evaluated the tumble eccentricity, indicating the degree of deviation in a vertical direction between the tumble center and the cylinder center. Li et al. [89] presented a tumble center motion analysis pointing out the influence of piston motion. Baby and Floch [90] tracked down the tumble center position for an engine with four different piston shapes.

The literature [48, 89, 90] suggested that the tumble center moves toward the exhaust side during the compression stroke. However, those studies did not reveal the motion after 50 CAD bTDC due to the experimental limitation of an optical engine. In addition, they did not explain the cause of this tumble center movement.

Here, the fundamental flow structure will be examined to pinpoint the reason for the movement of the tumble center.

In order to imitate the tumble structure during the compression stroke, simplified virtual velocity vector fields in a two-dimensional space (x-y space) are introduced in Figs. 2.9 and 2.10. These figures show the superposition of the in-cylinder velocity vector fields proposed at the beginning of the section (see Eq. (2.5)). Particularly, the tumble velocity function in the virtual velocity field was constructed by applying the “modified barrel swirl” proposed by Kim et al. [8], and the piston-induced velocity functions introduced in Eqs. (2.6) and (2.7) were applied. For illustrative purposes, the magnitude of the piston velocity is assumed to be half of the maximum magnitude of the tumble velocity. These figures show the instant velocity fields at 570 CAD in the x-y plane containing the center of the z-coordinate. Hence, the position of (0,0) refers to the volume center coordinates of the engine.

It was observed that the tumble centers, which are the zero-velocity points in the resultant velocity vector fields in Fig. 2.9(c) and Fig. 2.10(c), move toward the left side (exhaust side of the engine) since the piston-induced velocity causes asymmetry in the flow structure. This asymmetry arises because the piston-induced velocity strengthens the positive y-direction velocity vectors, whereas it weakens the negative y-direction velocity vectors in the resultant velocity vector fields. Based on Eqs. (2.6) and (2.7), as the piston-induced velocity before IVC has an overall larger velocity magnitude than the velocity after IVC with an identical piston speed, the tumble center before IVC moves further toward the left side than the tumble center after IVC.

Simulations were implemented to verify the above proposition regarding the movement of tumble center according to the different IVC timings. In order to form an identical tumble at the beginning of the compression stroke, the intake valve profile is kept the same until the intake valve lift becomes one millimeter at the end of the intake process. Figure 2.11 presents the tested valve profiles.

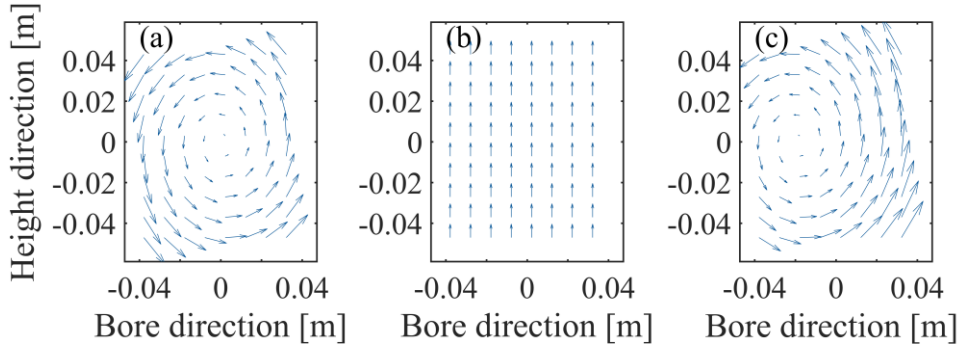


**Figure 2.9** Virtual velocity fields before IVC during the compression stroke: (a) tumble velocity, (b) piston-induced velocity, and (c) resultant velocity.

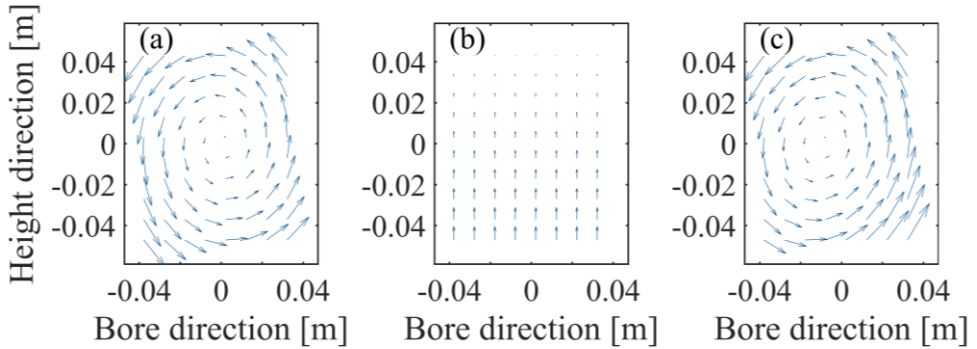


**Figure 2.10** Virtual velocity fields after IVC during the compression stroke: (a) tumble velocity, (b) piston-induced velocity, and (c) resultant velocity.



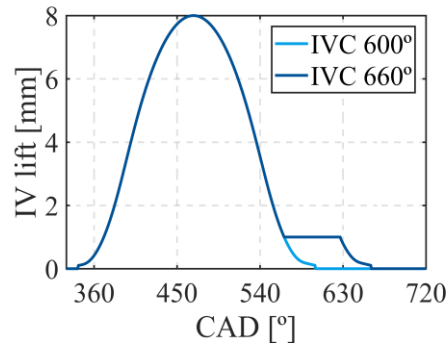


**Figure 2.11** Intake valve lift profiles with different IVC timings.

As the piston speed becomes zero at BDC, the velocity vector field at that time can be considered the tumble velocity. Although both simulations have the identical tumble velocity at BDC, the locations of the tumble center at the mid-stroke with two different IVC timings differ greatly, as shown in Fig. 2.12(b) and Fig. 2.12(c). The tumble center moves further toward the exhaust side with the late IVC timing condition than the earlier IVC timing condition, which is consistent with the previous virtual velocity vector fields (see Fig. 2.9(c) and Fig. 2.10(c)). Therefore, it can be concluded that the resultant velocity vector fields based on the superposition of Eq. (2.5) may reasonably describe the actual velocity vector fields. Additionally, the piston speed and IVC timing are revealed as the factors affecting the movement of the tumble center during compression.

Considering the aforesaid movement, the tumble center should return toward the intake side once the piston decelerates to a slower speed, such as in the latter part of the compression stroke. This phenomenon was also identified in the simulations. As seen in Fig. 2.13, therefore, the tumble centers of both IVC cases are ultimately located near the center of the cylinder.

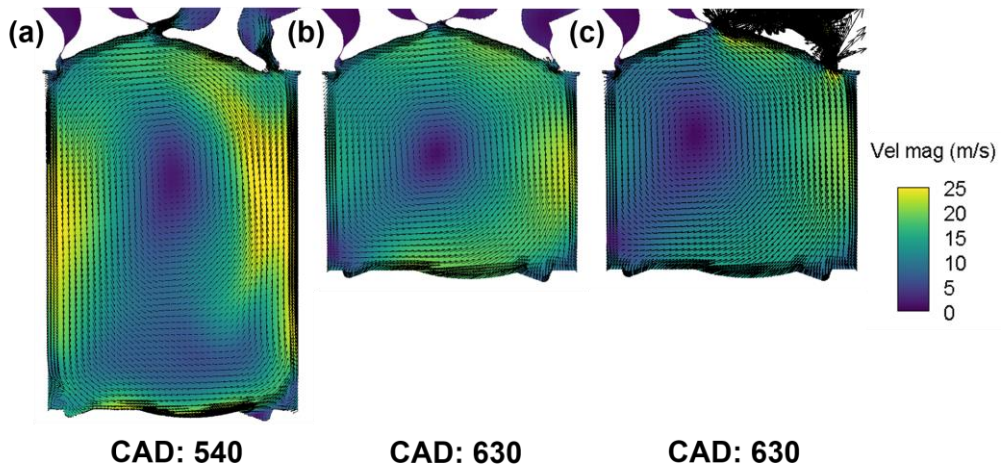


**Figure 2.12** Velocity vector fields across the valve plane: (a) tumble velocity at BDC, (b) resultant velocity at 630 CAD for the IVC 600° case, and (c) resultant velocity at 630 CAD for the IVC 660° case.

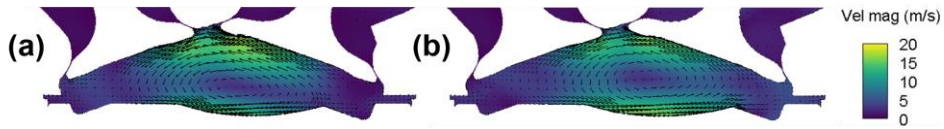


**Figure 2.13** Velocity vector fields at the TDC: (a) resultant velocity for the IVC 600° case, (c) resultant velocity for the IVC 660° case.

## 2.4. The analysis of tumble energy during the compression stroke

When the piston compresses the in-cylinder gas, the total (mean) kinetic energy increases or decreases depending on the in-cylinder velocity profile. The equation below presents the description in a mathematical form:

$$\dot{K}_{\text{ext}} = \sum_i \hat{\mathbf{f}}_{\text{ext},i} \cdot \hat{\mathbf{v}}_i = \sum_i \rho_i V_i (\hat{\mathbf{a}}_{\text{ext},i} \cdot \hat{\mathbf{v}}_i). \quad (2.8)$$

$\dot{K}_{\text{ext}}$ ,  $\hat{\mathbf{f}}_{\text{ext},i}$ ,  $\hat{\mathbf{v}}_i$ , and  $\hat{\mathbf{a}}_{\text{ext},i}$  are the kinetic energy increase rate, force, velocity, and acceleration, respectively. Subscripts ext and  $i$  each indicate externally induced properties exerted by the piston and the  $i$ -th component. Provided the inner product of a resultant velocity and an externally induced acceleration, i.e.,  $\hat{\mathbf{a}}_{\text{ext},i} \cdot \hat{\mathbf{v}}_i$ , is positive, the in-cylinder gas will increase its kinetic energy, and vice versa.

During the compression stroke, since the resultant velocity vector field includes the piston-induced velocity, which is always in the positive  $y$ -direction, it is worth stressing that the vectors in the positive  $y$ -direction are dominant over the vectors in the negative  $y$ -direction in the vector field. Therefore, when the piston accelerates with the positive  $y$ -direction, the total kinetic energy will increase according to Eq. (2.8). Conversely, it can be inferred that the kinetic energy will decrease with piston deceleration near the mid-stroke of the compression process.

However, it should be noted that the tumble energy does not always increase with increasing kinetic energy. Given that the rotating components are only considered in tumble velocity, piston-induced velocity does not affect the quantities of angular momentum and hence tumble energy. That is, the kinetic energy changes generated by the piston-induced velocity do not effectively accumulate as tumble energy and thus cannot explain the spinning up phenomenon during the compression stroke. In the following section, a new way of understanding spinning up will be provided based on the aforementioned flow structures.

### 2.4.1. Piston effect coupled with the viscous decay effect

Here, the statement of whether kinetic energy increases during the compression stroke is first investigated. Note that the accumulated energy in Fig. 2.14 was obtained by adding all the in-cylinder energy components that originated from the kinetic energy of the intake flow, i.e., mean kinetic energy (MKE), turbulent kinetic energy (TKE), and dissipated energy accumulated after EVO. Thus, considering that there is no kinetic energy intake change exerted on the in-cylinder charge after IVC (600 CAD), any change in the accumulated energy indicates the sheer variance in kinetic energy induced by the piston motion.

As expected, the kinetic energy generally increases when the piston accelerates with the positive y-direction, and it decreases otherwise. In the figure, however, although the piston deceleration starts from the mid-stroke of the compression process (approximately 645 CAD), the accumulated energy increases until approximately 690 CAD. To comprehend the phenomenon, it should be noted that

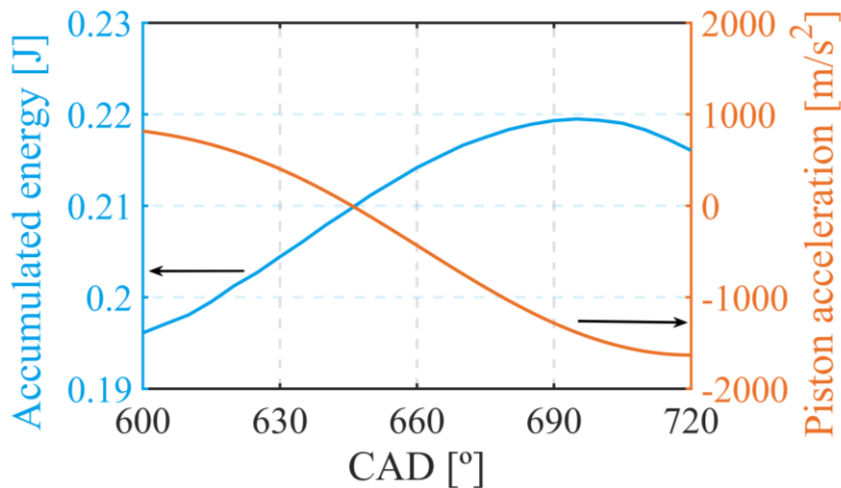


**Figure 2.14** Accumulated energy and piston acceleration in the reference case.

$\hat{\mathbf{a}}_{\text{ext},i}$  in Eq. (2.8) is not the only function of the magnitude of piston acceleration (or deceleration in the current discussion). Therefore, the kinetic energy does not always decrease during piston deceleration. For a close examination of this finding, the aforesaid superposition framework was applied.

First, the externally induced acceleration  $\hat{\mathbf{a}}_{\text{ext},i}$  in Eq. (2.8) needs to be analyzed based on the proper model and assumptions. As in the superposition analysis in Eq. (2.5), a uniformly distributed density over the cylinder is assumed. In Eq. (2.5), the resultant velocity is hypothetically divided into tumble velocity and piston-induced velocity to satisfy mass conservation in that instant. Similarly, as the acceleration determines the velocity vector field of the following instant, it needs to be formed to satisfy mass conservation in the resultant velocity of the following instant.

Since the resultant velocity is the superposition of the two velocity vector fields, the accelerations of those fields also need to be determined to satisfy the mass conservation of the following instant in each velocity field. The two fields shown on the left side in Fig. 2.15 are illustrated to visualize the velocities and accelerations satisfying the above condition in the hypothetical flow structure. For descriptive purposes, the figure presents the acceleration of piston-induced velocity at the moment when the piston decelerates.

In the figure, the acceleration profile of the tumble velocity presents the deceleration caused by the frictional force associated with the viscous decay of the turbulent fluid. In order to maintain the uniformly distributed density across the cylinder, the components of tumble velocity with identical streamlines should distribute their frictional forces along that streamline, as in the leftmost panel of Fig 2.15. Conversely, as the piston-induced velocity has the same velocity magnitude in

the plane perpendicular to the y-direction, the components on the plane have the same acceleration magnitude to maintain the uniform velocity profile of the following instant, as in Fig 2.15. As a result, by combining these two hypothetical acceleration profiles, the “actual” acceleration profile in the resultant velocity field can be evaluated.

However, in the resultant velocity field (on the right side of Fig. 2.15), due to the eccentric nature of the field during the compression stroke, the frictional force does not coincide with that of the ideal tumble velocity (on the left side of Fig. 2.15), causing the asymmetric acceleration distribution. Therefore, to match the overall acceleration profile to the sum of two hypothetical accelerations on the left side of Fig. 2.15, the force induced by the piston in the actual flow should look something like that in the rightmost profile in the figure. As the force direction is opposite to the resultant velocity direction, the decrease in the force leads to an increase in the velocity. Although the analysis was focused on the period of piston deceleration, the effect is also valid during piston acceleration. Consequently, to compensate for the deformation of the vector field caused by the piston velocity, the piston exerts a supplementary force proportional to the friction forces in the deformation area, eventually leading to the surplus in tumble energy and tumble spinning up.

From the understanding of the acceleration profile in the rightmost panel of Fig. 2.15, it can be hypothesized that the fast piston speed (determining the degree of the deformation) and the high frictional force around the deformation area will lead to a larger increase in tumble energy or a stronger spinning up. In the following discussions, further simulations are carried out to validate such hypotheses, which will indirectly demonstrate the validity of the superposition approach in explaining the spinning up of tumble.

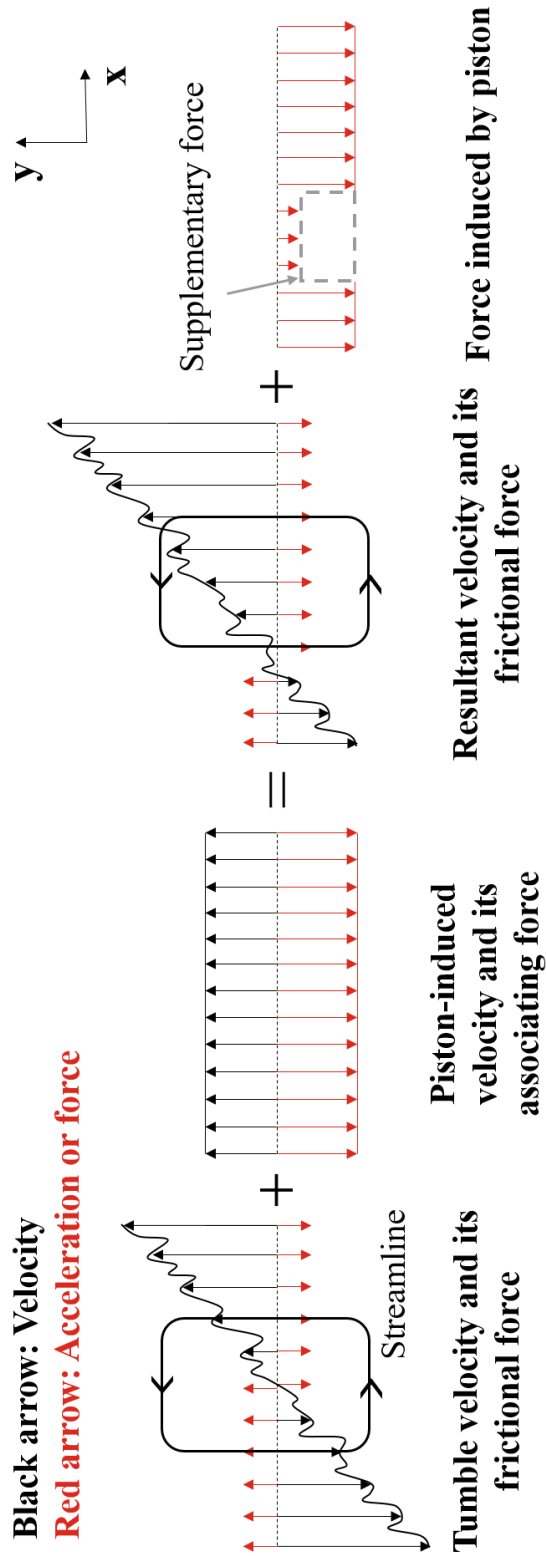


**Figure 2.15** Velocity and acceleration vectors along the line parallel to the x-direction.

Therefore, the additional simulation was conducted with the lowered modeling constant  $C_\mu$  in Eq. (2.9), while keeping the rest of the conditions the same as those of the reference case. The purpose of the simulation is to verify the frictional force effect on the accumulated energy by modulating the viscosity. The change in the modeling constant was executed after IVC (600 CAD). Since the viscous decay of kinetic energy is reduced with the lowered modeling constant, the quantity of kinetic energy in Fig. 2.16 is higher than that in the reference case. On the other hand, the accumulated energy decreases greatly during piston deceleration more than that of the reference case, implying the role of frictional force in the increase in the accumulated energy. Therefore, it can be concluded that the net kinetic energy variance during compression becomes positive with the aid of frictional force, thereby intensifying tumble. Moreover, the decrease in the accumulated energy in the case of low  $C_\mu$  is noteworthy in that this phenomenon cannot be understood by the existing angular momentum theory. The turbulent viscosity  $\nu_t$  is given by

$$\nu_t = C_\mu \rho \frac{k^2}{\varepsilon}, \quad (2.9)$$

where  $k$  and  $\varepsilon$  are TKE and dissipation of TKE, respectively.

Besides, it is worth noting that this phenomenon occurs after IVC. Before IVC, tumble velocity components do not need to formulate the streamline described in Fig. 2.15 since the in-cylinder mass is discharged by intake backflow. To verify this proposition, a simulation was executed employing the profiles with different IVC timings in Fig. 2.11. The simulation results of the mass-specific angular momentum, tumble energy, and TKE are presented in Fig. 2.17. In the figure, angular momentum



and tumble energy increase after IVC, which is especially evident for the IVC 600° case.

Since the x-direction velocity is intensified by the distortion of the tumble velocity as the piston approaches the TDC (refer to Fig. 2.7), the viscous shear stress increases. This causes the breakdown of tumble, which leads to a high turbulence intensity near the TDC. In that respect, in Fig. 2.17, the tumble energies in both cases decay rapidly near the TDC (720 CAD), thereby generating a second TKE peak. The resulting phenomenon, so-called “vortex breakdown,” has been observed in various studies [47].

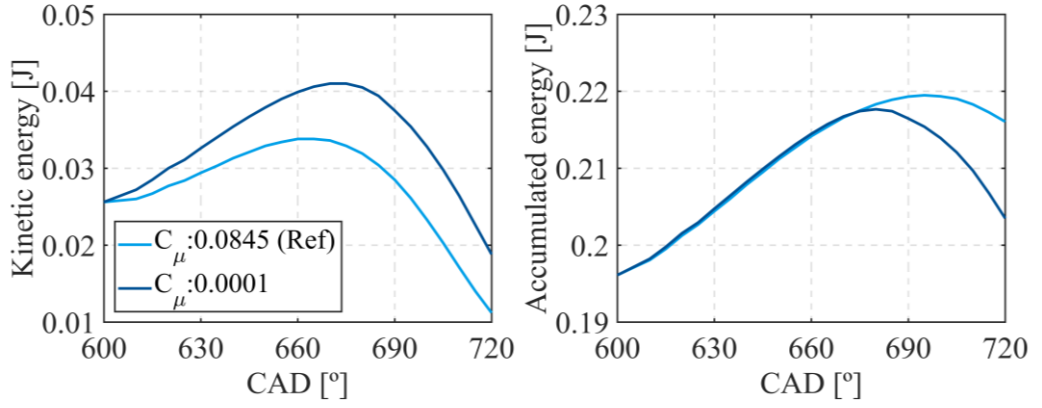


**Figure 2.16** Kinetic energy and accumulated energy  
with different values of  $C_\mu$ .

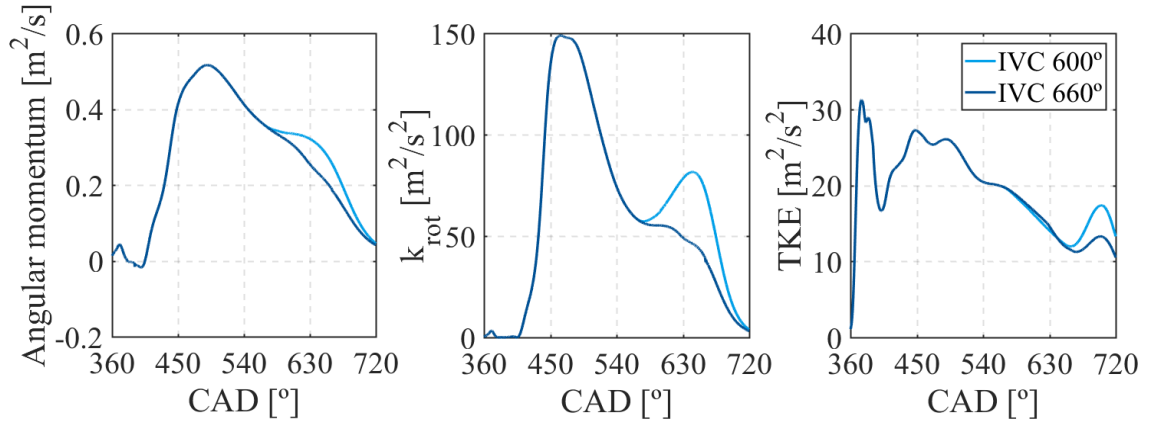


**Figure 2.17** Mass-specific angular momentum, tumble energy, and turbulent kinetic energy  
under different IVC conditions.

## **Chapter 3. TURBULENCE MODEL**

### **3.1. Methodology**

#### **3.1.1. Simulated cases**

The 3D CFD simulations were carried out using the commercial CONVERGE software with the identical configuration elaborated in Section 2.1.1. The objective of these simulations is (i) to verify the physics analyzed in this study and (ii) to compare the simulation results with the 0D results. Considering the study focuses on the flow behavior of tumble and the resultant turbulence, negligible effects of residual gas on turbulence are presumed for both 3D CFD and 0D simulations to reduce computational cost. This proposition is considered plausible in this numerical scheme as the closure of turbulent viscosity (if any) has little to do with temperature and in-cylinder composition. Therefore, instead of multiple cycles, a single motoring cycle covering the period between exhaust valve opening (EVO) timing and firing TDC is performed.

As summarized in Table 3.1, a total of 25 cases were simulated in the study. The hyphen (-) in the table indicates an identical condition to that of the reference case (Case 1). As every listed parameter affects tumble and resultant turbulence, all the cases serve as conducive instances for identifying the physical behaviors of tumble, eventually verifying the proposed model. By comparing cases 1–12, the effects of variable valve actuation were identified, such as valve timing, valve duration, and valve lift, on tumble. From cases 1 and 13–21, the effects of geometry were identified, such as connecting rod length, stroke, bore, and intake port design. Lastly, from cases 1 and 22–25, the effect of intake manifold pressure and engine speed were identified.

**Table 3.1** Simulated cases in this study.

Case no.	IVO [CAD]	IVC [CAD]	IV lift [mm]	Conrod [mm]	Bore [mm]	Stroke [mm]	CR [-]	$D_{in}/D_{ex}$ [mm]	Intake port type	Intake $P$ [bar]	Speed [RPM]
1 (Ref.)	343	600	8	145	75.6	89	10.5	30.5/25	A	0.7	1600
2	-	540	-	-	-	-	-	-	-	-	-
3	-	630	-	-	-	-	-	-	-	-	-
4	-	660	-	-	-	-	-	-	-	-	-
5	373	-	-	-	-	-	-	-	-	-	-
6	403	-	-	-	-	-	-	-	-	-	-
7	363	620	-	-	-	-	-	-	-	-	-
8	363	620	5	-	-	-	-	-	-	-	-
9	383	640	-	-	-	-	-	-	-	-	-
10	383	640	5	-	-	-	-	-	-	-	-
11	-	-	5	-	-	-	-	-	-	-	-
12	-	-	10	-	-	-	-	-	-	-	-
13	-	-	-	100	-	-	-	-	-	-	-
14	-	-	-	300	-	-	-	-	-	-	-
15	-	-	-	-	-	69	3.4	-	-	-	-
16	-	-	-	-	-	79	5.1	-	-	-	-
17	-	-	-	211.65	86	86	12	33/27	B	-	-
18	-	-	-	207.65	81	97	12	29/27	C	-	-
19	-	-	-	199.15	-	111	12	29/27	C	-	-
20	-	-	-	-	-	-	-	-	D	-	-
21	-	-	-	-	-	-	-	-	E	-	-
22	-	-	-	-	-	-	-	-	-	0.55	-
23	-	-	-	-	-	-	-	-	-	0.85	-
24	-	-	-	-	-	-	-	-	-	-	2400
25	-	-	-	-	-	-	-	-	-	-	3200

### 3.1.2. The overall schematic of turbulence model

It is first noted that the focus of this study is on engines solely utilizing tumble as the in-cylinder flow, excluding the others such as swirl and squish. Since the model is established based on the Reynolds-averaged Navier-stokes (RANS) equations, kinetic energy is divided into mean (MKE or  $K$ ) and turbulent (TKE or  $k$ ) kinetic energies. According to the energy cascade, TKE is produced due to energy transfer or turbulence production from MKE, and it eventually dissipates by the viscosity of fluids.

Figure 3.1 shows the overall schematic of the model along with the corresponding model equations from Eqs. (3.1)-(3.4). As tumble is perceived as kinetic energy instead of angular momentum throughout the modeling in this study, the tumble energy  $K_{\text{rot}}$  defined in Section 2.1.2 is utilized to represent the strength of tumble. Note that the definition is utilized for obtaining  $K_{\text{rot}}$  from 3D CFD. As for the 0D simulation,  $K_{\text{rot}}$  is calculated by using Eqs. (3.1)-(3.4). A detailed explanation of the terms in Eqs. (3.1)-(3.4) is in the following discussion.

$$\dot{K}_{\text{in}} = \dot{K}_{\text{rot,in}} + \dot{K}_{\text{nonrot}} \quad (3.1)$$

$$\dot{K}_{\text{rot}} = \dot{K}_{\text{rot,in}} + \dot{K}_{\text{spin}} - \dot{k}_{\text{rot}} - C_{\text{out}} \frac{\dot{m}_{\text{out}}}{m} K_{\text{rot}} \quad (3.2)$$

$$\dot{k} = C_{\text{rot}} \dot{k}_{\text{rot}} + \dot{k}_{\text{nonrot}} - \varepsilon - \frac{\dot{m}_{\text{out}}}{m} k \quad (3.3)$$

$$(\dot{k}_{\text{nonrot}} = C_{\text{non}} \dot{K}_{\text{nonrot}} + C_{\text{ex}} \dot{K}_{\text{ex}} + \dot{k}_{\text{den}})$$

$$\varepsilon = C_{\mu}^{3/4} m \frac{u'_{\text{avg}}{}^3}{l_t} \quad (3.4)$$

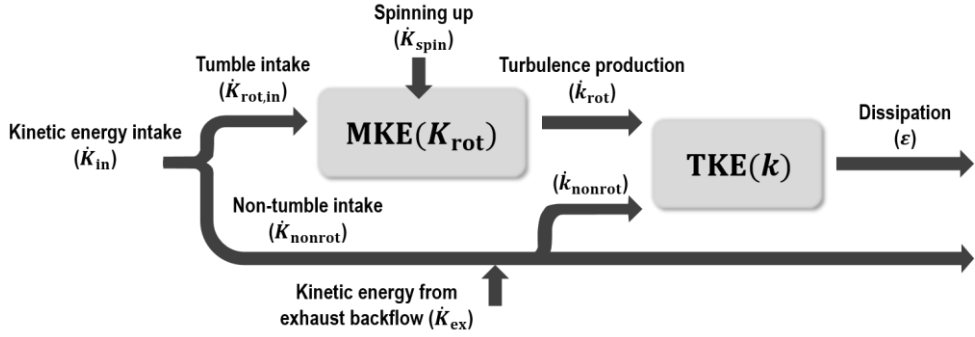


**Figure 3.1** Schematic of the kinetic energy flow in the 0D model.

Given the limitation of 0D simulations, an inaccuracy arises with the deficiency of reflecting the local flow phenomena. Nonetheless, the accuracy can be improved by reflecting the flow structures based on appropriate assumptions. Therefore, to reflect the distinctive features of the local flow structures in the model, the kinetic energy intake  $\dot{K}_{in}$  is divided into tumble intake  $\dot{K}_{rot,in}$  and non-tumble intake  $\dot{K}_{nonrot}$ , each contributing to the intake of tumble and non-tumble energies, as shown in Eq. (3.1). This approach is based on the concept that the flows excluding tumble do not possess sufficient inertial forces to retain the sustainable flow structure. Considering this, the non-tumble intake  $\dot{K}_{nonrot}$  and kinetic energy produced by exhaust backflow  $\dot{K}_{ex}$  are dissipated directly for the simplicity of the model; however, some portions are recovered to adjust the local quantities of turbulence using the validation constant  $C_{non}$  and  $C_{ex}$  in Eq. (3.3). Here,  $\dot{k}_{den}$ , defined as  $\dot{k}_{den} = \frac{2}{3}(k\dot{\rho}_{in}/\rho_{in} - \nu_t(\dot{\rho}_{in}/\rho_{in})^2)$ , where  $\rho_{in}$  and  $\nu_t$  are the in-cylinder density and turbulent viscosity, respectively. This term is included in  $\dot{k}_{nonrot}$  in Eq. (3.3).

As turbulent properties obtained from the 3D CFD simulations significantly depend on numerical schemes such as mesh refining techniques and turbulence solvers, they differ quantitatively at discrete schemes irrespective of identical

operating conditions. Hence, in order to increase the controllability required to adjust the changeable values for the 0D dissipation model, a simple one-equation model in Eq. (3.4) is employed instead of the widely applied  $k$ - $\varepsilon$  model. Detailed analyses on the dependency of turbulence on numerical schemes and the methodology for specifying integral length scale  $l_t$  are presented in the following subsection.

In this chapter, the modeling procedures for each term in Eqs. (3.1)–(3.4) are delineated. Specifically, Section 3.2 proposes a methodology to determine the effective flow area to accurately quantify the kinetic energy intake  $\dot{K}_{in}$  introduced into the cylinder and further describes the process of splitting  $\dot{K}_{in}$  into  $\dot{K}_{rot,in}$  and  $\dot{K}_{nonrot}$  by using a loss coefficient. Section 3.3 proposes the model for the turbulence production from tumble energy  $\dot{k}_{rot}$ . Lastly, Section 3.4 proposes the model for spinning up  $\dot{K}_{spin}$  which intensifies tumble energy during compression.

### **3.1.3. Dependency of the turbulent properties on numerical schemes**

To investigate the dependency of the turbulent properties on numerical schemes, the author exploited properties obtained in a previous study through 3D CFD simulations (refer to the Port A results in Figs. 19 and 20 in [91]), whose engine conditions are identical to that of case 4 in this study but with different commercial software and mesh solvers. As shown in Fig. 3.2, the noticeable differences in the quantities of integral length scales and turbulent intensities were observed. The lower integral length scale in case 4 of this study indicates the higher dissipation rate, resulting in a lower turbulent intensity. Meanwhile, the cause for the discrepancy of tumble energy is supposed to be the change in turbulent viscosity  $\nu_t$  with varying turbulent intensity. Due to the variability of the properties with numerical schemes, therefore,

the intuitively manageable one-equation model is adopted for the dissipation model in this study to increase the controllability of turbulent properties.

Further, the integral length scale, which is the largest turbulence scale, should be prescribed to determine the extent of dissipation rate during simulation. The emphasis is on accurately predicting the dissipation rate after IVC timing considering a vast majority of turbulence that survive during combustion is produced behind the timing. Given that the finding from Kim et al. [92] states that the local maximum ( $\sim 600^\circ$ ) and minimum ( $\sim 720^\circ$ ) points of integral length scale can be correlated with cylinder volume in various operating conditions, the cubic root of the in-cylinder volume was employed to scale the integral length scale  $l_t$  in this study as

$$l_t = aV_{\text{cyl}}^{1/3} + b, \quad (3.5)$$

where  $V_{\text{cyl}}$  is total in-cylinder volume. Here,  $a$  and  $b$  are the adjusting parameters for the local maximum and minimum points, with values 0.0475 and -0.001, respectively, to match the points of integral length scale in case 1 (see the leftmost of Fig. 3.2). These adjusting parameters are kept constant throughout this study.

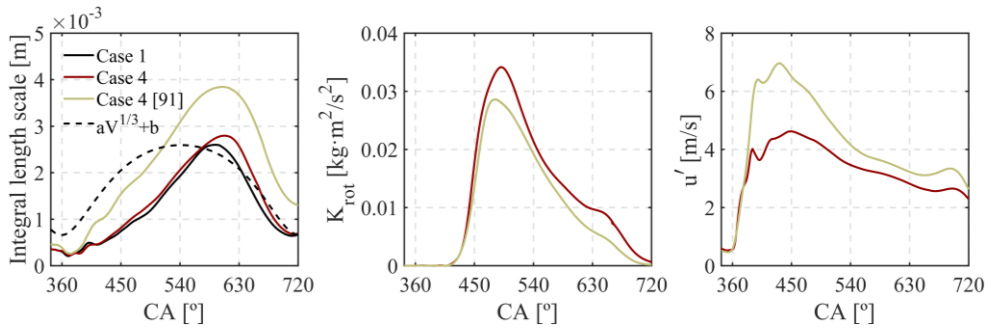


**Figure 3.2** Integral length scale, tumble energy, and turbulent intensity obtained from different numerical schemes.



## 3.2. Intake model

This section covers the models associated with the increase in kinetic energy during the intake process. Given that the valve strategies and intake port design significantly affect the intake characteristics, the models in this section are crucial for reflecting those variances. Moreover, since the amount of kinetic energy determined by the intake process intimately influences the later kinetic energy phenomena during compression, e.g., spinning up, the appropriate intake models should be further emphasized.

Herein, the model for  $\dot{K}_{\text{in}}$  to determine the total kinetic energy intake is proposed based on the analysis of the effective flow area presented in Section 3.2.1. Subsequently, in Section 3.2.2, the division approach for tumble  $\dot{K}_{\text{rot,in}}$  and non-tumble  $\dot{K}_{\text{nonrot}}$  intakes is presented, and loss coefficient is introduced.

### 3.2.1. Determination of the effective flow area

The following expressions show the typical approach to determine the intake velocity  $v_{\text{in}}$  and the resultant kinetic energy intake  $\dot{K}_{\text{in}}$  in 0D simulations:

$$v_{\text{in}} = \frac{\dot{m}_{\text{in}}}{\rho_{\text{in}} A_{\text{eff}}}, \quad \dot{K}_{\text{in}} = \frac{1}{2} \dot{m}_{\text{in}} v_{\text{in}}^2, \quad (3.6)$$

where  $\dot{m}_{\text{in}}$  is mass flow rate and  $A_{\text{eff}}$  is the effective flow area. Therefore, determining the effective flow area dominantly affects intake velocity and thus kinetic energy intake. However, the inaccuracy of  $\dot{K}_{\text{in}}$  could arise since the intake velocity and mass flow rate along the effective flow area are indeed locally different.

As such, in order to correctly calculate  $\dot{K}_{in}$ , integration should be performed on the effective flow area, given as

$$\dot{K}_{in} = \frac{1}{2} \iint_{A_{eff}} \rho v^3 dA, \quad (3.7)$$

where  $\rho$  and  $v$  are the local density and velocity, respectively. As mentioned earlier, this can be hardly achieved in 0D models due to the unknown local properties.

However, the calculations of the kinetic energy intake in the 0D model can be improved by applying the division concept of the valve curtain area. Here, a method using steady CFD simulation is introduced to determine the appropriate effective flow area, thereby improving the calculation of  $\dot{K}_{in}$ . According to the approach by Kim et al. [26], the simulation begins by inducing flow based on the given pressure difference at upstream and downstream boundary conditions. More specifically, an inflow area that is adequately far from the cylinder is selected for the upstream boundary and the piston area is selected for the downstream boundary with total pressures of 1.0 and 0.9 bar, respectively. Each simulation is conducted until the mass flow rates along the valve curtain areas converge at each fixed valve lift case. As depicted in Fig. 3.3, the valve curtain areas are divided into four regions with equal surface areas, and each region is denominated by numbering for convenience purposes, hereinafter described as divisions 1-4. Since the degree of the pressure difference between the boundaries had a negligible effect on the fraction of mass flow rate [26], the total pressures remained unchanged in every simulation.

To save the computational cost of the simulation, the number of cells was diminished by reducing the base grid size and level of AMR as 5 mm and 2, respectively. In contrast, the remaining conditions are configured identically to those

described in Section 2.1.1. The simulation was performed for 6 ms, during which the mass flow rates across the valve curtain area at the divisions converged sufficiently. As a result, the percent deviations of the mass flow rate from the mean values were found to be less than 2% during the last 3 ms.

From the simulation, two intrinsic properties of the designated port geometries are attained at the given valve lifts: discharge coefficients and the fractions of mass flow rate. The discharge coefficient refers to the ratio between the actual and theoretical mass flow rates, where the actual mass flow rate is determined by the average mass flow rate over the last 3 ms of the simulation. On the other hand, the equation for compressible isentropic flow is employed to calculate the theoretical mass flow rate. Since the flow area needs to be specified for the equation, two areas were considered for the calculation: valve curtain area  $A_l$  and the valve area  $A_v$ .

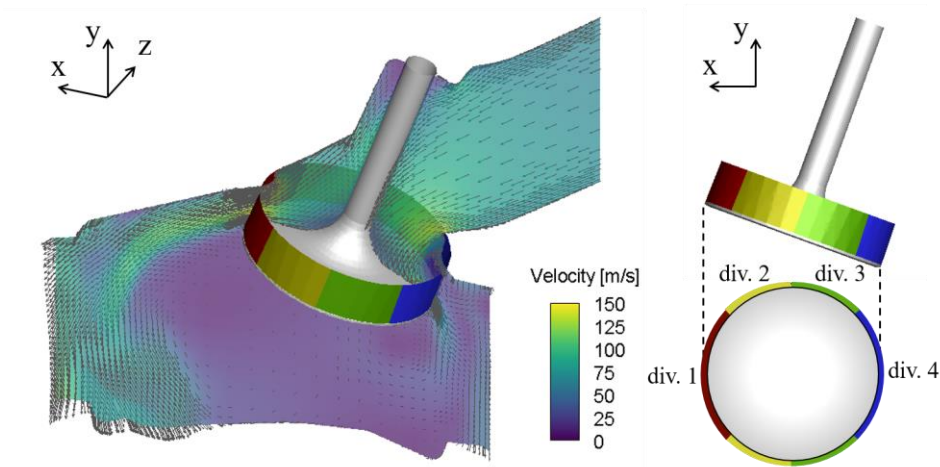


**Figure 3.3** Steady CFD simulation with the valve curtain area divided into four regions: red (division 1), yellow (division 2), green (division 3), and blue (division 4).

Furthermore, provided the valve stem diameter is one-fifth of the valve diameter, one can calculate those areas as

$$A_l = \pi n_v D_{in} l_v, \quad A_v = \frac{\pi}{4} n_v (D_{in}^2 - (0.2 D_{in})^2), \quad (3.8)$$

where  $n_v$ ,  $D_{in}$ , and  $l_v$  are the number of valves, intake valve diameter, and valve lift, respectively. Therefore, two different discharge coefficients,  $C_{d,l}$  and  $C_{d,v}$ , are obtained by varying the flow area (i.e., the theoretical mass flow rate). Here,  $C_{d,l}$  and  $C_{d,v}$  are determined by employing flow areas  $A_l$  and  $A_v$ , respectively.

Figure 3.4 shows the above properties of the reference case at various valve lifts, i.e., the discharge coefficients and fractions of mass flow rate. As seen in Fig. 3.4(a),  $C_{d,l}$  decreases as the valve lift increases, whereas  $C_{d,v}$  increases until it becomes saturated at a sufficiently high valve lift. From this result, the location of areas with

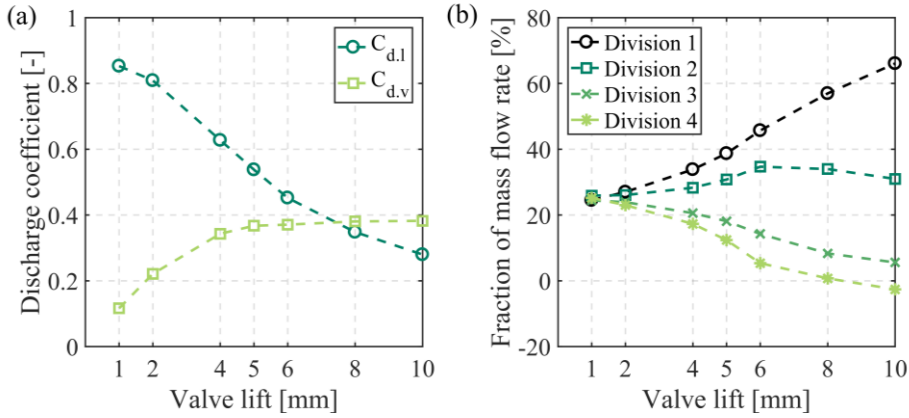


**Figure 3.4** Discharge coefficient (a) and fractions of mass flow rate (b) at the fixed valve lifts obtained from the steady CFD simulation (Reference case).

the restricted flow can be inferred considering the discharge coefficient refers to the extent of area occupied by the flow. It is worth noting that discerning the area with the restricted flow (or fully charged) is of importance since the intake velocity is mostly determined at this location. For instance, as  $C_{d,l}$  is high at lower valve lifts, the flow path is considered to be restricted by the valve curtain area  $A_l$ . The mass flow rate along  $A_l$ , as shown in Fig. 3.4(b), is thus equidistributed at the lower lifts. However, at higher valve lifts,  $C_{d,v}$  increases and approaches an asymptotic value, thereby indicating the restriction of the flow is on  $A_v$  instead of  $A_l$ . Under the circumstances, the mass flow rate eventually concentrates to the upper side of  $A_l$  corresponding to divisions 1-2, leaving behind the rest of the area of  $A_l$ .

Although two discharge coefficients  $C_{d,l}$  and  $C_{d,v}$  are obtained at various valve lifts, the coefficients utilized in the 0D model are the ones representing the maximum allowable flow at a designated flow area. Therefore, the representative discharge coefficients for the valve curtain area and valve area are selected when the valve lift is 2 mm and 10 mm, respectively. In the same manner, the discharge coefficients at different port designs are determined in Table 3.2.

**Table 3.2** Discharge coefficients for the valve curtain area and valve area at different port designs.

Port type	$C_{d,l}$	$C_{d,v}$
A	0.809	0.382
B	0.716	0.497
C	0.743	0.545
D	0.791	0.420
E	0.779	0.415

As in the previous analysis, the valve curtain area and valve area restrict the flow at 2 mm and 10 mm, respectively. However, it should be noted that the transition of the restricted areas at the intermediate valve lift will graduate proceed, not in a dichotomous way. For instance, at the conventional tumble-enhanced port design, where a flow is concentrated on the upper side of the valve curtain area, the flow passing through divisions 1-2 is restricted by the valve curtain area at the intermediate valve lift, whereas the flow at divisions 3-4 is simultaneously restricted by the valve area. This phenomenon can also be identified in the steady CFD results, as shown in Fig. 3.5. Contrary to the 2 mm and 10 mm cases, the flow velocity for the 6 mm case is determined at both the valve curtain area and valve area based on the flow passage.

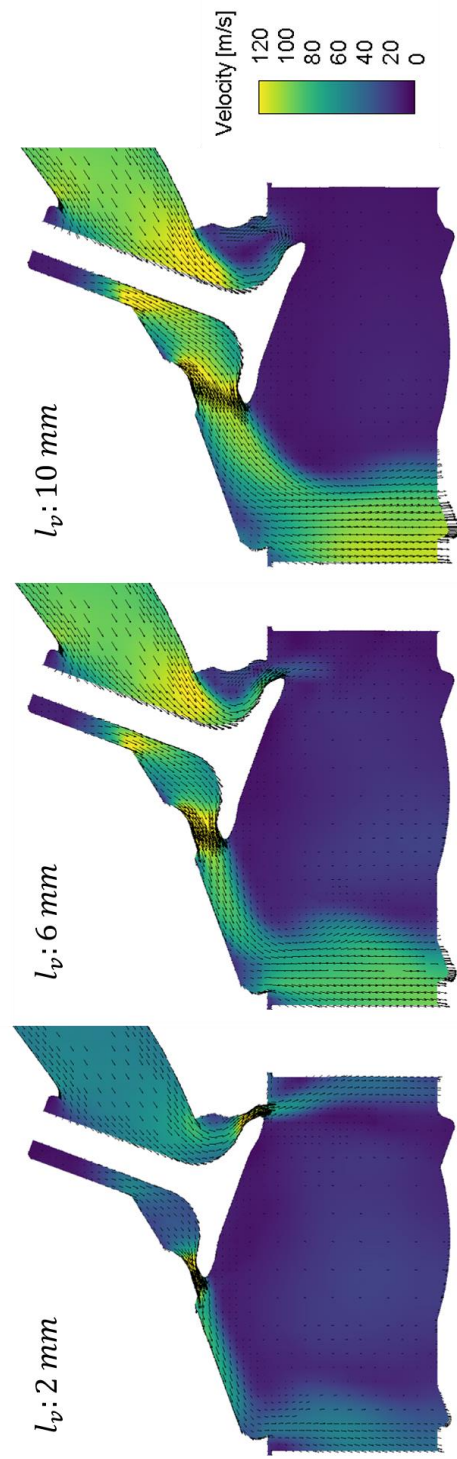


**Figure 3.5** Velocity vector fields at various valve lifts (2 mm, 6 mm, 10 mm) with the engine geometry of the reference case.

In order for the 0D model to consider the transition of the effective area, the valve area is hypothetically divided into four regions by fractions of the mass flow rate at each division of the valve curtain area, as depicted in Eq. (3.9). Subsequently, the minimum flow areas for each division are selected for the effective flow areas as follows:

$$A_{l,i} = \frac{A_l}{n_d}, \quad A_{v,i} = \frac{\dot{m}_{in,i}}{\sum_{i=1}^{n_d} \dot{m}_{in,i}} A_v, \quad (3.9)$$

$$A_{eff,i} = \min(C_{d,l}A_{l,i}, C_{d,v}A_{v,i}), \quad (3.10)$$

where  $n_d$  is the number of divisions (four in this case), and subscript  $i$  is the numbering of the divisions. As a consequence, the intake velocity at each division and the total kinetic energy intake are determined as

$$v_{in,i} = \frac{\dot{m}_{in,i}}{\rho_{in}A_{eff,i}}, \quad \dot{K}_{in} = \sum_{i=1}^{n_d} \frac{1}{2} \dot{m}_{in,i} v_{in,i}^2. \quad (3.11)$$

To verify the above model, the results of the effective flow areas of the steady CFD results were compared with that of the 0D simulation. Specifically, in the CFD simulation, the areas having flow velocity beyond the designated magnitude at each division of the valve curtain area were considered as the effective flow areas by determining the cutoff velocity as half of the surface-averaged intake velocity across the valve curtain area. This is because the areas having sufficient velocity magnitude were occupied by flows.

Figure 3.6 shows the results of the effective flow areas obtained from the steady CFD and 0D simulation results. The solid lines and markers indicate the 0D and CFD



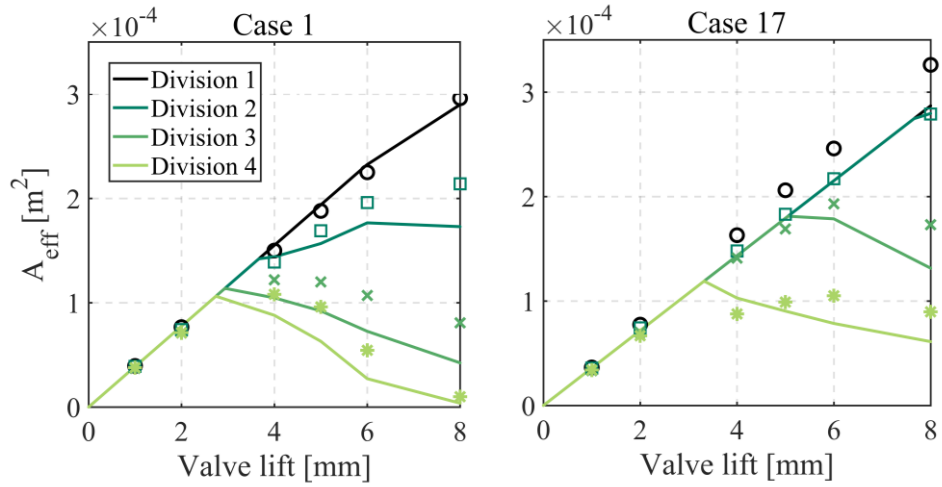


**Figure 3.6** Comparison of the effective flow areas obtained from different port designs. The solid lines and markers indicate the quantities obtained from the 0D and CFD simulations, respectively, with the assumption of cutoff velocity.

results of the effective flow areas at the instantaneous valve lift during simulation, respectively. Given that the effective flow areas differ appreciably with the discrete port designs (i.e., different discharge coefficients, fractions of the mass flow rate, and the intake valve diameter), cases 1 and 17 were compared. In the figure, slight underestimations of the areas were observed for the 0D results, which seem to be caused by the uncertainty of the cutoff velocity used in the CFD simulation. Nonetheless, the overall tendency of the results showed satisfactory agreement in both simulations, thereby verifying the proposed intake model.

### 3.2.2. Loss coefficient

Although an approach to determine the appropriate effective flow areas and the quantity of kinetic energy intake was previously proposed, not all kinetic energy intake can contribute towards generating a sustainable tumble structure. Therefore,

the losses of tumble intake will be investigated, thereby establishing a complete intake model.

Herein, two major losses of tumble intake are considered in the model. First is reverse tumble, a counter-rotating motion against tumble, formed when the flow passes through the lower side of the valve curtain area corresponding to divisions 3-4. Since reverse tumble disturbs tumble formation, as discussed in Section 2.1, tumble intake is modeled to decrease based on the amount of reverse tumble intake. Tumble intake  $\dot{K}_{\text{rot,in}}$  and non-tumble intake  $\dot{K}_{\text{nonrot}}$  are accordingly expressed as

$$\dot{K}_{\text{rot,in}} = \frac{1}{2} \left( \sum_{i=1}^2 C_{\text{loss},i} \dot{m}_{\text{in},i} v_{\text{in},i}^2 - \sum_{i=3}^4 C_{\text{loss},i} \dot{m}_{\text{in},i} v_{\text{in},i}^2 \right), \quad (3.12)$$

$$\dot{K}_{\text{nonrot}} = \dot{K}_{\text{in}} - \dot{K}_{\text{rot,in}}. \quad (3.13)$$

However, Eq. (3.12) includes the loss coefficient  $C_{\text{loss},i}$ , which indicates the extent of contribution of the kinetic energy intake in tumble energy. This loss coefficient will be discussed in detail below.

In earlier 0D models, much effort has been made to adjust (generally reduce) the quantity of MKE or the angular momentum during the intake period. The most common method for this was using tuning constants [9, 10, 13, 14]. Further, there was a study that attempted to utilize a correction factor, which is the function of cylinder geometric information [92].

Meanwhile, several studies have attempted to provide the physical rationale behind the loss of these quantities. Grasreiner et al. [9] explained that the loss originated from the abrupt dissipation of the intake flow. Kim et al. [92] argued that

the loss is attributed to the small vortices generated during the early intake period near the intake valves. The common statement posed by these studies is the location of the loss adjacent to the intake valves.

Similar to the previous analyses, high dissipation rates were observed near the intake valves in the steady CFD results, as shown in Fig. 3.7. However, this intense local dissipation is hardly reproduced by 0D simulations using the typical dissipation models, thereby leading to the overestimation of the in-cylinder kinetic energy. Therefore, in this study, the tumble intake is reduced beforehand by the loss coefficient to appropriately quantify the tumble intake.

It is evident that the loss mostly arises from the frictional force of intake gas. Given that the decaying rate of a Newtonian fluid is proportional to the square of the velocity gradient, a higher kinetic energy loss is generated from the higher speed or narrower flow height along the valve curtain area. Concerning the speed of intake gas, as can be identified in Eqs. (3.12) and (3.13), the kinetic energy loss, which is equivalent to  $\dot{K}_{\text{nonrot}}$ , increases as the rate of change of kinetic energy intake increases at a given value of the loss coefficient; the kinetic energy loss is set proportional to the squared velocity of intake gas. Accordingly, it can be concluded that the loss attributed to the speed of intake gas is reflected priorly in Eq. (3.12). Therefore, other losses irrelevant to the speed of intake gas will be discussed and reflected in the loss coefficient.

First, the effect of flow restriction at the valve curtain area is considered. When seeing the upper sides of the valve curtain areas in Fig. 3.7, high kinetic energy losses are readily observed around the valve boundaries. This is because flow tends to generate large velocity gradients adjacent to walls, particularly when the flow is restricted to that region. Accordingly, the proportion of the kinetic energy loss will

decrease as the instantaneous valve lift increases due to the reduced proportion of the intake flow affected by the wall boundary. Furthermore, the proportion of the loss will asymptotically reach a saturation value when the flow is no longer restricted by the valve curtain area.

Second, the effect of the effective flow area is considered. This effect can be easily identified in the 6 mm valve lift case, shown in Figs. 3.5 and 3.7. More specifically, as can be seen in Fig. 3.5, the flow located on the lower side of the intake valve exhibits a smaller effective flow area, resulting in a narrower flow height and thus a larger velocity gradient, compared to the flow on the upper side. As such, a higher dissipation rate is observed at the flow on the lower side in Fig. 3.7. Here, it was concluded that the smaller the effective flow area, the higher the kinetic energy loss.

To reflect on these losses, the loss coefficient was modeled to exhibit a higher loss in the kinetic energy intake for a narrower effective flow area, as depicted in the numerator of Eq. (3.14). Note that  $C_{\text{loss},i}$  represents the portion of the kinetic energy intake that becomes tumble energy intake, i.e., the lower the value, the higher the loss. Subsequently, the effective flow areas are further normalized by the valve area around the valve stem. This normalization comprises physical implications considering the valve area with larger flow capacity has the higher instantaneous valve lift wherein the transition of the restricted area occurs, provided the other conditions are identical. This propensity can be identified in the cases with different port designs, shown in Fig. 3.6. In the figure, it was revealed that the transition at each division, which corresponds to the deflection point of the solid line, occurs at higher valve lifts in case 17, whose flow capacity of the valve area is larger than that of case 1. Owing to the elongated restriction at the valve curtain area, a larger portion of kinetic energy loss can be generated in the cases with a larger flow capacity in the

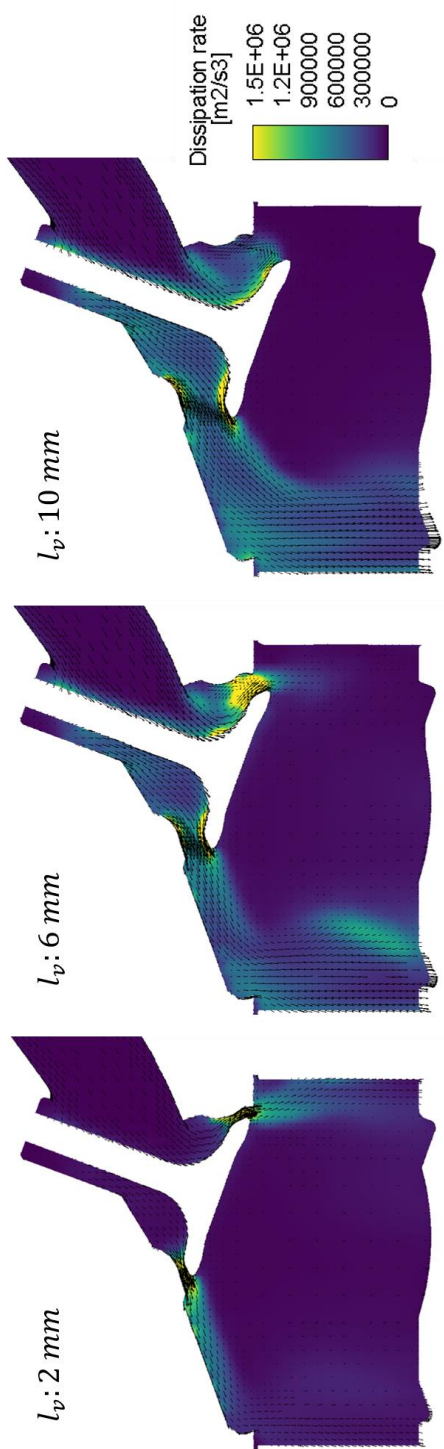


**Figure 3.7** Dissipation rate at different valve lifts (2 mm, 6 mm, and 10 mm) with the engine geometry of the reference case.

valve area. The function for the loss coefficient is therefore determined as

$$C_{\text{loss},i} = \text{erf} \left( C_l \left( \frac{A_{\text{eff},i}}{C_{d,v}A_v} \right)^{n_l} \right). \quad (3.14)$$

The validation constant  $C_l$  is adjusted to balance the amount of reduction, and  $n_l$ , which determines the sensitivity of the ratio between the effective flow and valve areas, is empirically chosen as two in the model.

In this modeling approach, when intake flow is restricted to the valve curtain area ( $A_{\text{eff},i} = C_{d,l}A_{l,i}$ ), the coefficient increases (i.e., a kinetic energy loss decreases) as the instantaneous valve lift increases, reproducing the reduced proportion of the intake flow affected by a valve boundary. On the other hand, when the effective flow area becomes the valve area ( $A_{\text{eff},i} = C_{d,v}A_{v,i}$ ) with the sufficiently high valve lift, the coefficient becomes the only function of the fraction of mass flow rate at each division. More specifically, the lower the fraction of mass flow rate at each division, the higher the decaying rate, indicating the narrower flow height. It also denotes that the coefficient becomes independent of the properties of intake valves in such conditions, presuming that the flow is no longer affected by the valves and is determined by their upstream. Therefore, by individually adopting the coefficient at each division, the aforementioned losses of intake flow can eventually be reflected in the proposed model.

Further, the utility of the loss coefficient is verified in the following paragraphs. It is worth noting first that the two peaks of tumble energy generally occur during one cycle; the first peak is generated by the tumble intake during the intake stroke, whereas the second peak is generated by spinning up during the compression stroke, as exemplified in Fig. 13 later. Since the loss coefficient primarily affects the intake

process, the fractions of accumulated kinetic energy intake during the intake period and the first peaks of tumble energy were used to verify the model. Figures 3.8(a) and (b) show the simulation results with and without the loss coefficient in Eq. (14), respectively. For the latter, a single tuning constant was used to determine the loss, which was the common method applied to the previous models. The value of the tuning constant was chosen such that it matched the first peak of tumble energy of the reference case. In the figure on the left,  $K_{\text{rot,cum}}$ ,  $k_{\text{non,cum}}$ , and  $K_{\text{loss,cum}}$

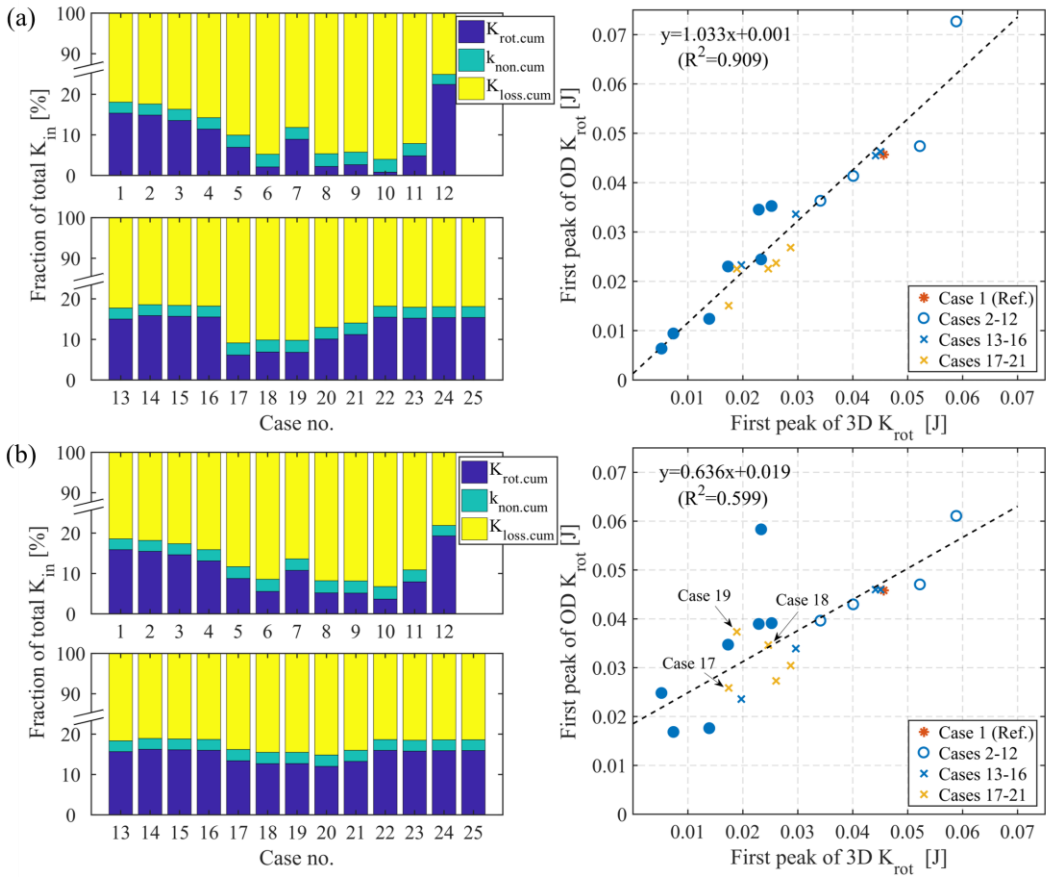


**Figure 3.8** The fractions of accumulated kinetic energy intake from the 0D simulation (left) and the first peaks of tumble energy for the 3D CFD and 0D simulations (right): (a) 0D results with loss coefficient in Eq. (3.14), (b) 0D results with a single tuning constant.

indicate the cumulative quantities during the intake period, which present tumble energy, TKE from non-tumble energy, and the directly dissipated energy, respectively. Considering that the proportions of the cumulative quantities in cases 22–25, which are different intake manifold pressure and engine speed cases, do not differ significantly from that of the reference case, and that the quantities of the first peaks of tumble energy were too high compared to the other peaks, their results were excluded in the figure on the right for descriptive purposes.

It is readily seen that the overall lower quantities of  $K_{\text{rot,cum}}$  is visible in the former simulation shown in Fig. 3.8(a), compared to the latter shown in Fig. 3.8(b), particularly for cases 5-11 and 17-19. Firstly, for cases with late IVO and low valve lift (corresponding to cases 5-11), as the loss coefficient decreases the tumble intake when the instantaneous valve lift is low (i.e., narrow flow heights), the tumble intake during the early intake period decreases intensively, resulting in the lower first peak of tumble energy. Particularly, the decrease in late IVO cases is severe because a large portion of intake mass is rapidly introduced into the cylinder at the lower instantaneous valve lift. By adopting the loss coefficient, therefore, the first peaks of cases 5-11, denoted by filled circles in the figure, are predicted closely to those of 3D CFD in Fig. 3.8(a).

Secondly, the finding of lower tumble intake for cases 17-19 (with Port B and C) is noteworthy considering their valve profiles are identical to that of the reference case (with Port A). Interestingly, the reduction in those cases is attributed to the large flow capacity of the valve area due to the relatively high values of  $C_{d,v}$  (compare the values of Port A-C in Table 3.2). As mentioned earlier, since the flow passing the valve area with a large flow capacity is prone to be restricted by the valve curtain areas, rather than the valve area, the decrease in tumble energy can be attributed to the circumferential increase in the flow area contact with the valve boundary, which



is subjected to a large velocity gradient. As the simulation using a single tuning constant is not capable of reflecting these phenomena, it eventually fails to predict the peaks of tumble energy, yielding higher tumble energies compared to 3D CFD, as shown in Fig. 3.8(b).

### 3.3. Turbulence production model

As for the turbulence production from tumble energy, the model previously developed by Kim et al. [8] was used. Below is a brief explanation of the development of the model.

The model is primarily developed by the virtual velocity field imitating the tumble structure. The velocity field, called the “barrel swirl” function, was first proposed by Benjamin [4, 5] and later modified by Kim et al. [8] to reflect the vortex breakdown of tumble. The equations for modified barrel swirl is given as

$$U_x = 2U \left( 1 - \frac{4z^2}{B^2} \right) \frac{y}{H}, \quad U_y = -2U \frac{H}{B^2} x, \quad U_z = 0, \quad (3.15)$$

where  $U_x$ ,  $U_y$ ,  $U_z$ ,  $U$ ,  $B$ , and  $H$  are the x-dir velocity, y-dir velocity, z-dir velocity, maximum x-dir speed, bore, and instantaneous cylinder height, respectively.

For simplicity, the geometries of the pent-roof head and piston are neglected, and the cylindrical shape of the engine is assumed. Subsequently, the three-dimensional velocity structures were built using Eq. (3.15), as shown in Fig. 3.9. The velocity structure described in the figure varies according to the ratio of bore to instantaneous height to satisfy the mass conservation at that moment, which is consistent with the theory in Section 2.3. Since the x-dir velocity magnitudes become

faster at the lower instantaneous cylinder height with the modified barrel swirl function, the vortex breakdown phenomenon, which is the rapid decaying of tumble energy near the end of the compression stroke, can be reproduced in this model.

In order for the 0D simulation to utilize the structure depicted in Eq. (3.15),  $U$  in this model should be adjusted to have an identical amount of instantaneous tumble energy calculated during simulation. To this end,  $U$  is substituted by the function of  $K_{\text{rot}}$ ,  $B$ , and  $H$ . Subsequently, by applying the closure equation of turbulent viscosity of RANS, the total in-cylinder decaying rate  $\dot{k}_{\text{rot}}$  is acquired from the virtual velocity field, expressed as

$$\dot{k}_{\text{rot}} = \nu_t K_{\text{rot}} \frac{120B^2 + 192H^4/B^2 - 288H^2 + 64H^2}{5B^2H^2 + 6H^4}. \quad (3.16)$$

Further, the correcting factor  $n$  was introduced in the model to reflect the non-linear velocity profile of tumble since the original virtual velocity field is structured with linear velocity profiles in x- and y-directions, as in Eq. (3.15). The factor proposed earlier [8] was additionally modified to improve the applicability of the model in this study. More specifically, the original numerator and denominator of the factor, each representing the geometric size of the cylinder and width of tumble flow, are replaced with the in-cylinder volume and mean value of the two representative valve lifts, respectively.

Therefore, the model developed is given as

$$n = C_{\text{prod}} \frac{V_{\text{cyl}}^{\frac{1}{3}}}{C_{d,l}(l_{v,\text{max}} + l_{v,\text{min}})/2}, \quad (3.17)$$

$$\begin{aligned}
& \dot{k}_{\text{rot}} \\
& = \nu_t K_{\text{rot}} \frac{\frac{2n+1}{2n-1} \cdot \frac{n^2}{3} \cdot \left(120B^2 + 192\frac{H^4}{B^2}\right) - \frac{2n+1}{3} \cdot 288H^2 + 64H^2}{5B^2H^2 + 6H^4} \quad (3.18)
\end{aligned}$$

where  $l_{v,\text{max}}$ , and  $l_{v,\text{min}}$  are the maximum and minimum valve lifts for the generation of tumble, respectively, and  $C_{\text{prod}}$  is the validation constant. The minimum valve lift, where the tumble energy starts increasing in all simulated cases, is set as 4 mm. Here, the common definition of turbulent viscosity  $\nu_t$  in the  $k\text{-}\varepsilon$  model is exploited:  $\nu_t = C_\mu k^2/\varepsilon$ . The constant  $C_\mu$  is 0.0845, which is identical to 3D CFD.

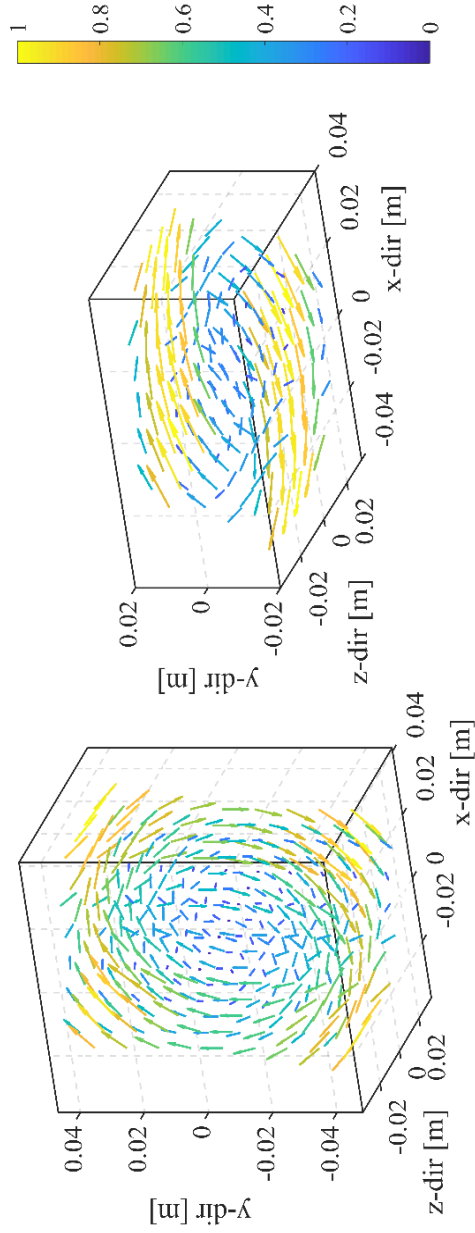


**Figure 3.9** 3D virtual velocity fields (modified barrel swirl) for the turbulence production model. Each cylinder height is 80 mm (left) and 30 mm (right), and the bore is 75.6 mm. The colors in the scale bar indicate the relative magnitudes of velocity normalized by the maximum velocity.

### 3.4. Spinning up model

The spinning up model is built upon the kinetic energy theory proposed in Section 2.4. During the compression stroke, kinetic energy of the in-cylinder charge can increase as the piston accelerates, and vice versa. Therefore, the net variance of kinetic energy during compression is expected to be approximately zero, considering the piston accelerates during the early compression stroke and begins decelerating during the middle, which counterbalances each effect. Notwithstanding this argument, as shown in Fig. 3.10, the accumulated energy, which is the sum of MKE, TKE, and accumulated dissipation, exhibits a net increase at the end of the compression stroke, indicating that the interaction between the flow and the piston is not uniform throughout, but that there is a certain imbalance in the force field and thus the additional tumble flow (or spinning up) induced by the piston. Hence, the increment in the accumulated energy is equivalent to the amount of tumble spinning up. Note that the analysis is conducted after IVC due to the difficulty in conducting an exact evaluation of the increase in kinetic energy while the valves are opened.

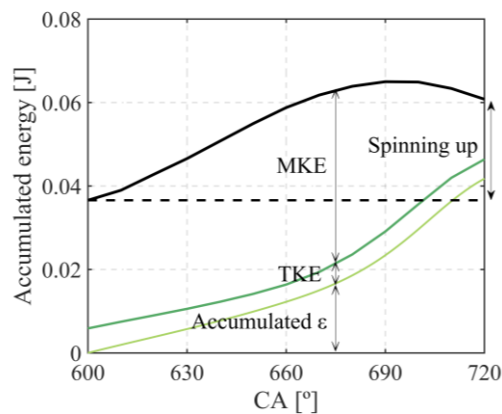


**Figure 3.10** Accumulated energy and spinning up after IVC at the reference case obtained from 3D CFD.

In order to characterize the imbalance of the force field exerted by the piston on the in-cylinder gas, the following pedagogical model was proposed in Section 2.4. Firstly, the in-cylinder velocity profile at the horizontal plane of the geometrical tumble center is hypothetically divided into two velocity fields, the tumble velocity and piston-induced velocity in Fig. 3.11, in order to satisfy mass conservation during compression. Here, the frictional force in the hypothetical tumble velocity field is shown in red arrows, which is opposing the direction of the velocity. This frictional force is caused by the turbulent viscosity and the wall effect in real situation, but the latter is omitted for simplicity of further discussion.

As mentioned earlier, if the piston-induced force field is uniform, i.e., only influencing the piston-induced velocity, then this will not lead to a net change of the rotational motion. However, when piston-induced velocity is added to tumble velocity, an asymmetry arises in the in-cylinder velocity profile (the rightmost in the figure), giving rise to a deformed region where the resultant direction of velocity is reversed, opposite to the direction of hypothetical tumble velocity at the corresponding region. It is evident that if there is no piston velocity onto the charge, then there is no such deformation. Accordingly, the direction of resultant acceleration at the deformed region, again due to the viscosity and the wall effect, is reversed to the hypothetical force field of the tumble velocity field, as shown in the rightmost panel in Fig. 3.11. As a consequence, in comparing these two force fields, the force field exerted by the piston will not be uniform, but exerts a supplementary force proportional to the frictional force in the deformed region. This non-uniformity is causing the tumble spinning up. Interested readers are referred to Section 2.4 for details. The point, however, is that the intensity of spinning up is related to the frictional force in the deformed region.

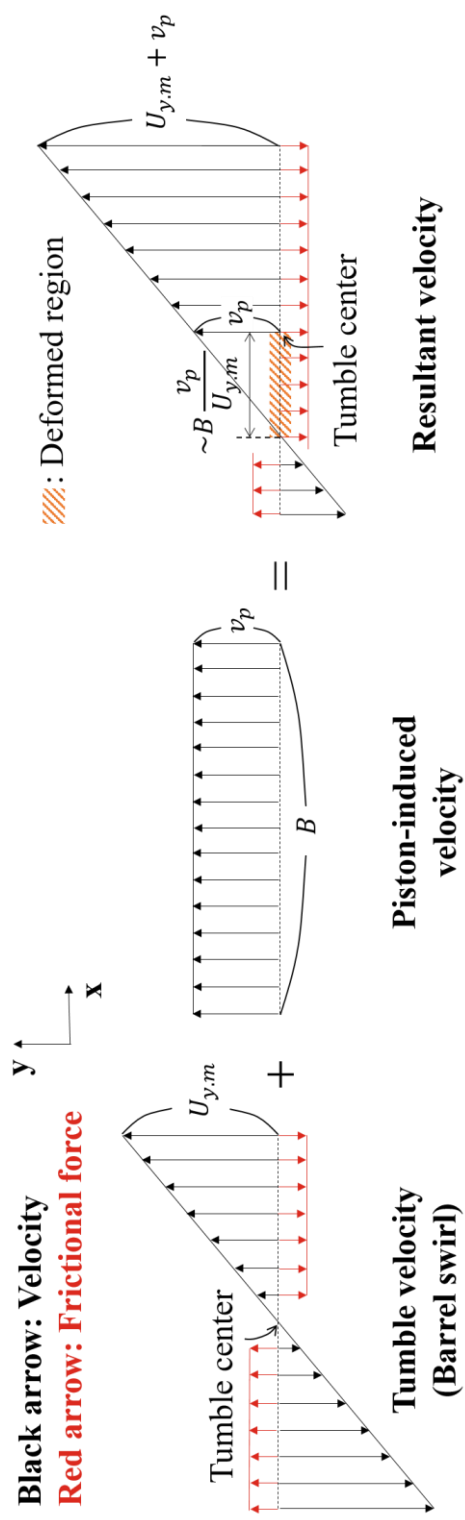


**Figure 3.11** One-dimensional velocity profiles along the line parallel to the x-direction.

Considering the deformed volume (more specifically, the frictional force thereof) is associated with the intensity of spinning up, the volume during compression should be estimated. To inspect the factors affecting the volume, a one-dimensional velocity profile in Fig. 3.11, is first utilized to conduct a simple investigation. In that case, the proportion of the deformed line is calculated as  $v_p/U_{y,m}$  (see the resultant velocity in the figure), where  $v_p$  and  $U_{y,m}$  are the piston speed and maximum y-dir velocity of tumble velocity, respectively. This indicates that the ratio of the piston speed to the y-dir velocity plays a significant role in determining the deformed region. It is nevertheless worth noting that the actual tumble must not form the linear profile shown in Fig. 3.11, and hence, the linear profile is simply employed here to identify the factors affecting the deformed region. Furthermore, by applying this approach to a three-dimensional modified barrel swirl structure, one could obtain the analytical solution of the ratio of deformed volume  $V_{\text{def}}$  to the total in-cylinder volume  $V_{\text{cyl}}$ , given as

$$\begin{aligned} \frac{V_{\text{def}}}{V_{\text{cyl}}} = & \frac{1}{3\pi} \sqrt{1 - \left(\frac{v_p}{U_{y,m}}\right)^2} \left(2 \frac{U_{y,m}}{v_p} + \frac{v_p}{U_{y,m}}\right) \\ & + \frac{1}{\pi} \tan^{-1} \left( \left(\frac{U_{y,m}}{v_p}\right)^2 - 1 \right)^{-\frac{1}{2}} \\ & - \frac{2}{3\pi} \frac{U_{y,m}}{v_p} \quad \text{if } \frac{v_p}{U_{y,m}} < 1, \end{aligned} \quad (3.19)$$

$$\frac{V_{\text{def}}}{V_{\text{cyl}}} = \frac{1}{2} - \frac{2}{3\pi} \frac{U_{y,m}}{v_p} \quad \text{if } \frac{v_p}{U_{y,m}} \geq 1. \quad (3.20)$$

The above equations quantify the proportion of the region experiencing spinning up and approach one-half asymptotically by increasing the ratio  $v_p/U_{y,m}$ . However, there are two limitations to when the deformed volume is postulated to be



directly proportional to the intensity of spinning up. First, compared to the modified barrel swirl function, the actual in-cylinder velocity profile does not have a linear shape, indicating that the proportion of the deformed region is not identical to that depicted in Eqs. (3.19)-(3.20). Second, provided the profile is non-linear, the decaying rate or frictional force at the deformed area is not equidistributed throughout the cylinder. Therefore, the intensity of spinning up may not be proportional to the ratio in Eqs. (3.19)-(3.20).

In that respect, an error function is proposed to reproduce the activation degree of spinning up in a non-linear way, as shown in Eq. (3.21), with  $v_p/U_{y,m}$ . Furthermore, the frictional force from the deformed region is represented by the turbulence production generated by the x-dir gradient of the y-dir velocity at the modified barrel swirl function  $\dot{k}_{\text{rot},y}$  (refer to Eq. (3.16)). Note that the maximum y-dir velocity at the modified barrel swirl function,  $U_y(x = B/2)$  in Eq. (3.15) was determined as  $U_{y,m}$ . The model is eventually developed as

$$\dot{K}_{\text{spin}} = C_{\text{spin}} \dot{k}_{\text{rot},y} \operatorname{erf}\left(a_{\text{spin}} \frac{v_p}{U_{y,m}}\right), \quad (3.21)$$

where

$$\dot{k}_{\text{rot},y} = \nu_t K_{\text{rot}} \frac{192H^4}{5B^4H^2 + 6B^2H^4}, \quad (3.22)$$

$$U_{y,m} = U \frac{H}{B} = \sqrt{\frac{192K_{\text{rot}}}{\rho\pi(5B^2H + 6H^3)}} \cdot \frac{H}{B}. \quad (3.23)$$

The validation constant  $C_{\text{spin}}$  was used to adjust the second peaks of tumble energy produced by spinning up, whereas  $a_{\text{spin}}$  was empirically considered as two.

It is worth noting that the discussion so far on the spinning up is valid when all valves are closed. While intake valves are open, the intensity of spinning up could be decreased since some parts of the fluid need not form a rotating streamline according to the theory. Albeit a completely discrete phenomenon, it was also observed that the intake backflow in 3D CFD during compression exhibited a higher velocity magnitude, resulting in higher kinetic energy compared to the remaining in-cylinder flow. As both phenomena lower the tumble energy before IVC, it is difficult to distinguish the effects, incorporated in Eq. (3.2) to be reflected by one validation constant  $C_{\text{out}}$ , separately. Therefore, it was determined as 2.4 in the model.

The spinning up model was verified by comparing the accumulated quantities of spinning up obtained from the 3D CFD and 0D simulations. Particularly, the quantities of 3D CFD were defined as the net difference of the accumulated energy between IVC and 720° (TDC), as shown in Fig. 3.10, whereas the quantities of 0D are calculated by integrating the spinning up rate from IVC to 720° during simulation in Eq. (3.21). As a result, an acceptable correlation was observed between the 3D CFD and 0D simulations in Fig. 3.12, thereby verifying the utility of the model.

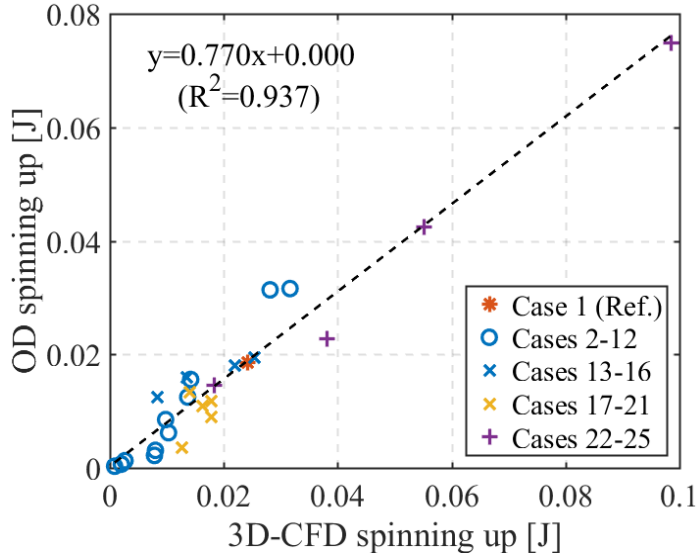


**Figure 3.12** Comparison of the accumulated quantities of spinning up obtained from the 3D CFD and 0D simulations.

## 3.5. Result and discussion

### 3.5.1. Sensitivity analysis of the validation constants

For the proposed models, three validation constants ( $C_{ex}$ ,  $C_{non}$ ,  $C_{rot}$ ) for turbulent intensity and four ( $C_l$ ,  $C_{prod}$ ,  $C_{spin}$ ,  $C_{out}$ ) for tumble energy were employed throughout the simulation. Here, the common definition for turbulent intensity  $u'_{avg} = \sqrt{2k/3m}$  is used. Table 3.3 summarizes the values of the constants. As seen in Fig. 3.13, the constants are used to adjust the quantities of tumble energy and turbulent kinetic energy of the reference case. Furthermore, these constants dominantly affect particular spots on the profiles shown in the figure. In the following analysis, the shifting effects of the constants on the tumble energy and turbulent intensity are investigated by multiplying the weight factors to the constants.

**Table 3.3** Validation constants used in the model.

Validation constant	Value
$C_{ex}$	0.003
$C_{non}$	0.027
$C_{rot}$	0.18
$C_l$	0.82
$C_{prod}$	0.15
$C_{spin}$	5.20
$C_{out}$	2.40

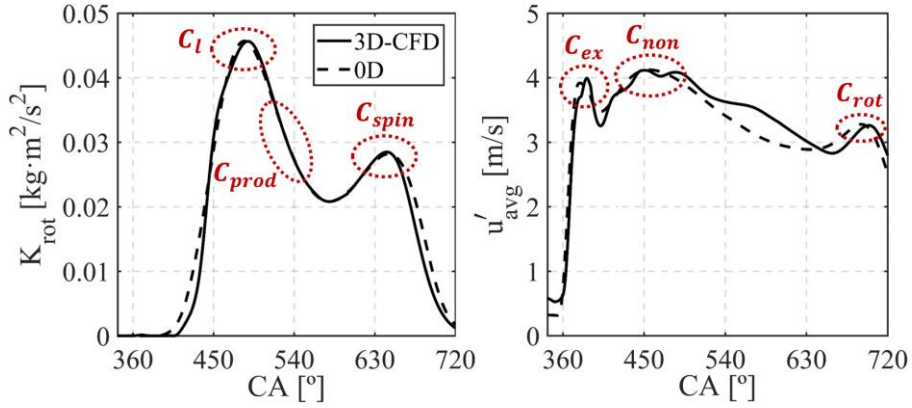


**Figure 3.13** Comparison of tumble energy and turbulent intensity for the reference case.

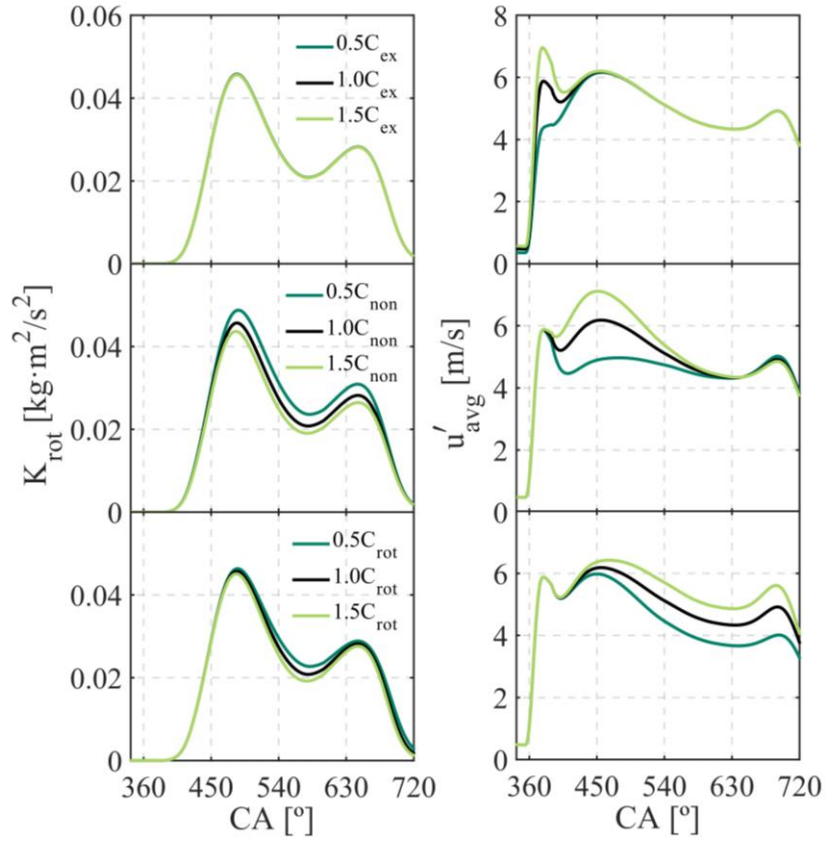
Adjustment methodologies are subsequently suggested in order to secure the generality of the model. Nonetheless, it is worth noting that all only a single set of constants is used throughout the study of all 25 cases in Table 1, except in this subsection.

Figure 3.14 shows the effects of the validation constants of turbulence production and dissipation.  $C_{ex}$  and  $C_{non}$  are the adjusting constants for the intakes of TKE from the exhaust backflow and non-tumble intake, respectively.  $C_{rot}$

is used to adjust the contribution of turbulence production from tumble energy. Although these constants have no direct influence on the quantity of tumble energy, they affect tumble energy by changing the turbulent viscosity. However, relatively minor changes are observed in tumble energy compared to turbulent intensity, as seen in the figure.

In contrast, Fig. 3.15 describes the effects of the validation constants that directly affect tumble energy. Here,  $C_l$  is used to adjust the first peak of tumble energy, considering its significant effect on the intake of tumble energy. Although the first peak is also affected by  $C_{\text{prod}}$ , the preferential adjustment of  $C_l$  is recommended to match the first peak, given that  $C_{\text{prod}}$  controls the overall decaying rate of tumble energy. Specifically, the decaying rate between the first and second peaks (refer to Fig. 3.13) is adjusted using  $C_{\text{prod}}$ . Subsequently,  $C_{\text{spin}}$  is used to adjust the second peak of tumble energy. As mentioned in Section 3.4,  $C_{\text{out}}$  adjusts the combined effects of the reductions on both spinning up and discharge by intake backflow before IVC. It is hence worthwhile to comment that  $C_{\text{out}}$  plays a critical role in differentiating the second peaks of tumble energy at various IVC cases, despite showing marginal changes in Fig. 3.15.

Additionally, the effects of tumble intake and spinning up on the turbulent intensity are explored based on the results shown in Figs. 3.15(a) and (c), with emphasis on the change in turbulent intensity near TDC that dominantly influences combustion. As seen from the figure, the changes in tumble intake and spinning up are mainly involved in the formation of the two peaks of tumble energy, thereby exhibiting considerable effects on the quantities of turbulent intensity near TDC. Therefore, this finding supports the importance of appropriate models for both tumble intake and spinning up.



**Figure 3.14** Tumble energy and turbulent intensity results with validation constants ( $C_{ex}$ ,  $C_{non}$ ,  $C_{rot}$ ) multiplied by weight factors.

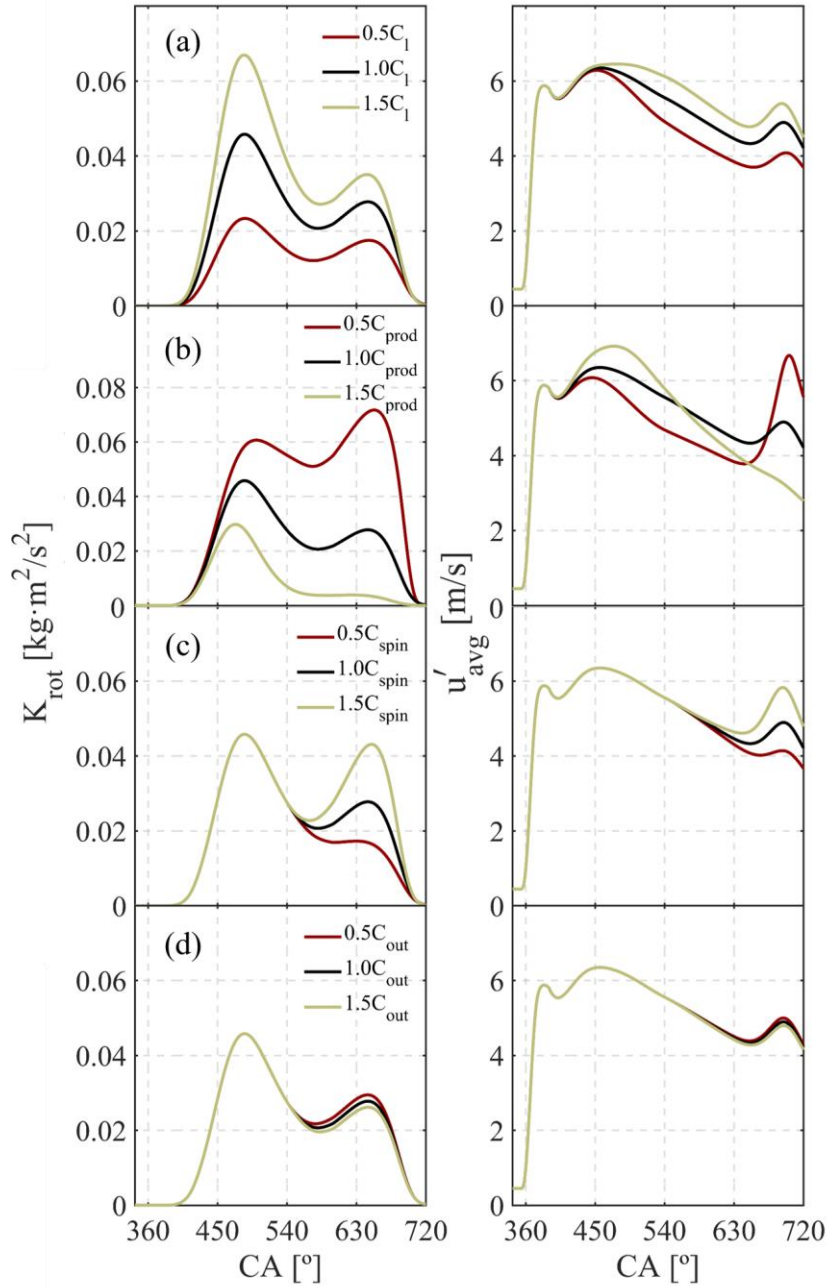


**Figure 3.15** Tumble energy and turbulent intensity of the 0D simulation at different validation constants ( $C_l$ ,  $C_{\text{prod}}$ ,  $C_{\text{spin}}$ ,  $C_{\text{out}}$ ) multiplied by weight factors.

### 3.5.2. Variable valve operation results

Presently, the controllability of valve actuation has significantly improved due to the development of variable valve actuation technologies. Although various valve strategies are activated to primarily control compression/expansion ratios and valve overlap, they significantly influence tumble formation, resulting in non-identical turbulent combustion behaviors in the end. The effects of valve strategies on tumble hence should be accommodated to accurately evaluate combustion in SI engines.

It should be noted that the exhaust valve profile remained unchanged throughout the study, considering the kinetic energy induced by the exhaust valves had a negligible effect on tumble, compared to intake valves. Therefore, as seen in Fig. 3.16, only the cases with varying intake valve profiles were explored with the fixed exhaust valve profile.

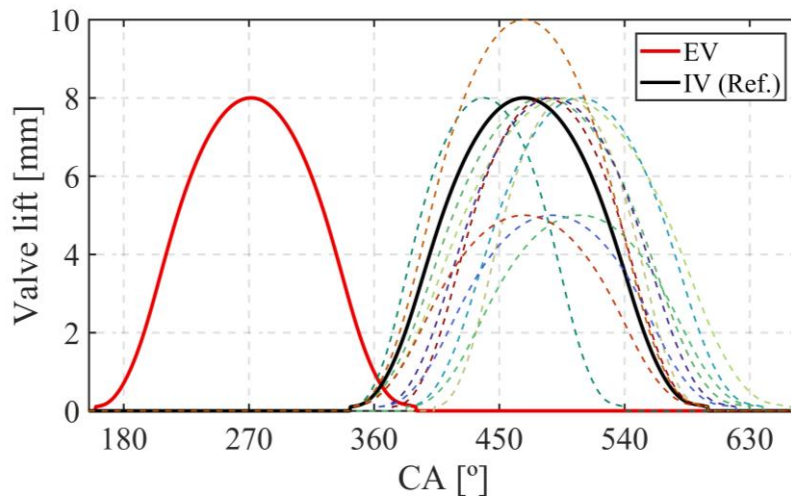


**Figure 3.16** All valve profiles explored in this study. Solid and dashed lines indicate valve profiles in the reference case and the intake valve profiles in cases 2-12, respectively.



The overall results for various valve strategies are presented in Fig. 3.17. The effect of IVC timing on tumble is identified by comparing cases 1-4, shown in the uppermost figures. As discussed in Section 3.4, the combined effect of the weakened spinning up and intake backflow decreases tumble energy in the later IVC cases, thereby lowering the turbulent intensity. These phenomena are mainly captured by using the validation constant  $C_{out}$  in the proposed model.

The effect of IVO timing is revealed by comparing cases 1, 5, and 6. As for the cases with late IVO timings, particularly placed after TDC ( $360^\circ$ ), the intake flow rapidly charges the cylinder and generates momentarily high turbulent intensity in the early intake period. However, this flow has an insignificant contribution to the later turbulent intensity near firing TDC ( $720^\circ$ ) since its kinetic energy is not converted into tumble energy at the lower instantaneous valve lift. This phenomenon is mainly reproduced by adopting two factors in the present model: reverse tumble and loss coefficient.

The effect of the aforementioned factors is distinct in cases 8, 10, and 11, where the lower valve lifts are utilized, and accordingly, the lower quantities of tumble energy are generated. Since the model is capable of reflecting the phenomena concerning the two factors, the 0D quantities of tumble energy and turbulent intensity in cases 7-12 are eventually in good agreement with those of 3D CFD.

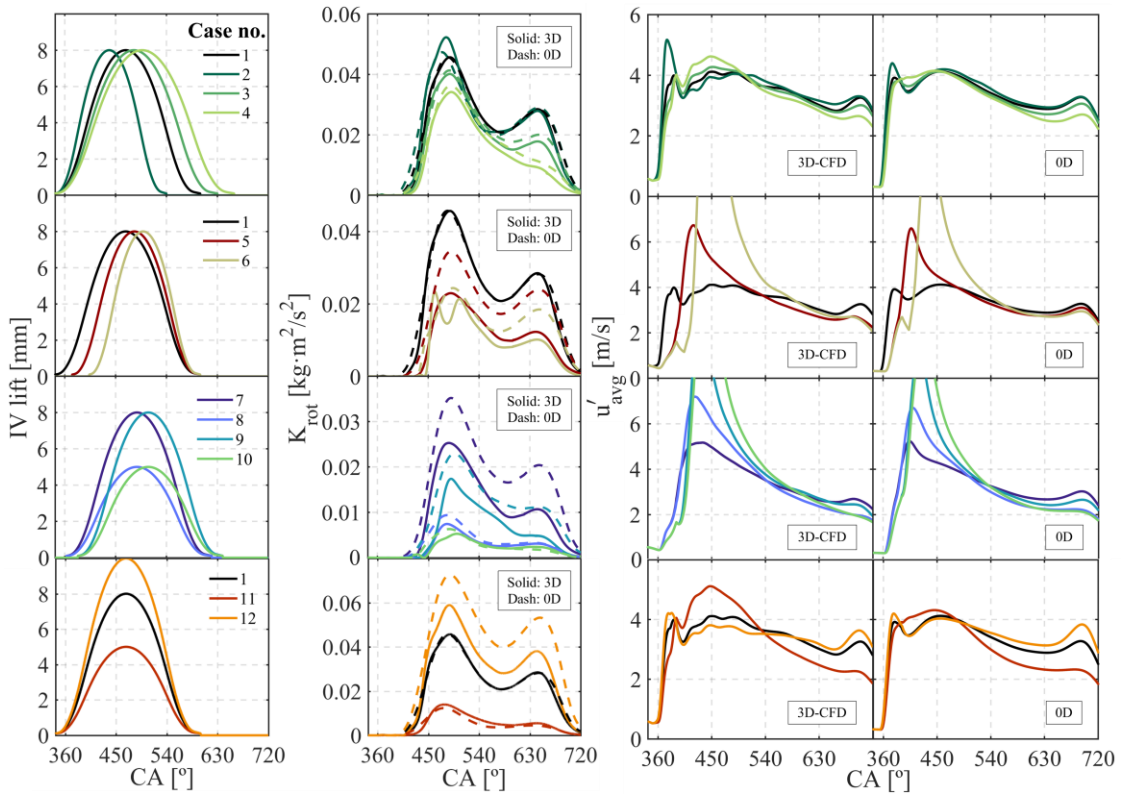


**Figure 3.17** Tumble energy (2nd column) and turbulent intensity (3rd and 4th columns), obtained from the 3D CFD and 0D simulations at various intake valve lift profiles. 1st row: cases with different IVC, 2nd row: cases with different IVO, 3rd and 4th rows: cases with different valve lifts.

### 3.5.3. Engine geometry results

The engine geometries, from the intake port to the cylinder components, affect tumble in several ways. For instance, the intake flow is intrinsically characterized by the designated intake port design before being introduced into the cylinder. The characterized features include the mass flux distribution across the valve curtain area and the mass flow rate associated with the discharge coefficient. These features significantly influence the formation of tumble. Subsequently, the kinetic energy of

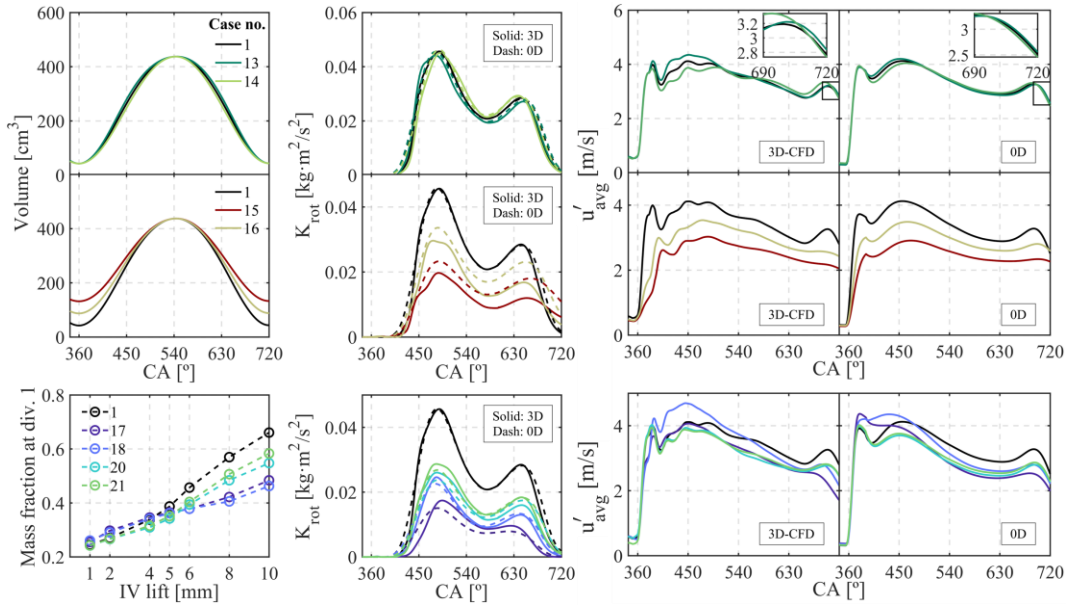
the flow introduced into the cylinder undergoes decaying (or turbulence production), which is the function of the engine cylinder geometries (refer to Eqs. (3.21)-(3.23)). Furthermore, tumble spinning up is exerted on the flow during compression, leading to an increase in its energy. It is worth noting that, despite the complex mechanism of the spinning up, it is an apparent function of the cylinder components. That is, every model should reproduce the aforementioned phenomena to acquire appropriate tumble energy and turbulent intensity for different engine geometry cases.

Figure 3.18 shows the results of cases 13-21 into three sub-categories: connecting rod, stroke, and intake port design. Although marginal changes are observed in the results of the connecting rod (corresponding to cases 1, 13, and 14), they are clearly visible and identified in the figure. Furthermore, the effect of piston speed is realized simultaneously with the effect of compression ratio in cases 1, 15, and 16. Considering the case having a shorter stroke exhibits higher instantaneous height at TDC, the weaker vortex breakdown is observed in that case, thereby resulting in higher tumble energy by the end of the compression stroke. Besides, the intensity of spinning up decreases at a shorter stroke case due to the lowered piston speed, which can be recognized by comparing the increasing rate of tumble energy during compression. As these parameters are reflected in the turbulent production and spinning up models, tumble energies obtained from the 0D simulation closely follow those of the 3D CFD simulation.

Contrary to the previous cases, the cases in the third category exhibit different intake port designs, which are characterized by different discharge coefficients and fractions of mass flow rate at the valve curtain area. Considering this, case 19 is excluded in Fig. 3.18 given that its intake port design is identical to case 18. It is worth stressing that not only the fractions of mass flow rate but the various other

parameters should be considered here for accurately analyzing the outcomes of the first peaks of tumble energy.

Firstly, the larger displacement volumes in cases 17-18 compared to the other cases (by a factor of 5/4) are focused since tumble energy is generally proportional to the displacement volume, provided the remaining conditions are identical. However, contradictory to one's expectation, relatively lower tumble energies in cases 17-18 were observed than the others. Based on the interpretation of the proposed model, two factors seem to substantially reduce tumble energy for those cases: the lower mass flow rate at divisions 1-2 and the relatively higher  $C_{d,v}$  compared to  $C_{d,l}$ .



**Figure 3.18** Tumble energy (2nd column) and turbulent intensity (3rd and 4th columns), obtained from the 3D CFD and 0D simulations with various engine geometries.

1st row: cases with different connecting rods, 2nd row: cases with different strokes, and 3rd row: cases with different intake port designs.

Although evident in the fractions of mass flow rate, the importance of these reductions on the tumble energy based on the relatively high  $C_{d,v}$  (see Table 3.2) should be underlined, considering these reductions are comparable to those of the lower fraction of mass flow rate at divisions 1-2. That is, the loss coefficient in Eq. (3.14) has a significant role in reducing the tumble energy for cases with high  $C_{d,v}$  by elongating the flow restriction at the valve curtain area, thereby increasing the circumferential flow area contact with the valve boundary, which is subjected to high decaying rates. A detailed description of this phenomenon was elaborated in Section 3.2.2. Similarly, by considering the two factors, i.e., the fractions of mass flow rate and the loss coefficient, the tumble energies of cases 20-21 were also able to be predicted successfully.

Further, another interesting finding was observed in comparing cases 17 and 18. Although case 17 is more advantageous for both discharge coefficients and fraction of mass flow rate in the aspect of tumble intake, lower tumble energy is observed. This is attributed to the relatively large intake valve diameter in case 17, which results in a lower intake velocity. As a result of reflecting these phenomena, the tumble energies in cases 1 and 17-21 were predicted successfully.

### **3.5.4. Engine operating condition results**

The intake manifold pressure and engine speed are representing the typical operating conditions in SI engines. Hence, it is crucial to accurately predict these conditions for modeling. In the context of 0D simulations, however, reproducing these conditions is straightforward since the predictions on turbulent properties dominantly depend on the accuracy of the calculated in-cylinder mass. That is, the

predictions are primarily achieved using the conventional compressible isentropic flow equation that solves mass flow rate without the aid of turbulence models.

For instance, the tumble energies at different intake manifold pressures can be reproduced by matching the in-cylinder mass, considering their quantities are nearly proportional to the density of the intake gas. Furthermore, minor changes occur in the quantities of turbulent intensity, which is intensive property given that changes in density have a negligible effect on turbulent viscosity.

For cases with different engine speeds, the quantities of tumble energy and turbulent intensity increase nearly proportionally with the engine speeds. That's because the intake velocity increases proportionally with engine speed, provided the in-cylinder mass is identical at the same crank angle position. However, in Fig. 3.19, the discrepancy of the 0D and 3D CFD simulations at the turbulent intensity during the early intake period ( $360^{\circ}\sim 420^{\circ}$ ) was observed in case 25, which is attributed to the misprediction of the mass flow rate at the corresponding period (refer to the in-cylinder mass of case 25 in Fig. 3.19). This misprediction may have arisen from the unsteadiness of the flow rate at the lower instantaneous lift, which differs from the assumption of a quasi-equilibrium process in the 0D model. This unsteadiness thus leads to inaccuracy at high engine speeds. However, the quantities of turbulent intensity near TDC ( $720^{\circ}$ ) are unperturbed because the deviations do not significantly influence the generation of tumble energy beginning at approximately  $410^{\circ}$ .

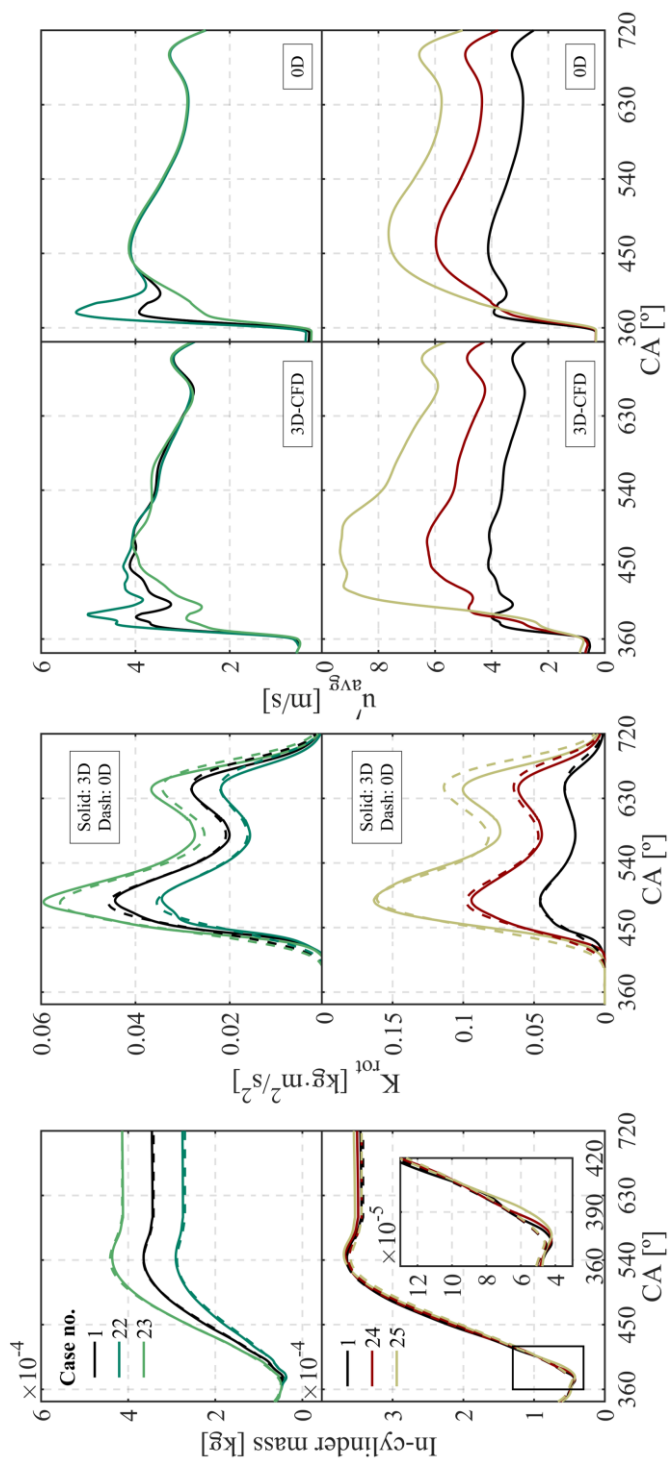


**Figure 3.19** Tumble energy (2nd column) and turbulent intensity (3rd and 4th columns), obtained from the 3D CFD and 0D simulations for different engine operating conditions. 1st row: cases with different intake manifold pressures, 2nd row: cases with different engine speeds.

### 3.5.5. Comparison with GT-power

To further demonstrate the accuracy of the proposed model, a commercial GT-power, a state-of-the-art 0D simulation developed by Gamma Technologies, embedding turbulence model of v2016 [10] was executed to compare the outcomes of the cases listed in Table 3.1. The tumble coefficient, indicating the proportion of tumble intake, is utilized in GT-power to adjust the strength of tumble, which increases monotonously as the intake valve lift increases [93]. Therefore, the coefficient was presumed to be a linear profile starting from zero at zero valve lift and was set to match the tumble ratio of 3D CFD at the IVC timing of the reference case. Meanwhile, the turbulence multipliers were set as default values.

For concise comparison, the quantities of turbulent intensity between 700–720°, which play a significant role in combustion, are averaged based on the crank angle. These average values are plotted as markers, whereas the minimum and maximum values during the period are plotted as error bars, as shown in Fig. 3.20. The left figure shows a comparison of the 3D CFD and 0D simulations with the proposed models, whereas the right figure shows a comparison of the 3D CFD simulation and GT-power applying turbulence model of v2016. Although the results of all cases except cases 24-25 (variations of engine speed) are presented in the proposed model, only the results of Port A (cases 1-16 and 22-23) are presented in GT-power for the sake of impartiality concerning the tuning constants associated with the changes of port design.

As seen in the figure, a clear correlation with 3D CFD was found in the results of the proposed model, with the coefficient of determination  $R^2$  obtained as 0.852. In addition, the lengths of the error bars for both 3D CFD and 0D simulations are



comparable. On the contrary, GT-power does not show any correlation with 3D CFD for the cases investigated in this study.

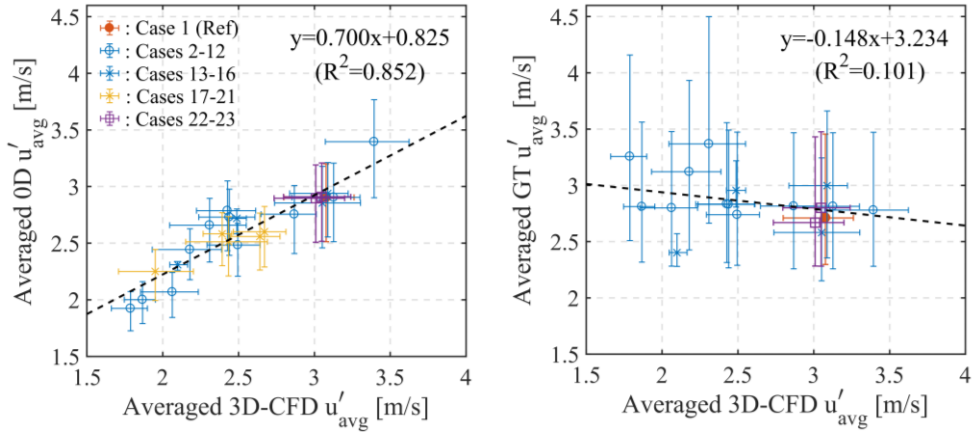


**Figure 3.20** Averaged turbulent intensity using crank angle during 700°(bTDC 20°)~720°(TDC).

## **Chapter 4. COMBUSTION MODEL**

In this chapter, combustion models built upon theories supported by numerous experiments and DNS studies to date are proposed. Note that the turbulent properties exploited in this study are predetermined by the methodologies in Chapter 3, and are not repeated for brevity.

### **4.1. Methodology**

#### **4.1.1. Experimental setup**

Four different gasoline engines equipped with Continuously Variable Valve Timing (CVVT) modules were used for the experiments. With varying valve timing, the operation range was extended immensely considering the amount of internal residual gas and effective compression ratio (and expansion ratio) varies according to the valve strategies, which influences the composition of in-cylinder gas and thermodynamic states.

Table 4.1 summarizes the engine specifications and operating conditions. It is worth noting that engines A-C share almost identical engine geometries, except for the S/B ratios. The detailed experimental setup for engines A-C is documented in [94]. Additionally, the turbulence characteristics of these engines were examined in Chapter 3, which verified the accuracy of turbulence properties in this chapter. In order to investigate the effects of reactant compositions and resultant thermodynamic states during combustion, the non-stoichiometric conditions were explored using engine D.

The AVL combustion analyzer was used for the acquisition of combustion data, including cylinder pressure and combustion durations. In terms of the post-processing, all experimental data in this study were determined by averaging the data of over 300 engine cycles per cylinder, and the cylinder average values were employed for the analysis of a multicylinder engine.

**Table 4.1** Engine specifications and operating conditions

		Engine A	Engine B	Engine C	Engine D	Unit
<b>Engine specifications</b>	No. of cylinders	1	1	1	4	[-]
	S/B ratio	1	1.2	1.47	1.15	[-]
	Bore	86	81	75.6	88.5	[mm]
	Stroke	86	97	111	101.46	[mm]
	Compression ratio	12	12	12	13	[-]
	Displacement volume per cylinder	ca. 500	ca. 500	ca. 500	ca. 624	[cm <sup>3</sup> ]
	No. of valves	4	4	4	4	[-]
	In/ex valve lift	9.5/9.5	9.5/9.5	9.5/9.5	10/10	[mm]
	In/ex valve diameter	33/27	29/27	29/27	36.5/30	[mm]
<b>Operating conditions</b>	Intake valve opening (IVO)	-10 to 40	-5 to 40	-5 to 35	20 to 45	[bTDC]
	Exhaust valve opening (EVO)	19 to 54	19 to 54	24 to 54	27 to 57	[bBDC]
	In/ex valve duration	280/240	280/240	280/240	268/248	[CAD]
	Avg. intake pressure	0.61 to 1.43	0.61 to 1.32	0.63 to 1.33	0.77 to 1.31	[bar]
	Engine speed	1500, 2000	1500, 2000	1500, 2000	1250 to 3000	[RPM]
	Equivalence ratio ( $\phi$ )	1	1	1	0.53 to 0.59	[-]
	Ignition timing	-4.5 to 33	1.5 to 22.5	0 to 21.75	13.8 to 33.4	[bTDC]
	Octane number	91.5	91.5	91.5	92	[-]
	No. of points	98	40	56	51	[-]

### 4.1.2. Simulation setup

A two-zone model was used for the 0D simulation. The model assumes two distinct, burned and unburned zones whose thermodynamic states are determined independently during combustion. The first law of thermodynamics is applied to define each thermodynamic state, whereas the in-cylinder gas is assumed to be an ideal gas for the equation of state. For the modeling heat transfer, the equation proposed by Woschni [95] was exploited.

In order to obtain thermodynamic and transport properties, the Cantera toolbox embedded in Matlab was utilized. Specifically, the reduced gasoline surrogate mechanism with 323 species [96] is applied in this study to determine the non-dimensional factors, such as Lewis number (Le), Markstein number (Ma), and Zel'dovich number (Ze), based on the properties therein. As for the determination of the effective Le, the volume-based approach for the multifuel mixture proposed by Lapalme et al. [97] was used, considering the primary reference fuel (PRF), being binary, is selected as the gasoline surrogate fuel for the simulation. The expression for individual Le for deficient species  $i$  is given as

$$Le_i = \frac{\alpha_i}{D_{i,\text{mix}}}, \quad (4.1)$$

where,

$$D_{i,\text{mix}} = (1 - y_i) / \left( \sum_{\substack{j=1 \\ j \neq i}}^n \frac{x_j}{D_{ij}} \right). \quad (4.2)$$

Here,  $\alpha_i$ ,  $D_{ij}$ ,  $y_i$ , and  $x_i$  are the thermal diffusivity, mass diffusivity, mass fraction, and mole fraction, respectively. Subscript  $j$  denotes the unburned mixture species. Note that when calculating  $\alpha_i$  and  $D_{i,\text{mix}}$  of fuel  $i$ , the composition of the unburned mixture only considers the fuel  $i$ , air, and diluents, while excluding other fuels. Therefore, the effective Lewis number for deficient species can be determined as

$$\text{Le}_{\text{eff}} = \sum_{i=1}^n x_i \text{Le}_i. \quad (4.3)$$

As elaborated in [97], the effective Lewis number within the range of  $0.8 < \phi \leq 1$  is additionally supplemented by combining  $\text{Le}_{\text{eff}}$  for both deficient species and excessive species with the function of  $\text{Ze}$  and  $\phi$ .

For  $\text{Ma}$  and  $\text{Ze}$ , the identical approaches from the study conducted by Demesoukas et al. [24] were utilized. Particularly, the theoretical equation proposed by Bechtold and Matalon [98] was used for  $\text{Ma}$  since it exhibits a fairly good agreement with the experimental data [99] for various gasoline surrogate fuels. However, it is recommended to cautiously use the equation for some fuels, e.g., hydrogen [98], that further deviate from the experimental data. The equation for  $\text{Ma}$  is given as

$$\text{Ma} = \alpha_M - \frac{(\sigma - 1)}{\sigma} \gamma_1, \quad (4.4)$$

where

$$\alpha_M = \gamma_1 + \frac{1}{2} \text{Ze}(\text{Le}_{\text{eff}} - 1)\gamma_2, \quad (4.5)$$

$$\gamma_1 = 2\sigma/(\sqrt{\sigma} + 1), \quad (4.6)$$

$$\gamma_2 = \frac{4}{\sigma - 1} \left\{ \sqrt{\sigma} - 1 - \ln \left( \frac{(\sqrt{\sigma} + 1)}{2} \right) \right\}, \quad (4.7)$$

and  $\sigma$  ( $= \rho_u/\rho_b$ ) is the expansion ratio. Lastly, the equation for Ze proposed by Müller [100] is utilized:

$$\text{Ze} = 4 \frac{T_b - T_u}{T_b - T^0}, \quad (4.8)$$

where  $T^0$  is the crossover temperature, expressed as

$$T^0 = - \frac{E}{\ln \left( \frac{P}{B} \right)}. \quad (4.9)$$

Coefficients  $E$  and  $B$  are determined by the values of the iso-octane documented in Table 1 in [100], whereas  $T_b$  and  $T_u$  stand for the burned and unburned temperatures, respectively.

To simplify the calculation of in-cylinder geometry, a cylindrical shape is assumed while neglecting the pentroof shape of the cylinder head, which is consistent with Chapter 3. Furthermore, the ignition kernel is placed beneath the center of the head according to the actual distance between the spark electrode and the head to appropriately reproduce the flame surface area during the early flame

development phase. Therefore, the flame propagates with the shape of a truncated sphere instead of a hemisphere.

### 4.1.3. Laminar properties

The planar laminar flame speed  $S_L^0$ , the unstretched flame speed at unburned gas, is one of the principal properties of combustion. Although abundant research [54, 99, 101, 102] has been conducted to determine the  $S_L^0$  of gasoline and its surrogate fuels, they have been scarcely explored based on the engine-relevant conditions owing to the existence of hydrodynamic instability at extreme thermodynamic conditions [75]. In this regard, most of the empirical expressions estimate the flame speed by the extrapolation devoid of verification over those conditions. Considering this study covers a broad range of thermodynamic conditions and highly diluted and lean conditions, the deviation owing to extrapolation could be distinct. Therefore, in this study, the expression obtained from the reaction kinetics calculations by Hann et al. [103], specialized for the engine-relevant conditions having a broad range of dilution and equivalence ratios, is exploited to determine the value of  $S_L^0$  instead of using generally applied power-law formulas [101, 104].

As revealed in previous studies [61, 63, 70], since the laminar flame thickness is an important property involving combustion in several ways, it is necessary to accurately determine the thickness for modeling the combustion phenomena. In general, two approaches are used for defining the flame thickness. First, by using the Zel'dovich flame thickness, defined as  $\delta_L^0 \equiv \alpha/S_L^0$ , and second, by using the maximum gradient of various variables, such as  $\delta'_L \equiv (T_b - T_u)/\max(|\nabla T|)$ , when applying temperature. Here,  $\alpha$  denotes the thermal diffusivity of unburned mixture. Although the latter retains the physical meaning of flame structure, it can be only



exploited in studies wherein the combustion properties have been solved within the flame thickness. Considering this, the value of  $\delta_L^0$  is complemented to approximate the latter based on the correlation proposed by Blint [105], given as

$$\delta_L = 2\delta_L^0 \left( \frac{T_b}{T_u} \right)^{0.7}. \quad (4.10)$$

Accordingly, the laminar flame thickness in Eq. (4.10) is utilized in the simulation.

Given that the initial flame is developed from the spark, it inherently propagates spherically and possesses a curved and stretched flame surface. Then, the flame retains the propagating speed different from  $S_L^0$  due to the inequality of mass and thermal diffusivities of the deficient species. In principle, this stretched laminar flame speed  $S_L$  tends to vary linearly according to the stretch rate  $\kappa_s$  comprising information on the curvature, as follows:

$$S_L = S_L^0 - \kappa_s L_b / \sigma, \quad (4.11)$$

where

$$\kappa_s = \left( \frac{2}{r_f} \right) \frac{dr_f}{dt}, \quad L_b = \delta_L^0 \text{Ma}. \quad (4.12)$$

By approximating  $1/\sigma \cdot dr_f/dt$  to  $S_L^0$ , Eqs. (4.11) and (4.12) become

$$S_L = S_L^0 (1 - 2L_b/r_f). \quad (4.13)$$

It is worth noting that despite losing its linearity with  $\kappa_s$ , Eq. (4.13) accurately determines the stretched laminar flame speed of the reactant with  $Le > 1$  compared to Eq. (4.11), as proved by Chen [53]. Therefore, Eq. (4.13) is used to determine the value of  $S_L$  in this study. Note that the approaches used to determine the laminar flame thickness and stretched laminar flame speed are identical to those presented in [24].

#### 4.1.4. Simulation methodology

For the simulation input, the ensemble-averaged pressure profiles based on CAD were used for the intake and exhaust pressures for engines A-C. However, due to the absence of CAD-based data, the average intake and exhaust pressure values were used for engine D. During simulation, the discharged mass and energy were recorded to determine the composition and energy of both intake and exhaust backflow. That is, the discharged gas is first introduced into the cylinder as backflow until it is nearly exhausted. Further, the simulation was iterated until the trapped in-cylinder mass at IVC timing and the remaining mass of intake backflow in the intake manifold converge to one percent deviation of those in the previous cycle.

Figure 4.1 shows the temperature and residual mass determined by the aforesaid approach at the ignition timing plotted along with the experimental value of pressure. The temperature and pressure ranges at the ignition timing vary from 559–794 K and 4.5–28.6 bar respectively, indicating the broad thermodynamic range of the operating points explored in this study.

Furthermore, the combustion regime diagram is presented in Fig. 4.2. It is readily identified that the points of Engine D, in particular, exhibit higher velocity ratios due to the lowered planar laminar flame speed in lean conditions. Besides, as

depicted in Fig. 4.2(a), a vast majority of the points at ignition timing are located in the thin reaction zones regime. As the local turbulent intensity decreases when the flame propagates, and Zel'dovich flame thickness decreases with an increase in the in-cylinder pressure, the operating points typically portray the trajectories during combustion, as shown in Fig. 4.2(b). Therefore, it can be concluded that the points of Engine A-C are mainly located in the corrugated flamelets zone. Despite the transition during combustion, the points of Engine D are prone to locate in thin reaction zones regime.

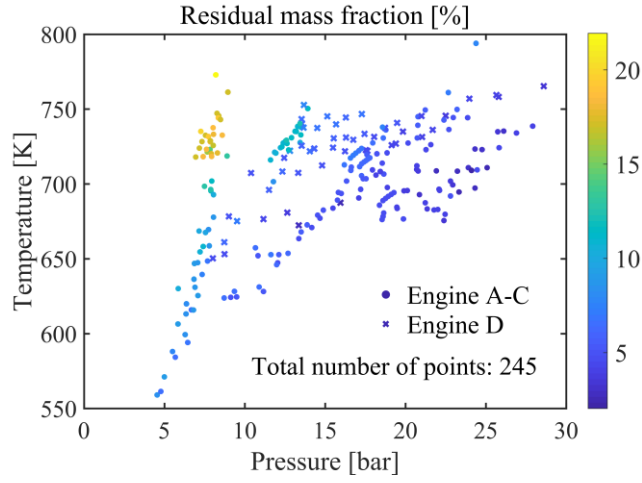


**Figure 4.1** Operating ranges of temperature, pressure, and residual mass fraction at ignition timing.

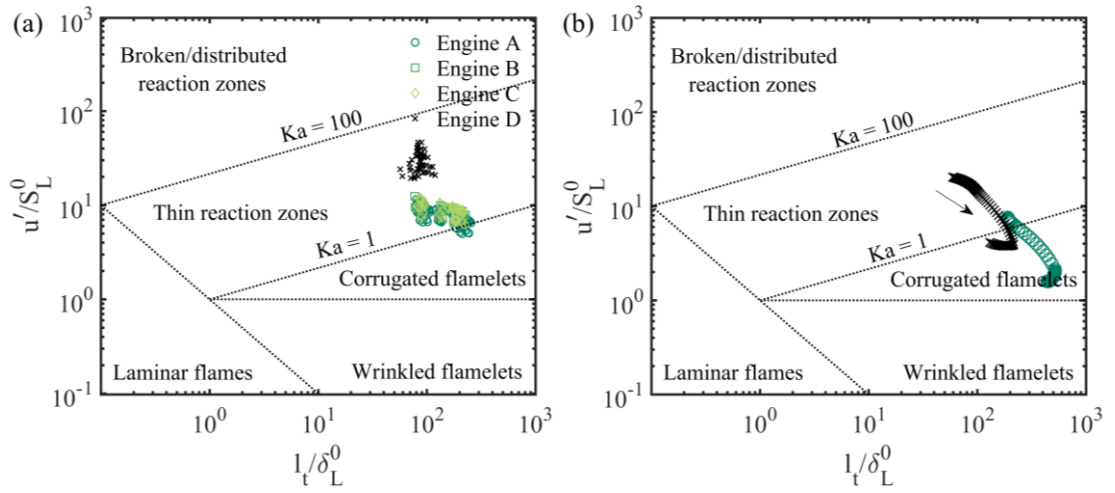


**Figure 4.2** Combustion regime diagram for a premixed turbulent flame. (a) Conditions of all operating points at ignition timing and (b) example cases (Engines A and D) for the trajectory of the condition during combustion.

## 4.2. Turbulence/flame interaction model

### 4.2.1. Flame surface density (FSD) model

The FSD model, which is based on the flame surface density balance equation, has been widely applied in numerical simulations such as 0D [23-26], RANS [36], and LES [37-39]. This model assesses the flame wrinkling process in unresolved volume (corresponding to the integral length scale and sub-grid scale in RANS and LES, respectively) by solving the filtered balance equation. The equation for evaluating the flame surface density  $\bar{\Sigma}$  representing the extent of wrinkled flame surface per unit volume is given as

$$\begin{aligned} \frac{\partial \bar{\Sigma}}{\partial t} + \nabla \cdot (\langle \hat{\mathbf{u}} \rangle_s \bar{\Sigma}) + \nabla \cdot (\langle U_d \hat{\mathbf{n}} \rangle_s \bar{\Sigma}) \\ = \langle \nabla \cdot \hat{\mathbf{u}} - \hat{\mathbf{n}} \hat{\mathbf{n}} : \nabla \hat{\mathbf{u}} \rangle_s \bar{\Sigma} + \langle U_d \nabla \cdot \hat{\mathbf{n}} \rangle_s \bar{\Sigma}, \end{aligned} \quad (4.14)$$

where  $\hat{\mathbf{u}}$ ,  $U_d$ , and  $\hat{\mathbf{n}}$  are the local velocity, displacement speed of the flame front, and the normal vector to the flame front, respectively. The bracket  $\langle \cdot \rangle_s$  denotes the average value along the flame surface. Particularly, the LHS of this transport equation comprises the unsteady term and two convection terms by local velocity and flame speed, in order. The RHS terms comprise the strain rate effect by the velocity field and the combined effect of curvature and flame propagation. Furthermore, to utilize this equation in the simulation, the closure on the production of the wrinkled flame surface by the strain rate (the first term in RHS) should be implemented first.

In the context of RANS, this production term is commonly related to the ratio of the turbulent intensity  $u'$  to the integral length scale  $l_t$  [37, 38]:

$$\langle \nabla \cdot \hat{\mathbf{u}} - \hat{\mathbf{n}}\hat{\mathbf{n}} : \nabla \hat{\mathbf{u}} \rangle_s = \Gamma \frac{u'}{l_t}. \quad (4.15)$$

The integrated straining efficiency  $\Gamma$  hence should be closed to utilize the equation.

For completeness, the determining methodology for  $\Gamma$  proposed by Charlette et al. [37] is briefly reviewed here. It is worth noting that using this methodology,  $\Gamma$  can be evaluated by considering the respective wrinkling abilities based on the different turbulent length scales.

For the first step of the evaluation, one might find the expression for the velocity-derivative (strain rate) information from the energy spectrum of homogeneous turbulence:

$$\langle \left( \frac{\partial u_1}{\partial x_1} \right)^2 \rangle = \int_0^\infty \kappa^2 E_{11}(\kappa) d\kappa, \quad (4.16)$$

where  $\kappa$  is the wavenumber of vortex size  $r$ , expressed as  $\kappa = \pi/r$ , and  $E_{11}(\kappa)$  is the one-dimensional energy spectrum. By inserting the efficiency function  $C(\kappa)$ , which indicates the flame stretch efficiency of the vortex having wavenumber  $\kappa$ , and  $\Gamma$  into Eq. (4.16), the equation is modified as

$$\left( \Gamma \frac{u'}{l_t} \right)^2 = \int_{\pi/l_t}^\infty [C(\kappa)]^2 \kappa^2 E_{11}(\kappa) d\kappa. \quad (4.17)$$

The function  $C(\kappa)$  is formed by the DNS study that instigated the vortex-flame interactions, and several forms of the function have been proposed in previous studies [37-39, 106]. In these studies, the value of  $C(\kappa)$  is determined at the

specified length and velocity ratios of their respective vortices:  $C\left(\frac{r}{\delta_L}, \frac{v}{S_L^0}\right)$ , where  $v$  is the speed of a vortex. By utilizing  $C\left(\frac{r}{\delta_L}, \frac{v}{S_L^0}\right)$ , the RHS in Eq. (4.17) could yield the net flame stretch from all the vortices having length scales below  $l_t$ . Lastly, if the Kolmogorov spectrum with viscous cutoff  $f_p$ , Pao spectrum, substitutes  $E_{11}(\kappa)$  and conducts normalization to attain non-dimensionless quantities,  $\Gamma$  eventually evolves as

$$\Gamma^2 = 0.49\pi^{\frac{4}{3}} \int_1^\infty C\left(\frac{r(\kappa)}{\delta_L}, \frac{v(\kappa)}{S_L^0}\right)^2 \bar{\kappa}^{\frac{1}{3}} f_p(\bar{\kappa}, \text{Re}_l) d\bar{\kappa}, \quad (4.18)$$

where

$$\begin{aligned} \bar{\kappa} &= \kappa \frac{l_t}{\pi}, & \frac{r(\kappa)}{\delta_L} &= \frac{1}{\bar{\kappa}} \frac{l_t}{\delta_L}, \\ \frac{v(\kappa)}{S_L^0} &= \frac{u'}{S_L^0} (\bar{\kappa}\pi)^{\frac{1}{3}} [0.49f_p(\bar{\kappa}, \text{Re}_l)]^{\frac{1}{2}}, \text{ and } \text{Re}_l &= \frac{4u'l_t}{S_L^0 \delta_L^0}. \end{aligned} \quad (4.19)$$

Therefore, the strain rate effect term in Eq. (4.14) can be expressed using  $\Gamma$  in Eq. (4.18), which was determined by the efficiency function,  $C\left(\frac{r}{\delta_L}, \frac{v}{S_L^0}\right)$ . The interested readers are referred to the cited paper [37] for further details.

However, for the 0D application, Eq. (4.14) should be additionally modified, following the approach by Richard and Veynante [26]. Firstly, by introducing wrinkled (unresolved) and unwrinkled (resolved) flame surfaces  $A_T$  and  $A_L$ , respectively, one can obtain the following equations:

$$A_T = \iiint \bar{\varepsilon} dV, \quad (4.20)$$

$$A_T = \varepsilon A_L, \quad \frac{1}{\varepsilon} \frac{d\varepsilon}{dt} = \frac{1}{A_T} \frac{dA_T}{dt} - \frac{1}{A_L} \frac{dA_L}{dt}, \quad (4.21)$$

where the wrinkling factor  $\varepsilon$  is defined as the ratio of  $A_T$  to  $A_L$ . By volume integrating Eq. (4.14) and utilizing the relation in Eq. (4.20), Eq. (4.14) is rewritten as

$$\frac{1}{A_T} \frac{dA_T}{dt} = \frac{\iiint (\langle \nabla \cdot \hat{\mathbf{u}} - \hat{\mathbf{n}} \hat{\mathbf{n}} : \nabla \hat{\mathbf{u}} \rangle_s \bar{\varepsilon} + \langle U_d \nabla \cdot \hat{\mathbf{n}} \rangle_s \bar{\varepsilon}) dV}{\iiint \bar{\varepsilon} dV}. \quad (4.22)$$

With several assumptions concerning the RHS terms, Eq. (4.22) can be expressed by using  $\Gamma$  as

$$\frac{1}{A_T} \frac{dA_T}{dt} = \Gamma \frac{u'}{l_t} \left( \frac{\varepsilon_{\text{eq}} - \varepsilon}{\varepsilon_{\text{eq}} - 1} \right) + \frac{2}{r_f} \sigma S_L - \frac{2}{3\gamma P} \frac{dP}{dt}, \quad (4.23)$$

where  $P$  and  $\gamma$  are the in-cylinder pressure and specific heat ratio, respectively, and  $\varepsilon_{\text{eq}}$  is the equilibrium value of  $\varepsilon$  at the fully-developed turbulent flame. Although  $\varepsilon_{\text{eq}}$  is commonly presented by the formula using  $\Gamma$  with the Kolmogorov-Petrovski-Piskunov theorem in the earlier 0D FSD models [23, 24, 26], a newly developed formula, which will be addressed further, was used in this study. Subsequently, through simple derivation procedures (see Eqs. (8)-(10) in [26]), the relation associated with  $A_L$  could be obtained:



$$\frac{1}{A_L} \frac{dA_L}{dt} = \frac{2}{r_f} \sigma \mathcal{E} S_L - \frac{2}{3\gamma P} \frac{dP}{dt}. \quad (4.24)$$

Finally, by substituting Eqs. (4.23)-(4.24) into Eq. (4.21), the FSD model equation applied in 0D simulation is derived as

$$\frac{1}{\mathcal{E}} \frac{d\mathcal{E}}{dt} = \Gamma \frac{u'}{l_t} \left( \frac{\mathcal{E}_{eq} - \mathcal{E}}{\mathcal{E}_{eq} - 1} \right) - \frac{2}{r_f} \sigma (\mathcal{E} - 1) S_L. \quad (4.25)$$

Particularly, the first term in the RHS denotes the net production of the wrinkled flame surface by the respective vortices, whose sizes lie between the inner and outer cutoff scales. As this term physically describes the transient wrinkling process with the integrated flame stretch abilities of vortices, the early flame development could thereby be reproduced in the model. Furthermore, provided the net flame stretch is sufficiently high, this term results in  $\mathcal{E}$  asymptotically approaching  $\mathcal{E}_{eq}$ , growing as a fully-developed turbulence flame. Conversely, the second term denotes the flame annihilation by flame propagation, which in turn behaves as the sink for the wrinkled flame surface.

#### 4.2.2. Efficiency function and cutoff scales

The efficiency function  $C\left(\frac{r}{\delta_L}, \frac{v}{s_L^0}\right)$  refers to the flame stretch efficiencies of the respective vortex whose size and velocity are  $r$  and  $v$ , respectively. As addressed earlier, this function is a key ingredient for determining the net straining efficiency  $\Gamma$ , which reproduces the transient wrinkling process. Therefore, selecting an appropriate efficiency function can significantly influence the performance of the

model. Prior to the selection of the efficiency function, several forms of functions proposed in previous studies will be briefly introduced here.

The efficiency function was firstly proposed by Meneveau and Poinso [39], which is the only function of length ratio, i.e.,  $C\left(\frac{r}{\delta_L}\right)$ . Since velocity influences the stretch efficiency, a new function was later devised by Colin et al. [38] to include the effect of velocity ratio as  $C\left(\frac{r}{\delta_L}, \frac{v}{s_L^0}\right)$ . Subsequently, Charlette et al. [37] modified Colin's function and included an additional inner cutoff whose characteristic velocity was half the planar laminar flame speed, which is associated with the Gibson scale. Recently, Bourgrine et al. [106] reduced kinetics in the DNS scheme and developed an efficiency function reflecting the fuel characteristics. This reflection of mixture composition is of vital importance for the generality of the model, considering the thermo-diffusive instability at the reactant with non-unity Lewis number can influence the flame wrinkling process.

Figure 4.3 shows all aforesaid efficiency functions at different length and velocity ratios. As expected, the efficiency function in [39] remained unchanged for different velocity ratios due to the absence of the velocity ratio as a variable. Conversely, while the function in [38] increases its efficiency slightly at the higher velocity scale, a noticeable increment was observed at the function in [37] owing to the activation of the additional inner cutoff scale at the lower velocity ratio. However, since the only difference of the function between [37] and [38] is the cutoff scale, they nearly overlap at the higher velocity scale where the cutoff is ineffective, whereas the function in [106] has two distinctive features. First, the efficiency is higher than the unity for conditions with lower velocity ratios and higher length ratios. Second, it exhibits low efficiency at higher velocity ratios, which is the opposite behavior of other functions.

It is worth stressing that the experimental data in this study has a wider range of velocity ratio compared to the general engine data, considering the planar laminar flame speed at lean-burn points (operating points from Engine D in Table 4.1) are 2–3 times slower than that at the stoichiometric points. That is, the behaviors of the functions concerning the velocity ratio are crucial for the performance of the model. Owing to this, the function in [106] was successfully embedded in the experimental data with a few validation constants.

Furthermore, it is worth focusing on the common feature of the efficiency functions at the lower length ratios. Specifically, their efficiencies weaken when the vortex size approaches the length of laminar flame thickness. This feature evidently plays as an inner cutoff that nullifies the wrinkling of vortices smaller than the laminar flame thickness. Besides, a similar concept of an inner cutoff scale was substantiated by several precedent studies.

For instance, in a series of experimental works conducted by Kobayashi and co-workers [61, 70], the inner cutoff was proved to be saturated to the characteristic scale of flame instability at a sufficiently high Reynolds number. The point is that this characteristic scale is typically relevant to the length of Zel'dovich flame thickness, albeit not a strict comparison. Moreover, based on a DNS study conducted by Yu and Lipatnikov [63], the existence of the local curvatures at the reaction zone was found to retain similarities when normalized by the Zel'dovich flame thickness at various turbulence conditions. They further argued that the flame wrinkling by the vortices smaller than the Zel'dovich flame thickness was readily smoothed out by the molecular transport effect, thereby presenting flame thickness as the inner cutoff. More recently, Ahmed et al. [60] showed that the inner cutoff scale was in the order of Zel'dovich flame thickness by numerical analysis.

In contrast, several studies have proposed the inner cutoff scale being proportional to the Kolmogorov length scale at the unburned gas,  $\eta$ . Gülder and Smallwood [71] suggested the regression line of inner cutoff as  $22\eta$  based on the collected experimental data from the literature. Kobayashi et al. [70] claimed that the inner cutoff was approximately  $12\eta$  when its value is larger than the characteristic scale of flame instability at a low Reynolds number. Furthermore, Shim et al. [33] suggested a fitting function for the inner cutoff with gathered previous numerical and experimental data. The function therein asymptotically approached  $8\eta$  when the Zel'dovich flame thickness became narrower compared to  $\eta$ , but diverged otherwise.

Although no explicit consensus was found in previous studies, the common statement concerning the shift of inner cutoff could be elicited. As mentioned earlier, Kobayashi et al. [70] assessed the inner cutoff by comparing the characteristic scale of flame instability and  $\eta$  for various Reynolds numbers, and a clear transition was observed between the two properties at a moderate Reynolds number. Moreover, although Ahmed et al. [60] claimed that the inner cutoff scale was relevant to flame thickness, higher values of inner cutoff relative to Zel'dovich flame thickness were observed at the weak turbulence condition, where  $\eta$  was elevated, which could be interpreted as the transition. A similar transition was also recognized from the fitting function proposed by Shim et al. [33] at values where  $\eta$  and the Zel'dovich flame thickness became comparable. Considering these aspects, the inner cutoff  $\varepsilon_c$  was evaluated by selecting the maximum value between  $\delta_L$  and  $8\eta$ :

$$\varepsilon_c = \max(\delta_L, 8\eta). \quad (4.26)$$

Note that further discussion on the transition of inner cutoff during combustion is presented in Appendix. C. Since  $\delta_L$  plays as an inner cutoff scale in the efficiency functions, it is accordingly replaced by  $\varepsilon_c$ ; i.e.,  $C\left(\frac{r}{\varepsilon_c}, \frac{v}{S_L^0}\right)$ . As a result, the function by Bourgrine et al. [106] is recast as

$$C\left(\frac{r}{\varepsilon_c}, \frac{v}{S_L^0}\right) = C_{\text{eff}} \left[ \frac{C_r}{1 + 0.3 \left(\frac{v}{S_L^0}\right) C_r} \right] \cdot \left[ \frac{1.76 + \tanh(\text{Le} - 2)}{\text{Le}} \right], \quad (4.27)$$

where

$$C_r\left(\frac{r}{\varepsilon_c}\right) = 1 + \text{erf}\left[0.9 \log\left(C_{\text{in}} \frac{r}{\varepsilon_c}\right) - 2\right]. \quad (4.28)$$

Here,  $C_{\text{eff}}$  and  $C_{\text{in}}$  are the validation constants. In particular,  $C_{\text{eff}}$  and  $C_{\text{in}}$  are used to adjust the overall quantity of efficiencies and the effect of inner cutoff, respectively.

In addition to the inner cutoff, the present model makes use of an outer cutoff scale to adjust the wrinkling process. In a physical sense, the early flame kernel with a sufficiently small radius is unable to facilitate the stretching by large-scale turbulence. This is consistent with the explanation presented by Abdel-Gayed et al. [107], which states that the initial flame is convected by the lower frequencies of turbulence without affecting the flame front. Similarly, Richard and Veynante [26] used the outer cutoff by considering the time scale of flame development  $\tau_l$  in their 0D FSD model. The time scale  $\tau_l$  is defined as the ratio of flame radius  $r_f$  to the laminar flame speed at the burned gas  $\sigma S_L$ . Then, they made the vortices having eddy turnover times longer than  $\tau_l$  being ineffective for flame wrinkling.

Instead of the timescale-based approach, in this study, the outer cutoff scale is set to be proportional to the radius of the flame kernel. That is, the vortices larger than the designated radius which is proportional to the radius of the flame kernel become ineffective for flame wrinkling. To utilize this concept, the stretch efficiency in Eq. (4.18) was integrated over the wavelengths larger than that of the vortex whose size is prescribed as  $C_{\text{out}}r_f$ , given as

$$\Gamma^2 = 0.49\pi^{\frac{4}{3}} \int_{\max(\frac{l_t}{C_{\text{out}}r_f}, 1)}^{\infty} C \left( \frac{r(\kappa)}{\varepsilon_c}, \frac{v(\kappa)}{S_L^0} \right)^2 \bar{\kappa}^{\frac{1}{3}} f_p(\bar{\kappa}, \text{Re}_l) d\bar{\kappa}. \quad (4.29)$$

Note that, provided the outer cutoff scale is larger than the integral length scale, one can recover the original equation from Eq. (4.29). Although this approach necessitates additional validation constant  $C_{\text{out}}$ , it poses a distinct physical implication from the previous approach [26].

Using three validation constants ( $C_{\text{eff}}$ ,  $C_{\text{in}}$ , and  $C_{\text{out}}$ ), the prediction of burn duration from 0–10%, hereinafter BD0010, was satisfactorily achieved as shown in Fig. 4.4. The values of  $C_{\text{eff}}$ ,  $C_{\text{in}}$ , and  $C_{\text{out}}$  were set as 0.35, 3, and 0.06, respectively. This result is noteworthy as every point in this study agrees with the model without showing any significant deviation. That indicates the physics of transient turbulence/flame interaction was successfully reproduced by the model. Note that the validation of BD0010 was primarily achieved by adjusting the three constants, as all factors other than  $\Gamma$  have marginal influences on BD0010.

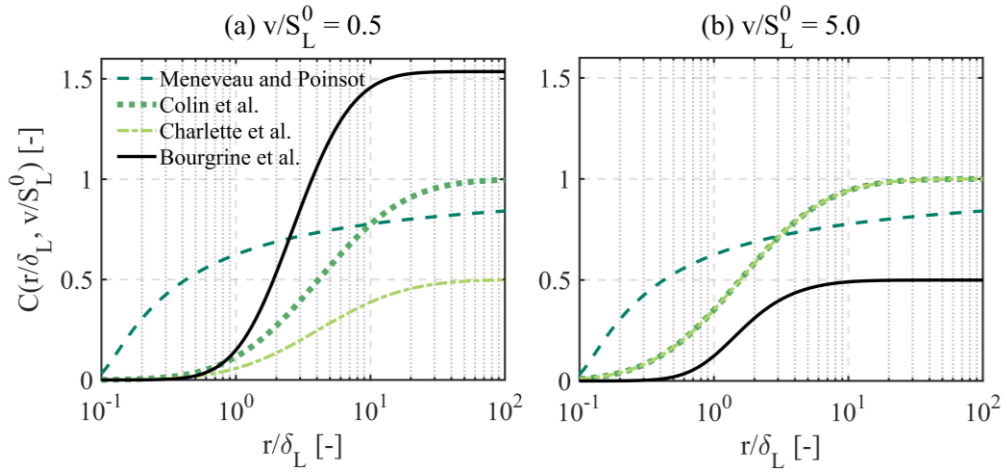


**Figure 4.3** Efficiency functions in previous studies at different length ratios ( $r/\delta_L$ ) and velocity ratios ( $v/S_L^0$ ). (a):  $v/S_L^0 = 0.5$ , (b):  $v/S_L^0 = 5.0$ .

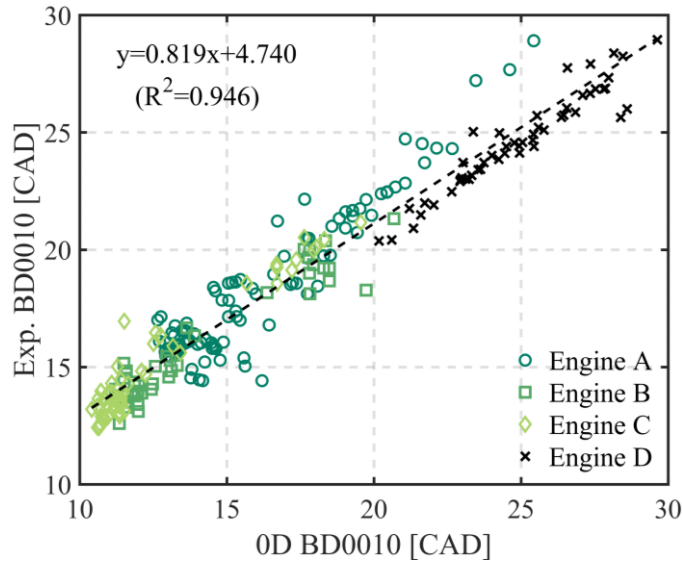


**Figure 4.4** Comparison of BD0010 with a total of 245 points for four different engines. The abscissa and ordinate indicate BD0010 obtained from the 0D simulation and experiment, respectively.

### 4.2.3. Distribution of turbulence

The obvious shortcoming of the 0D simulation arises from the deficiency of local information. This is particularly pronounced when predicting the local turbulence unevenly distributed throughout the cylinder. To overcome this, a methodology to estimate the local turbulence is suggested here based on several assumptions. It should be noted that the discussion in this section focuses on the engine utilizing tumble as the only flow structure.

First, the distribution structure of in-cylinder turbulence should be investigated. As the structure can be readily identified by analyzing 3D CFD, the motoring result of case 1 from Chapter 3, the reference case, was exploited for the analysis. In terms of the numerical scheme, the identical configuration in Chapter 3 is utilized for the simulation. As shown in Fig. 4.5, the turbulence is primarily located on the tumble center, which is nearly identical to the geometric center, and decreases linearly along the x-direction. Note that the x-y plane in the figure is the tumble plane, which indicates that the rotating axis of tumble is parallel to the z-axis. Additionally, a similar tendency was observed at the z-direction, which supports the centrally concentrated turbulence.

Moreover, an analogous phenomenon was observed experimentally by Zentgraf et al. [48]. Therein, a large portion of turbulence was found to be located near the tumble center by using particle image velocimetry as an optical measurement. It is worth noting that despite using the ensemble-averaged results, their finding excluded the effect of flow variance induced by the cycle-to-cycle variance. Besides, as the tumble center was found to exist at the geometric center near TDC experimentally [49] and numerically in Section 2.3.3, it is deemed reasonable to assume that the turbulence is centrally concentrated in the cylinder. Therefore, the distribution of



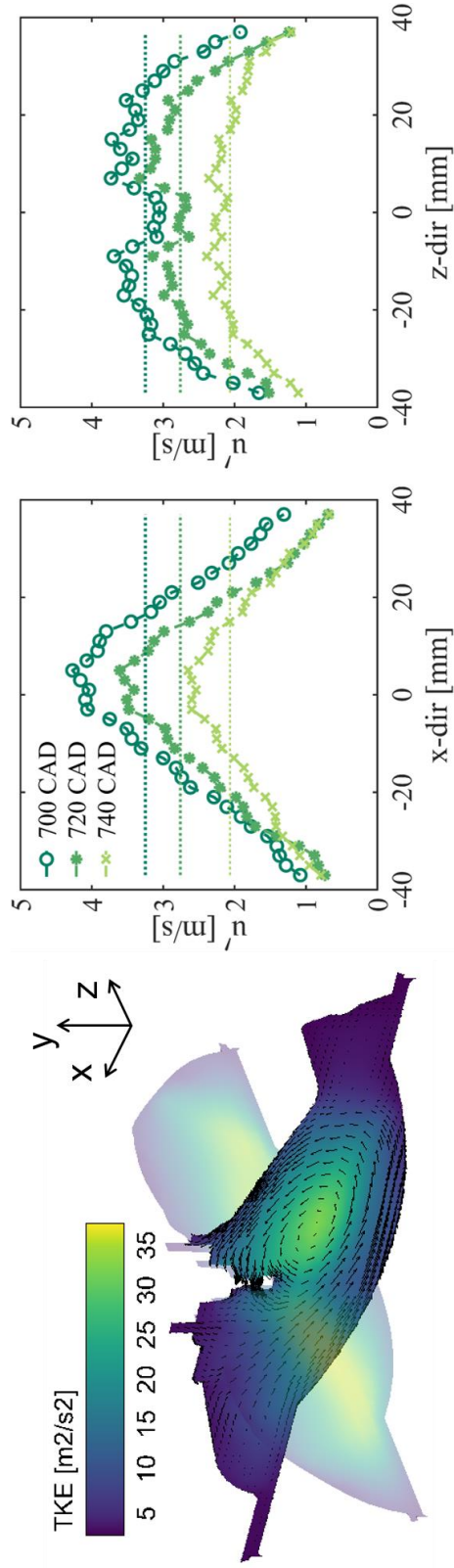


**Figure 4.5** The distribution of in-cylinder turbulence at the reference case. The leftmost figure shows the distributions of turbulent kinetic energy cut through the x-y and y-z planes at firing TDC. The markers and dotted lines in the middle and rightmost figures indicate the average turbulent intensities at the plane perpendicular to the respective directions and  $u'_{avg}$ , respectively.

turbulence in the present simulation was configured such that the turbulent intensity exhibited a linear profile along the radial direction with a maximum value at the center while retaining unchanged values along the direction of height.

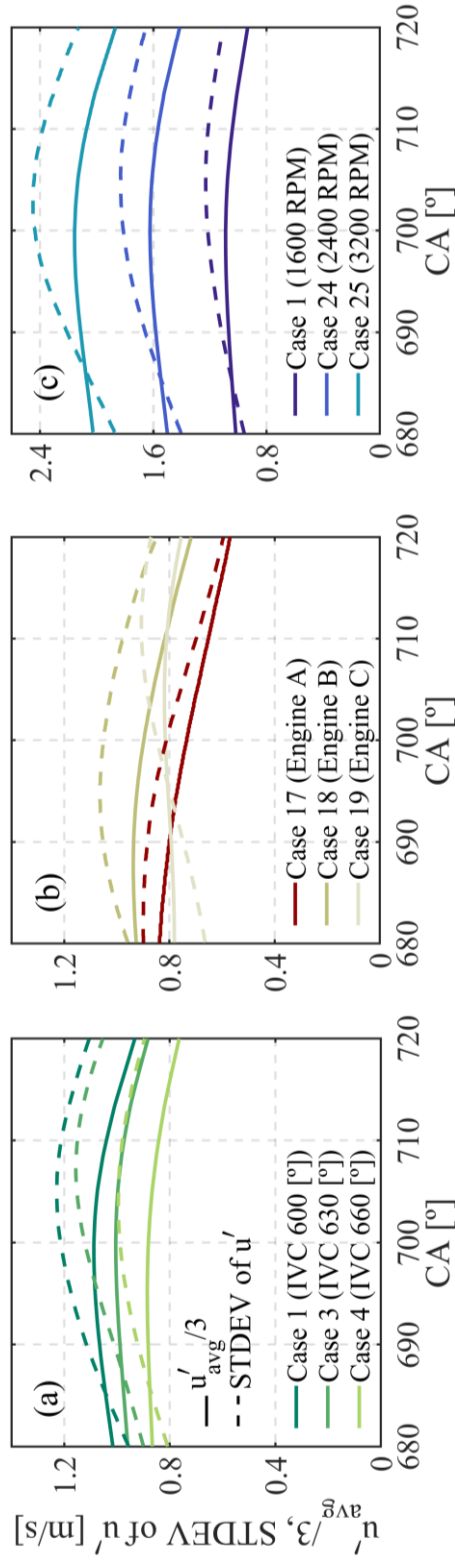
Further, an additional clue was used to determine the exact profile. The idea for solving this issue is attributed to the fact that the exact profile can be achieved using the two given properties: cylinder-averaged turbulent intensity  $u'_{\text{avg}}$  and standard deviation of the profile. Therefore, the focus was placed on the standard deviations of turbulent intensity obtained from 3D CFD. (Note that all averaged values employed in the analysis were averaged by volume.)

Figure 4.6 describes the standard deviations of turbulent intensity along with one-third of  $u'_{\text{avg}}$ . To secure the generality, a total of eight cases from Chapter 3 were considered for the analysis. At a glance, the analogies between both, the standard deviations and  $u'_{\text{avg}}$  were found in all cases at the shown crank angles, hereby indicating a similarity in the distribution structure of turbulence at diverse engine conditions. As such, the standard deviation was approximated as one-third of  $u'_{\text{avg}}$  in this study. Then, the exact profile of turbulent intensity could be specified with one property,  $u'_{\text{avg}}$ .

The profile of turbulent intensity is accordingly given as

$$u'(r) = u'_{\text{avg}} \left( 1 + \frac{2\sqrt{2}}{3} - \frac{2\sqrt{2}r}{B} \right), \quad (4.30)$$

where  $r$  is the radial distance from the geometric center of the cylinder and  $B$  is the bore of the cylinder. Further, by applying an additional assumption that the flamelet consecutively interacts with the strongest turbulence at the unburned zone,



**Figure 4.6** The standard deviations (dashed line) of turbulent intensity and volume-averaged turbulent intensities (solid line) at various engine operating cases. (a) Different IVC timings, (b) engine geometries, and (c) engine speeds. The numbering of cases is listed in Table 3.1.

the turbulent intensity in contact with the flamelet at a given burned gas volume could be evaluated. In other words, the burned gas volume was assumed as a cylindrical shape instead of a truncated sphere exclusively when estimating the turbulence in contact with the flamelet. This was achieved by simply replacing  $2r/B$  in Eq. (4.30) with the ratio of the burned gas volume to the total cylinder volume.

However, if further considering the dilatation of burned gas, which results in the compression of unburned gas, the mass fraction burned  $X_b$  is more pertinent to the substitution of  $2r/B$  compared to the volume ratio; that is, the substitution by  $X_b$  allows the equation to include the effect of the convection of turbulence induced by the compression. Therefore, Eq. (4.30) is rewritten as

$$u'(X_b) = u'_{\text{avg}} \left( 1 + \frac{2\sqrt{2}}{3} - \sqrt{2}X_b \right). \quad (4.31)$$

In order to verify the validity of Eq. (4.31), additional 3D CFD was implemented with the combustion model. As for the combustion model, the SAGE detailed kinetics solver [108] was utilized. The reference case was chosen as the subject of the analysis, and ignition timing was set as 715 CAD (=bTDC 5°). The objective of the simulation is to verify the effect of the combustion-induced dilation on the distribution of turbulence. Hence, the averaged turbulent intensity subjected to the volume of flame thickness was calculated during combustion. Note that the flame thickness was evaluated using the progress variable  $c$ , defined by temperature, and determined to be within the range of  $0.3 < c < 0.8$ , where  $c=0$  and 1 at the unburned and burned zone temperatures, respectively.

Figure 4.7 summarizes the results of the simulation. To further explicate the terms used in the figure,  $u'_{\text{flame}}$  is the averaged turbulent intensity within the flame thickness and  $u'_{\text{avg}}$  is the volume-averaged turbulent intensity obtained during motoring simulation, i.e., without combustion. The mass fraction burned  $X_b$  was calculated based on the heat release rate during combustion. Lastly,  $u'$  was determined using Eq. (4.31) and the prescribed values of  $u'_{\text{avg}}$  and  $X_b$ . Although discrepancy existed at the early flame development period,  $u'$  follows  $u'_{\text{flame}}$  more closely than  $u'_{\text{avg}}$ , confirming the validity of the equation.

This approach is intriguing given that the turbulent intensity was not considered as a discrete quantity at unburned and burned zones, which is different from the typical two-zone model. Instead, the turbulent intensity was determined identically with motoring simulation and redistributed considering the convection induced by combustion. As such, the local strength of the turbulent intensity in contact with flamelet could be directly evaluated. However, it is worth noting that this approach essentially presumes negligible effect of combustion on the strength of turbulence and purely highlights the effect of combustion on the convection of turbulence.

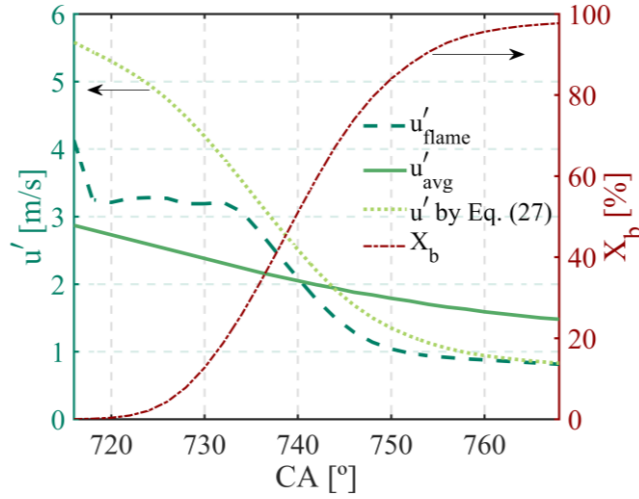


**Figure 4.7** Turbulent intensities and mass fraction burned. Detailed explanations regarding the terms are presented in the main body of the paper.

### 4.3. Determination of turbulent flame speed

In this section, the characteristics of the premixed flame subjected to turbulence are discussed and modeled using a variety of experimental and numerical analyses in the literature. First, the modeling process for the strained laminar flame speed, the average flamelet speed at turbulence-induced curvatures, is introduced. The flamelet characteristics at the thin reaction zones are further considered in the model since the experimental data by the lean-burn points exhibit, in particular, high Karlovitz numbers  $Ka$ , defined as the ratio of the chemical time scale to the Kolmogorov time scale, above unity. Subsequently, as an initial step for the determination of  $\mathcal{E}_{eq}$  in Eq. (4.25), the fully-developed turbulent flame speed equations proposed in previous studies are briefly reviewed. After the evaluation of the existing correlations, an expression for  $\mathcal{E}_{eq}$  applicable to the experimental data from this study is suggested as a consequence.

### 4.3.1. Strained laminar flame speed

Considering the wrinkled flame surface comprises numerous curvatures, the flamelet speed varies significantly along the flame surface due to differential diffusion. Therefore, the average flamelet speed or strained laminar flame speed is unequal to the planar laminar flame speed  $S_L^0$ . To date, numerous studies have observed and analyzed this phenomenon.

Weiβ et al. [62] conducted an experimental study wherein six mixtures with a Markstein numbers  $Ma$  between -2.8–5.7 were examined. Their results showed that the reactants with positive  $Ma$  exhibited lower strained laminar flame speed than  $S_L^0$ , whereas the fuels with negative  $Ma$  exhibited a higher strained laminar flame speed. Furthermore, Daniele et al. [30] conducted an experimental study and observed identical behaviors by varying the fuel composition of syngas and methane.

Similarly, some studies directly incorporated the differential diffusion effect in their closure forms of fully-developed turbulent flame speed by including Markstein length [64] or Lewis number [29, 109] for various reactant compositions. This study, however, conducts independent modeling of wrinkled flame surface and strained laminar flame speed. That is, the modeling for the closure of turbulent flame speed in Section 4.3.2 only presents the effect of increased flame surface and excludes the differential diffusion effect.

It should be further noted that the wrinkled flame surface in the fully-developed state is postulated to be unaffected by the thermo-diffusive instability, which is consistent with the findings of the DNS study conducted by Savard and Blanquart [83]. On comparing the probability density functions of mean curvature at the reaction zone with unity and non-unity  $Le$  reactants, they observed no differential

diffusion effect on the geometry of the reaction zone surface. It was revealed that both probability density functions from unity and non-unity Le reactants were almost identical, despite the different thermo-diffusive characteristics. In this regard, the effect of thermo-diffusive instability was only included in the efficiency function in Eq. (4.27), determining the speed of the wrinkling process.

For the base model, the equation of strained laminar flame speed  $\bar{S}_L$  suggested by Weiß et al. [62] was employed, given as

$$\frac{\bar{S}_L}{S_L^0} = 1 - \frac{I \cdot Ma \cdot Ka_{lam}}{\sigma} - I \cdot Ma \cdot Ka_{turb}, \quad (4.32)$$

where  $I_{eff}$  is an efficiency parameter only applicable for positive  $Ma$ :

$$I_{eff} = 1.241 \cdot [\max(\sqrt{\pi Ma \cdot Ka_{turb}}, 1)]^{-1.832}. \quad (4.33)$$

This efficiency parameter decreases the decline in flame speed to a certain extent at an adequately high  $Ka_{turb}$  and eventually portrays the saturation of the differential diffusion effect by turbulence-induced curvature during intense turbulence. Furthermore, similar behavior of the saturation of turbulence-induced curvature was observed in the numerical study conducted by Fogla et al. [65] (refer to Fig. 9 in the cited paper).

The definitions for the Karlovitz stretch factors  $Ka_{lam}$  and  $Ka_{turb}$  were consistent with [62], and are given as



$$\text{Ka}_{\text{lam}} = \kappa_s \frac{\delta_L^0}{S_L^0}, \quad \text{Ka}_{\text{turb}} = \frac{u'}{\lambda} \cdot \frac{\delta_L^0}{S_L^0} = \frac{1}{4} \left( \frac{u'^3}{\nu l_t} \right)^{\frac{1}{2}} \frac{\delta_L^0}{S_L^0}, \quad (4.34)$$

where  $\lambda$  and  $\nu$  are the Taylor microscale and kinematic viscosity at the unburned gas, respectively.

The second term in the RHS of Eq. (4.32) indicates the stretch effect by spherically expanding laminar flame proposed in Eq. (4.13). Accordingly, if the first and second terms are replaced with Eq. (4.13), the equation becomes

$$\bar{S}_L = S_L - I_{\text{eff}} \cdot \text{Ma} \cdot \text{Ka}_{\text{turb}} \cdot S_L^0. \quad (4.35)$$

Note that the analogous forms of strained laminar flame speed have been reported in the literature. Lin et al. [29] and Daniele et al. [30] utilized an identical formula with Eq. (4.35) for syngas and methane while excluding the efficiency parameter. Furthermore, Fogla et al. [65] introduced the formula with the average stretch rate determined numerically in place of  $\text{Ka}_{\text{turb}}$ .

However, Eq. (4.35) has a limitation for predicting the strained laminar flame speed since it describes the extent of flame wrinkling solely by the turbulent intensity  $u'$  in  $\text{Ka}_{\text{turb}}$ , implying that it could fail to predict the flame speed when the flame is not sufficiently wrinkled at the intense turbulence, particularly at the early flame development period. Besides, Eq. (4.32) was originally developed based on the experimental data obtained when the flame radius reaches 3.5 cm at a spherically expanding flame [62]. Considering this, an additional factor representing the extent of the flame development was placed in Eq. (4.35). This modification postulates the experimental data in [62] was obtained at a fully-developed flame, recovering the

original equation when the wrinkling factor becomes the equilibrium value. The equation is thus recast as

$$\bar{S}_L = S_L - I_{\text{eff}} \cdot \text{Ma} \cdot \text{Ka}_{\text{turb}} \cdot \left( \frac{\mathcal{E} - 1}{\mathcal{E}_{\text{eq}} - 1} \right) \cdot S_L^0. \quad (4.36)$$

As seen in Fig. 4.2, a particularly high  $\text{Ka}$  is shown for the lean-burn points owing to their lower  $S_L^0$  and higher  $\delta_L^0$  compared to the stoichiometric cases. Accordingly, the flame characteristics in the thin reaction zones have been considered.

The popular notion associated with the thin reaction zones was firstly proposed by Damköhler [28], who argued that small-scale turbulence affects molecular transport within the flame thickness, and suggested that the turbulent flame speed is proportional to the square root of the turbulent molecular diffusivity. Similarly, numerous studies have discussed the effects of modified molecular transport in the thin reaction zones on flame characteristics.

In a series of DNS studies conducted by Savard and co-workers [82-84], the differential diffusion effect decreased as turbulence increased due to the enhanced transport phenomena. In their analyses, both non-unity and unity  $\text{Le}$  cases for each fuel (i.e., hydrogen [82] and n-heptane [83, 84]) were simulated by modifying the transport properties in the numerical scheme. Furthermore, the flame structures at non-unity  $\text{Le}$  were revealed to approach the structures determined at unity  $\text{Le}$  as turbulence increased. This finding supports the increase of both thermal and mass diffusivity owing to turbulence at the thin reaction regime.

Meanwhile, several studies have experimentally and numerically substantiated the broadened preheat zone and reaction zone thicknesses at high  $Ka$  conditions [77, 79, 80, 110]. Wang et al. [80] observed the non-proportional relation between the wrinkled flame surface and turbulent flame speed and pinpointed the rationale behind the increase in turbulent flame speed at high  $Ka$  as the broadened flame thickness. That is, contrary to the flamelets regimes, the turbulent flame speed is no longer proportional to the increased flame surface but is additionally relevant to the increase in the reaction zone thickness by enhanced diffusivity.

To reproduce the flame behaviors at the thin reaction zones, the models proposed by Lapointe et al. [110] were employed in this simulation. As for the differential diffusion effect, the individual Lewis number  $Le_i$  in Eq. (4.1) was modified and re-evaluated to determine the effective Lewis number  $Le_{eff}$  in Eq. (4.3). The equation for the modified individual  $Le_{i,mod}$  is determined as

$$Le_{i,mod} = \frac{1 + a_1 Ka_r}{1/Le_i + a_1 Ka_r}, \quad (4.37)$$

where  $Ka_r$  is the reaction zone Karlovitz number, defined as

$$Ka_r = \left( \frac{\delta_r}{\eta_r} \right)^2. \quad (4.38)$$

Here,  $\delta_r$  and  $\eta_r$  are the reaction zone thickness and the Kolmogorov length scale at the reaction zone, respectively. As Lapointe and Blanquart [111] pointed out that  $\delta_r$  is in the range of one-third to one-half of the laminar flame thickness  $\delta_L$  according to their data, the value of  $\delta_r$  in this simulation was assumed to be half of  $\delta_L$ . Furthermore,  $\eta_r$  is determined as the Kolmogorov length scale at burned gas.

Coefficient  $a_1$  was set as 0.01, which is consistent with the literature [110]. At high  $Ka_r$  conditions,  $Le_{eff}$  closer to unity than its unperturbed value could be attained, which weakened the thermo-diffusive effect.

In the aspect of the broadened flame thickness, the reaction rate was assumed to be proportional to the width of the flame thickness. As such, the broadened ratio relative to its laminar value ( $\sim\sqrt{1 + a_2 Ka_r}$ ) was directly multiplied by  $\bar{S}_L$  to evaluate the modified strained laminar flame speed  $\bar{S}_{L,mod}$ , resulting in

$$\bar{S}_{L,mod} = \sqrt{1 + a_2 Ka_r} \cdot \bar{S}_L. \quad (4.39)$$

As suggested in the literature [110], the coefficient  $a_2$  was set as 0.01. Therefore, by utilizing Eqs. (4.37)-(4.39), the flame characteristics at thin and distributed reaction zones regimes were eventually adopted in the simulation.

In order to assess the impact of flamelet speed effects on the experimental data used in this study, the simulation results of two operating points from Engine A ( $\phi = 1$ ) and Engine D ( $\phi < 1$ ) are compared in Fig. 4.8. The period between ignition timing and crank angle at 95% of mass fraction burned is presented in the figure. The objective of the analysis was to understand the propensities of the strained laminar flame speed that were different from those of the planar laminar flame speed. However, it should be borne in mind that the cases shown in the figure are not representative of the entire engine cases.

To discretely analyze the influences associated with combustion regimes, the characteristics at the thin reaction zones were not accounted for in determining  $\bar{S}_L$ . That is, the effects of weakened differential diffusion and broadened flame thickness

by high  $Ka_r$  were exclusively included in  $\bar{S}_{L,mod}$ . At a glance, the flame speed reductions owing to the differential diffusion without enhanced diffusivity effect (i.e., the difference between  $S_L^0$  and  $\bar{S}_L$ ) were observed to be considerable in the figure, with the peak reduction accounting for over 25% of  $S_L^0$  in both cases. In contrast, the effects of  $Ka_r$  deemed to be negligible in the stoichiometric point, whose  $Ka_r$  was an order of magnitude less than that of the lean-burn point. Furthermore, despite the relatively high  $Ka_r$  condition at the lean-burn point, only a partial increase was observed in the flame speed by those effects at the early flame development. This result is consistent with the explanation provided by Lapointe et al. [110], which states that the reaction zone thickness is comparable to that of the laminar flame in most reactions even at high Karlovitz number ( $Ka_r \sim 100$ ), thereby indicating a negligible effect of broadened reaction zone thickness in the lean-gasoline engine points.

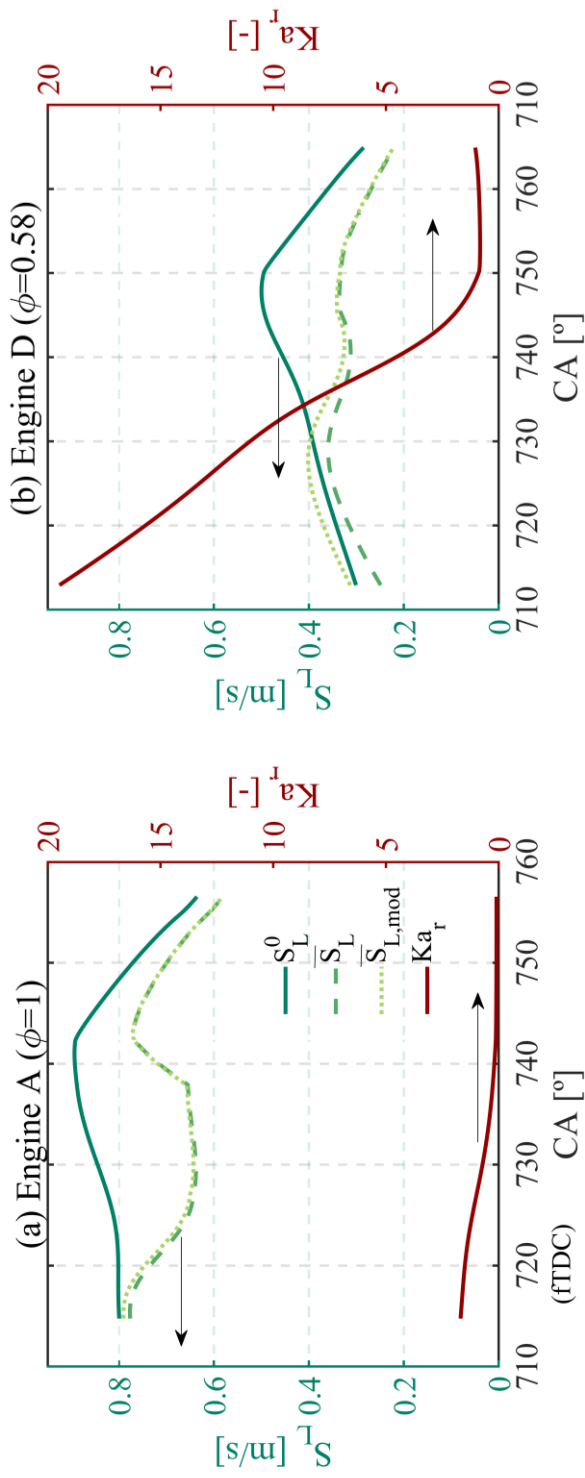


**Figure 4.8** 0D simulation results for the laminar flame speeds ( $S_L^0$ ,  $\bar{S}_L$ , and  $\bar{S}_{L,mod}$ ) at the left ordinates and the reaction zone Karlovitz number ( $Ka_r$ ) at the right ordinates. (a) One instance for the stoichiometric point with Engine A, and (b) one instance for the lean-burn point with Engine D.

### 4.3.2. Closure of the fully-developed turbulent flame speed

As a majority of combustion is undergone with turbulent flame, predicting the turbulent flame speed has been an intriguing but challenging issue in the combustion society. Until recently, extensive research has been conducted for the closure of turbulent flame speed [29, 59, 61, 63-69, 111]. Given that turbulent flame speed  $S_T$  is physically interpreted as the product of wrinkled flame surface and flamelet speed, it is commonly normalized using the laminar flame speed to express the extent of the wrinkled flame surface; e.g.,  $\Xi = S_T/S_L^0$ . That is, the existing closure forms are conducive clues to reveal the factors influencing flame wrinkling, and eventually to determine the wrinkling factor for the fully-developed turbulent flame,  $\Xi_{eq}$ . In that respect, several existing forms of turbulent flame speed are introduced here, and the possible factors that influence flame wrinkling are discussed. Note that the simulations performed in this section include all previous models except for the wall quenching model that is proposed later in this study.

The closure forms of turbulent flame speed have been diversely developed and proposed numerically [63, 65, 111] and experimentally [29, 59, 61, 64, 66-69] in the literature. As for the experiment, two methods have been mostly used to measure turbulent flame speed: fan-stirred centrally-ignited burners [61, 64, 66-70] and Bunsen-type burners [29, 59, 61, 70]. Table 4.2 summarizes the closure forms from experimental studies and the explored ranges of combustion environments.

Despite the different apparatuses used in the experiment, the common features in the expressions can be easily identified in Table 4.2. Undoubtedly, the effect of turbulence is included in velocity ratio,  $u'/S_L^0$ , with the exponent less than unity. It thus indicates the bending effect, which portrays the curved profile of turbulent flame speed as the turbulent intensity increases. Additionally, the effects of pressure and

flame thickness are identified in the expressions. Considering the Zel'dovich flame thickness is strongly correlated to pressure, as  $\delta_L^0 \sim P^{-c}$ , where the exponent  $c$  is positive, both effects are presumed to be one phenomenon and hereinafter denoted as the “pressure effect.”

**Table 4.2** Closure forms of turbulent flame speed from experimental studies.

$P^0$  and  $T^0$  denote the reference values for pressure and unburned zone temperature, respectively. Exact values are referred to in the literature.

No.	Expression	$T_u$ [K]	P [bar]	Fuels	Ref.
1	$\frac{S_T}{S_L^0} \sim \left(\frac{u'}{S_L^0}\right)^{0.38} \left(\frac{P}{P^0}\right)^{0.38}$	300, 573	~10	Methane	[61]
2	$\frac{S_T}{S_L^0} \sim \left(\frac{u'}{S_L^0}\right)^{0.63} \left(\frac{P}{P^0}\right)^{0.63} \left(\frac{T}{T^0}\right)^{-0.63} \left(\frac{l_t}{\delta_L^0}\right)^{-0.37}$	~773	~20	Syngas, methane	[59]
3	$\frac{S_T}{S_L^0} \sim \left(\frac{u'}{S_L^0}\right)^{0.53} \left(\frac{l_t}{\delta_L^0}\right)^{0.47}$	N/A	~12	Methane	[69]
4	$\frac{S_T}{S_L^0} \sim A \left(\frac{u'}{S_L^0}\right) \left[\left(\frac{u'}{S_L^0}\right)^2 \left(\frac{u' l_t}{\nu}\right)^{-0.5}\right]^B$ where $A, B = f(\text{Ma})$	~480	~35	Six species	[66]
5	$\frac{S_T}{S_L^0} \sim \left(\frac{u'}{S_L^0}\right)^{0.5} \left(\frac{r_f}{L_b}\right)^{0.5}$	N/A	~10	Six species	[64]
6	$\frac{S_T}{S_L^0} \sim \text{Le}_{\text{eff}}^{-0.82} \left(\frac{u'}{S_L^0}\right)^{0.45} \left(\frac{P}{P^0}\right)^{0.75} \left(\frac{T}{T^0}\right)^{-1.33} \left(\frac{l_t}{\delta_L^0}\right)^{-0.41}$	523, 623	~20	Hydrogen, syngas	[29]
7	$\frac{S_T}{S_L^0} \sim \left(\frac{u'}{S_L^0}\right)^{0.61} \left(\frac{l_t}{\delta_L^0}\right)^{0.39}$	300, 423	~5	Methane	[67]



While some studies (i.e., no. 4 and no. 5 in Table 4.2) seem to exclude the pressure effect at a glance, the related term can be found by inspecting the individual factors. For instance, since kinematic viscosity  $\nu$  is proportional to the product of the Zel'dovich flame thickness and the planar laminar flame speed,  $\delta_L^0 \cdot S_L^0$ , with constant Prandtl number, the expression in [66] accordingly comprises the Zel'dovich flame thickness, and hence, the pressure effect. Similarly, the expression in [64] includes the pressure effect with Markstein length  $L_b$  since the value of  $L_b$  is determined by the product of Markstein number and the Zel'dovich flame thickness.

Meanwhile, several studies have suggested the rationales behind the pressure effect. One possible reason is the increase in hydrodynamic instability (or Darrieus-Landau instability [72, 73]) with an increase in pressure. According to the theory of hydrodynamic instability, the characteristic length scale of the flame instability, where the wavelength is at the limit of flame instability, is lowered as the pressure increases due to its relevance with the flame thicknesses [112, 113]. Moreover, in a numerical study conducted by Attili et al. [113], this scale decreased more rapidly than theoretically expected as the pressure increased. In that respect, several studies have claimed that the pressure effect at turbulent flame speed attributes to hydrodynamic instability [59, 61, 69].

However, the effect of hydrodynamic instability on turbulent flame speed has not been clarified and is a controversial issue to date. More specifically, some studies have revealed the minor influence of expansion ratio  $\sigma$ , which theoretically has a significant influence on hydrodynamic instability, on the turbulent flame speed at moderate [65] and intense [114] turbulence conditions via numerical analysis. More recently, this effect was questioned in an experimental study conducted by Lipatnikov et al. [76], wherein the expansion ratio exhibited a weak effect on

turbulent flame speed even at low turbulence conditions. That is, the hydrodynamic instability could be of minor influence, if any, on turbulent flame speed. If it is true, the flame instability should not be considered as the cause for the pressure effect.

Another possibility for the pressure effect is the direct relevance of the laminar flame thickness with the inner cutoff. Due to the sudden rise in temperature across the flame, turbulent flows are subjected to high viscosity within the flame thickness, thereby nullifying the effect of small turbulence scales relative to the flame thickness on flame wrinkling. The laminar flame thickness can thus be a useful measure for the inner cutoff. Similarly, by postulating the flame thickness as an inner cutoff, Yu and Lipatnikov [63] suggested an expression for turbulent flame speed, given as  $S_T/S_L \sim (u'/S_L)^{0.5} (l_t/\delta_L^0)^{0.5}$ , in their numerical analysis.

Based on the discussion so far, the expression for a fully-developed turbulent flame speed is here introduced. By adopting the above concept of inner cutoff, the Zel'dovich flame thickness in the existing forms is replaced by the inner cutoff  $\varepsilon_c$ . It is worth noting that the Kolmogorov length scale  $\eta$  exhibits a strong pressure dependency [69], similar to  $\delta_L^0$ , to ensure the substitution of  $\varepsilon_c$  does not contradict the pressure effect. The expression is hence suggested as

$$\Xi_{\text{eq}} = \frac{A_T}{A_L} \Big|_{t \rightarrow \infty} = 1 + C_t \left( \frac{u'}{S_L^0} \right)^{C_1} \left( \frac{l_t}{\varepsilon_c} \right)^{C_2}, \quad (4.40)$$

where  $C_t$ ,  $C_1$ , and  $C_2$  are the validation constants.

To select appropriate exponents values  $C_1$  and  $C_2$ , each set  $(C_1, C_2)$  was determined in a two-dimensional domain and swept with an interval of 0.1. The explored ranges are  $0.6 \leq C_1 \leq 0.9$  and  $0.2 \leq C_2 \leq 0.6$ . As the flame surface

tends to approach the fully-developed state,  $\mathcal{E}_{\text{eq}}$  appreciably affects the evolution of wrinkling factor  $\mathcal{E}$  during simulation, particularly at the burn duration from 10–50%, hereinafter BD1050. Accordingly, the validation was performed by comparing the values of BD1050 obtained from the experiment and simulation results. For each prescribed set of exponents, one representative point of Engine A was used to match BD1050 within one percent deviation from the experimental value by determining the value of  $C_t$ . Note that only the stoichiometric points (a total of 194 points) were employed in this analysis due to the exceptional combustion features of the lean-burn points. This issue is further addressed later in this section.

For concise comparison, two representative outcomes of the simulation, the coefficient of determination  $R^2$  and the slope of the regression line, were considered in Fig. 4.9. The rightmost figure indicates one instance of the regression plot with  $(C_1, C_2)$  as  $(0.7, 0.3)$ . Above all, it should be underlined that the most appropriate value of  $C_2$ , associated with cutoff scales, in terms of  $R^2$  was within the range of 0.2–0.4, provided  $C_1$  is fixed. This behavior is of particular interest to the author in that it is analogous to the “fractal model.”

The fractal model predicts the wrinkled flame surface based on the fractal nature of the flame morphology, as discussed elsewhere [29-35]. More precisely, it presumes the recursive self-similarity of the flame geometry within the length scales ranging between the outer and inner cutoffs. In the context of the fractal model, the general expression for the wrinkled flame surface is given as

$$A_T = A_L \left( \frac{\mathcal{E}_O}{\mathcal{E}_C} \right)^{D_3-2}, \quad (4.41)$$

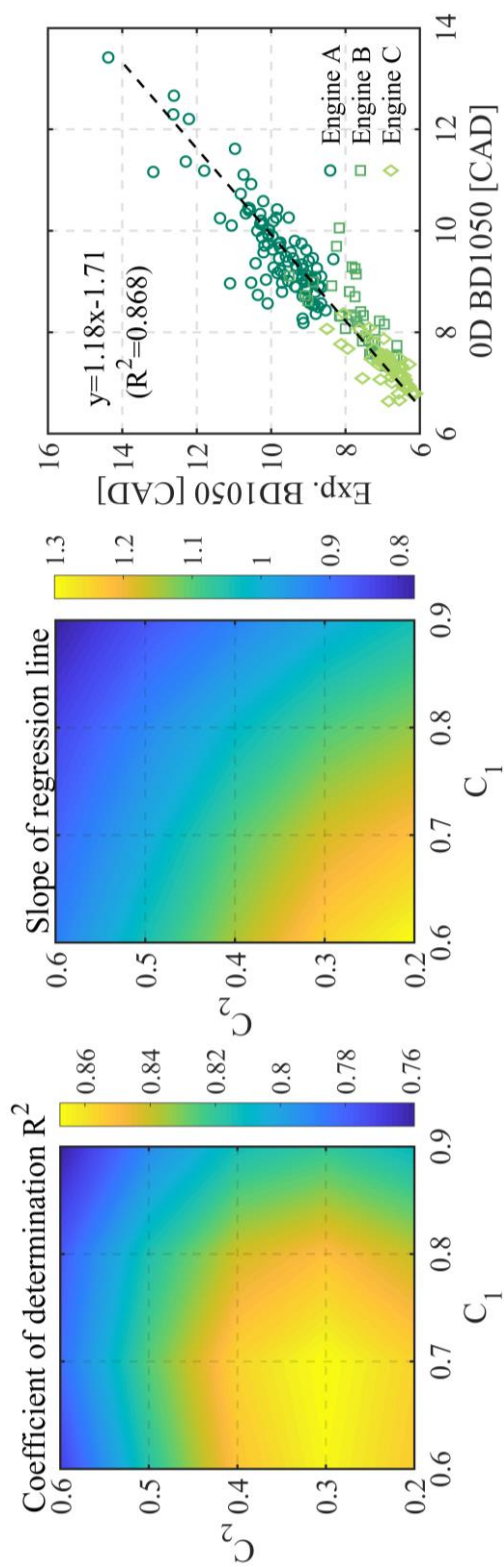


**Figure 4.9** Coefficient of determination (leftmost) and the slope of regression lines (middle) from the simulation results of stoichiometric points at different sets of  $(C_1, C_2)$ . The rightmost figure shows the one instance:  $(C_1, C_2) = (0.7, 0.3)$ .

where  $\varepsilon_o$  and  $D_3$  are the outer cutoff scale and three-dimensional fractal dimension, respectively. It is worth noting that Eq. (4.41) exhibits a similar structure with the term  $l_t/\varepsilon_c$  in Eq. (4.40) when the integral length scale  $l_t$  is equivalent to the outer cutoff scale. Most importantly, the reported values of the exponent ( $D_3 - 2$ ) (or in a two-dimensional analysis, ( $D_2 - 1$ )) in the literature [29-34] range typically from 0.2–0.5, despite a wider range being reported at extremely high Ka conditions [35]. Therefore, it is highlighted that the previous analysis of  $C_2$  is consistent with the fractal analysis.

However, for the lean-burn points, relatively high inaccuracies were observed between the predicted and experimental BD1050 while applying the closure form in Eq. (40), thereby indicating an unaccounted factor for flame wrinkling. Provided the characteristics at different combustion regimes are well reflected in the previous analysis, a notable difference is virtually in the burned gas temperature of the lean-burn points and stoichiometric points, wherein the calculated burned gas temperature of the lean-burn and stoichiometric points range from 1930–2140 K and 2440–2780 K during BD1050, respectively. This could be a possible unaccounted factor that affects flame wrinkling. Besides, several studies have addressed temperature as a factor that influences the turbulent flame speed.

As seen in Table 4.2, two studies [29, 59] proposed a strong negative correlation of turbulent flame speed with the unburned gas temperature. While Daniele et al. [59] did not discuss any explicit cause for the correlation, Lin et al [29] explained it as the different extent of hydrodynamic instability due to changes in the laminar flame speed with temperature. Furthermore, Jiang et al. [67] suggested two different closure forms for the unburned gas temperatures of 300 K and 423 K, considering they observed an obvious decrease in the normalized turbulent flame speed ( $S_T/S_L^0$ )

at the higher temperature. They explained this behavior with weakened hydrodynamic instability based on the lowered density ratio  $\sigma$  at the higher temperature. However, as discussed previously, the effect of hydrodynamic instability has not been clarified to date.

In contrast, Lapointe and Blanquart [111] performed numerical simulations using two different unburned gas temperatures, 298 K and 800 K. Therein, large differences of Karlovitz number at the reaction zone were observed by varying unburned gas temperature with a fixed velocity ratio  $u'/S_L^0$  and length ratio  $l_t/\delta_L$ , while the Karlovitz number at unburned gas remained unchanged. They further stated that the turbulences of small scales are beneficial for penetrating the reaction zone at higher unburned gas temperature due to the reduction of viscosity ratio across the flame, resulting in a higher Karlovitz number at the reaction zone. More precisely, it was shown that the decrease in viscosity change within the flame thickness leads to an increase in the flame surface at the reaction zone, indicating a higher Karlovitz number. Therefore, in their study, the viscosity within the flame thickness was highlighted as the factor that affected the stretch efficiency of turbulence.

Considering the rationale behind the determination of inner cutoff as the laminar flame thickness, the viscosity across the flame plays a dominant role in flame wrinkling. Then, the degree of viscosity, in addition to the length of laminar flame thickness subjected to high viscosity, can influence the stretch efficiency of turbulence at the reaction zone. This proposition can also clarify the reason for the negative correlation of turbulent flame speed with the unburned gas temperature. That is, due to the increase in viscosity, the flame is subjected to weaker turbulence at higher temperatures, thereby lowering the turbulent flame speed.

Moreover, an obvious correlation was observed between  $\mathcal{E}_{eq}$  and the arithmetic mean of unburned and burned zone temperatures, hereinafter referred to as the preheat zone temperature, based on the simulation results of BD1050. Note that the strongest correlation was observed with the preheat zone temperature rather than the unburned or burned zone temperatures, and their comparisons are not presented here for brevity.

In order to identify the aforesaid correlation, an instance of BD1050 obtained from the experiment and simulation results is presented in Fig. 4.10. The averaged value of preheat zone temperature during BD1050 is indicated by colored markers in the figure. The simulation was performed using identical values for  $C_t$ ,  $C_1$ , and  $C_2$  as in the previous example in Fig. 4.9 (see the rightmost figure). The relatively longer OD burn durations at lower temperatures in Fig. 4.10 indicate that the turbulent flame speed is underestimated at lower preheat zone temperatures, thereby implying the underestimation of  $\mathcal{E}_{eq}$  by Eq. (4.40). It is worth noting that this propensity is noticeable in the stoichiometric points as well, although less

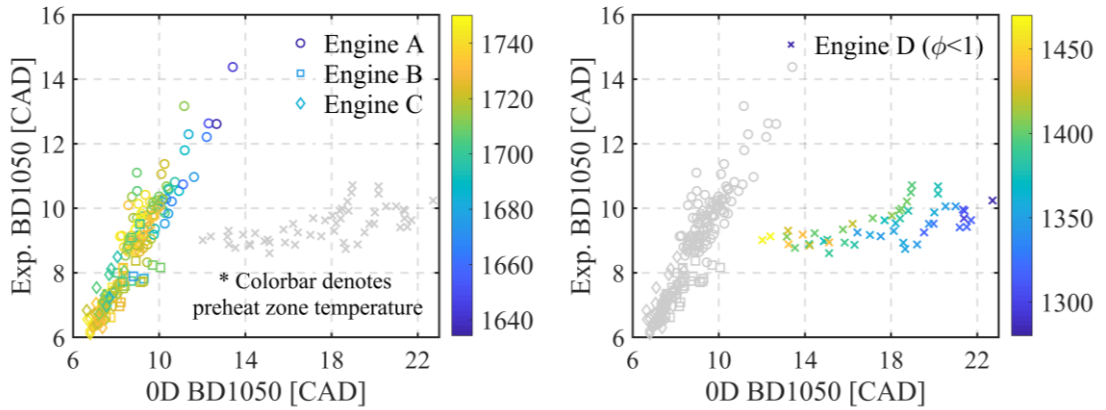


**Figure 4.10** Comparison of BD1050s obtained from the experiment and simulation results. The right and left figures show the stoichiometric and lean-burn points, respectively.

pronounced compared to the lean-burn points. The largely scattered data of Engine D evidently shows high prediction inaccuracy of the lean-burn points with Eq. (4.40).

Under those circumstances, the temperature term is additionally included in Eq. (4.40) using the power-law correlation similar to the existing closure forms. The expression for the wrinkling factor at equilibrium state  $\mathcal{E}_{\text{eq}}$  is finally recast as

$$\mathcal{E}_{\text{eq}} = \left. \frac{A_T}{A_L} \right|_{t \rightarrow \infty} = 1 + C_t \left( \frac{u'}{S_L^0} \right)^{C_1} \left( \frac{l_t}{\varepsilon_c} \right)^{C_2} \left( \frac{T^0}{T_{\text{ph}}} \right)^{C_3}, \quad (4.42)$$

where  $T_{\text{ph}}$  denotes preheat zone temperature defined as  $T_{\text{ph}} \equiv (T_u + T_b)/2$  and  $C_3$  is the validation constant associated with the temperature. The reference value of temperature  $T^0$  is set as 298.15 K.

Subsequently, the proper set of the three exponents is selected and proposed herein. To avoid unnecessary computation, only two values of  $C_2$  were explored, 0.3 and 0.4, which were previously considered to be reasonable. The explored ranges of  $C_1$  and  $C_3$  are  $0.6 \leq C_1 \leq 0.9$  and  $1.6 \leq C_3 \leq 2.8$ . Note that all operating points, including the lean-burn points, were exploited in this analysis.

Figure 4.11 shows the coefficient of determination  $R^2$  at each set of exponents. The point of highest  $R^2$  at  $C_2 = 0.3$  was found to be located at  $(C_1, C_3) = (0.8, 2.2)$  whereas the point at  $C_2 = 0.4$  was located at  $(C_1, C_3) = (0.8, 2.0)$ . Both points showed identical values of  $R^2$  as 0.851. Nonetheless, for the regression line slope, the highest  $R^2$  point at  $C_2 = 0.4$  exhibited a slope closer to unity compared to the point at  $C_2 = 0.3$ . As such, the set of three exponents  $(C_1, C_2, C_3)$  was finally determined as  $(0.8, 0.4, 2.0)$  with  $C_t$  as 213. Figure 4.12 shows the comparison of BD1050s with the simulation results using the determined set of



exponents, indicating the improved prediction of the lean-burn points compared to that in Fig. 4.10.

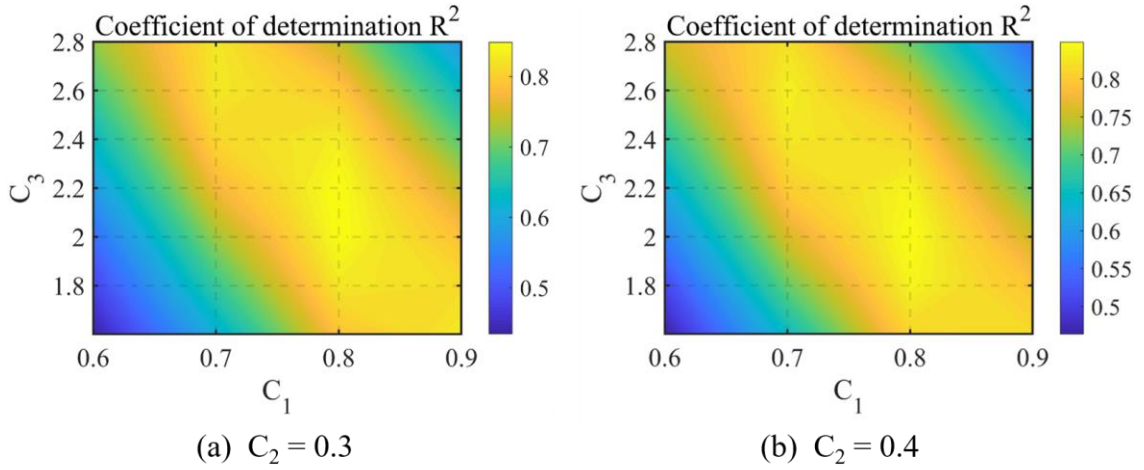


**Figure 4.11** Coefficient of determinations at different sets of validation constants ( $C_1$ ,  $C_3$ ).

The value of  $C_2$  is fixed at 0.3 and 0.4 in (a) and (b), respectively.

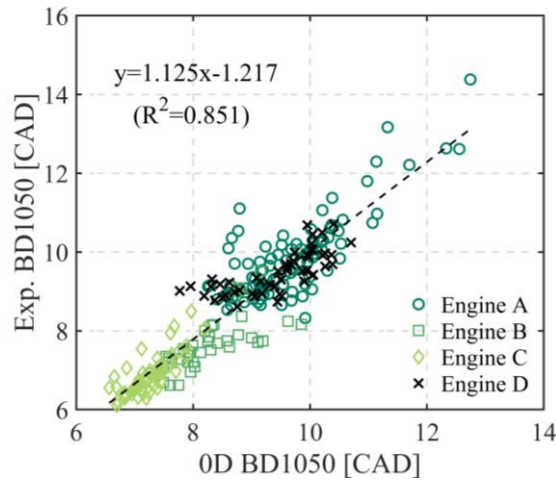


**Figure 4.12** Comparison of BD1050s obtained from the experiment and simulation results using exponents ( $C_1$ ,  $C_2$ ,  $C_3$ ) as (0.8, 0.4, 2.0).

### 4.3.3. Transition of the inner cutoff

Throughout this study, several roles of inner cutoff in the combustion phenomena have been discussed. Particularly, the inner cutoff adjusts the efficiency of turbulence by determining the integrated straining efficiency  $\Gamma$  in Section 3.2.2. Moreover, it is crucial for determining the equilibrium value of the wrinkling factor in Section 4.3.2. As such, the transition of the inner cutoff in Eq. (4.26) could be an important concern to evaluate the model.

Therefore, in order to identify the transition, the values of  $\delta_L$  and  $8\eta$  are compared, as shown in Fig. 4.13. It is readily seen that at the ignition timing, the value of  $\delta_L$  is greater than that of  $8\eta$  at all operating points. Furthermore, the transition from  $\delta_L$  to  $8\eta$  marginally occurs during BD0010, indicating the dominant role of the flame thickness in the early flame development period. Subsequently, the transition occurs rapidly during BD1050 in the stoichiometric points (Engine A-C), showing a predominant effect of  $\eta$  over  $\delta_L$ . However, the transition in lean-burn points (Engine D) seldom occurs between MFB00 and MFB50 due to the relatively lengthier  $\delta_L$  compared to the stoichiometric points.

Provided the evolution of thermodynamic states have an insignificant influence on the relative sizes of  $\delta_L$  and  $\eta$ , the major cause for transition is the decrease in turbulent intensity that is in contact with the flamelet during combustion, considering the decrease of turbulence increases  $\eta$ . This can be attributed to the natural decay of turbulence with time, and it is reproduced with the decay of cylinder-averaged turbulent intensity  $u'$  during simulation. Furthermore, the flamelet becomes exposed to weaker turbulence during flame propagation due to the distribution of turbulence, as discussed in Section 4.2.3. Based on these aspects, the transition from  $\delta_L$  to  $8\eta$  could be reproduced in the simulation during combustion.

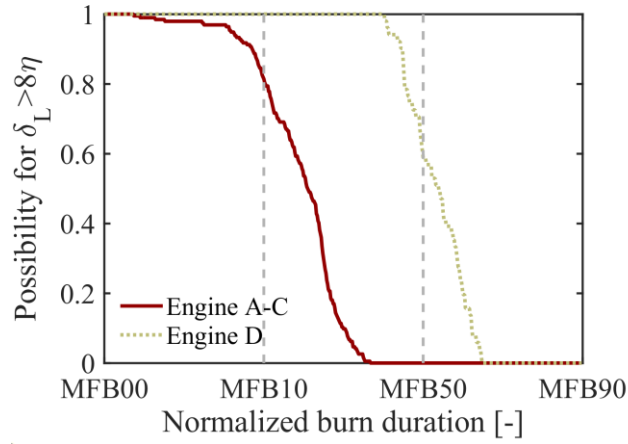


**Figure 4.13** Comparison of the  $\delta_L$  and  $8\eta$  values at all operating points considered in this study. The position in the abscissa indicates the relative timing during each burn duration period.

#### 4.4. Flame/wall interaction model

When a turbulent flame is in the vicinity of a cold wall, it exhibits distinct behaviors such as lowered flame speed and flame quenching from the freely propagating flame. Accordingly, three quenching mechanisms have been generally studied to elucidate the behaviors [115]: head-on quenching, side-wall quenching, and tube quenching. In SI engines, the interaction between a flame and cylinder liner, one of the representative cases of head-on quenching, critically affects the combustion characteristics due to the coolant in the vicinity of the liner. Therefore, herein, the wall interaction model between a flame and cylinder liner is exclusively dealt with in this study.

#### 4.4.1. Influence zone model

Due to the sudden increase in heat loss in the near-wall region, the propagating flame first experiences a lowered flame speed. When the flame approaches the wall, it eventually extinguishes, referred to as flame quenching. An exemplary picture of flame/wall interaction is illustrated in Fig. 4.14. The region where flame senses the presence of a cold wall with lowered propagation speed is referred to as the “influence zone,” whereas the region where the flame does not reach anymore is referred to as the “quenching zone.” Given that the objective of the proposed model is to reproduce turbulent flame speed near the wall, the modeling in this section focuses on predicting the length of the influence zone.

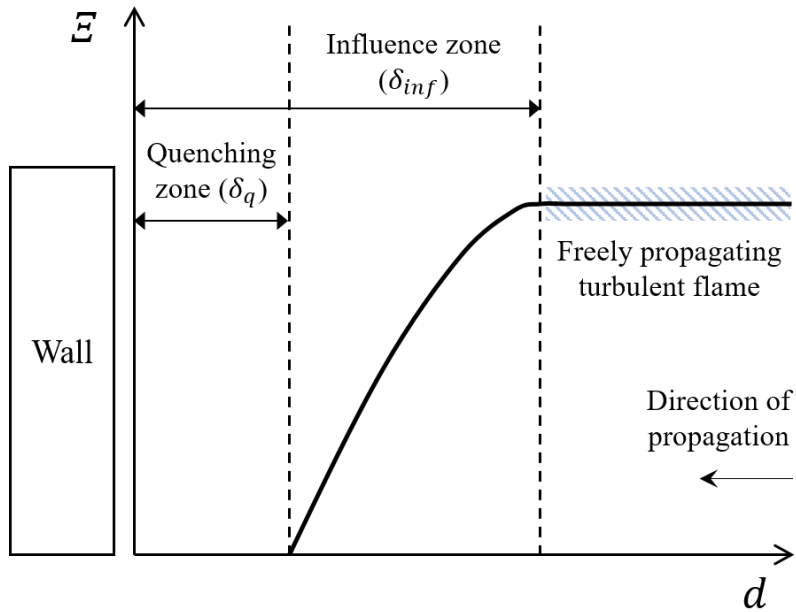


**Figure 4.14** Description of the flame/wall interaction. The wrinkling factor ( $\mathcal{E}$ ) is plotted alongside the distance from the wall ( $d$ ).

Since the lowered propagation speed significantly influences the latter part of combustion (accounting for 30–40% of the mass of unburned gas [21]), a variety of 0D models were proposed to reflect the flame behaviors at the influence zone. Bozza et al. [21] used the transition between the wall-combustion and fractal combustion modes to decrease the flame speed when the radial distance between flame and cylinder liner became less than the integral length scale. On the other hand, De Bellis et al. [17] used a similar transition but with different details in their fractal model. Furthermore, Demesoukas et al. [25] suggested a polynomial function that reduced the wrinkling factor within the influence zone in their FSD model. The quenching zone thickness  $\delta_q$  therein was reproduced based on its relation with pressure, i.e.,  $\delta_q \sim P^{-0.56}$ , whereas the influence zone thickness  $\delta_{inf}$  was set as a constant, 1.5 mm.

Most researches concerning the flame/wall interaction used the Peclet number  $Pe$ , defined as  $Pe \equiv d/\delta_L^0$ , for analysis, since the distances of the quenching and influence zones were comparable to the Zel'dovich flame thickness. Here,  $d$  stands for the distance from the wall. Based on this definition, the quenching and influence zone Peclet numbers are declared as  $Pe_q = \delta_q/\delta_L^0$ , and  $Pe_{inf} = \delta_{inf}/\delta_L^0$ , respectively. The results of those Peclet numbers in previous studies are briefly discussed below.

Poinsot et al. [115] numerically found that the Peclet numbers to be  $Pe_q = 3.4$  and  $Pe_{inf} \approx 8$ , and claimed that the quenching properties such as the quenching zone thickness and maximum wall heat fluxes of the turbulent cases remained in a similar order as those of the laminar case. In addition, Zhao et al. [116] numerically identified the values of Peclet numbers at the turbulent flame as  $Pe_q = 2.5$  and  $Pe_{inf} = 8$ .

Meanwhile, at the laminar condition, Boust et al. [117] derived the theoretical equation for the quenching zone Peclet number and validated the equation based on their experimental data. The proposed equation is determined as

$$\text{Pe}_q = \frac{1}{\varphi} - 1, \quad (4.43)$$

where

$$\varphi = Q_w/Q_\Sigma. \quad (4.44)$$

Here,  $Q_w$  is wall heat flux at quenching and  $Q_\Sigma$  is flame power, expressed as

$$Q_\Sigma = \rho_u S_L^0 y_f \Delta H_f, \quad (4.45)$$

where  $y_f$  and  $\Delta H_f$  are the mass fraction of fuel and heat of combustion, respectively.

However, in order to utilize Eqs. (4.43)-(4.45) in a 0D scheme, several assumptions were made for the modeling. First, although Eq. (4.43) was derived at a laminar condition, it was assumed that the equation was also capable of predicting turbulent flames. This assumption is supported by the finding made by Poinot et al. [115], which suggests similarities between the laminar and turbulence conditions. Second,  $\text{Pe}_{\text{inf}}$  was assumed to be proportional to  $\text{Pe}_q$  to determine the quantity of  $\delta_{\text{inf}}$  by applying the identical form of  $\text{Pe}_{\text{inf}}$  with  $\text{Pe}_q$  in Eq. (4.43). This could be plausible considering both quenching and lowered flame speed are caused by the

increased heat transfer near a cold wall. Lastly, it should be noted that the wall heat flux at quenching  $Q_w$  is an experimental value that is unavailable from the numerical simulations. The effect of  $Q_w$  was accordingly neglected, and  $Pe_q$  was assumed as the only function of flame power. Therefore, the model for the influence zone Peclet number  $Pe_{inf}$  can be simplified as

$$Pe_{inf} = Q_{\Sigma}/Q^0, \quad (4.46)$$

where  $Q^0$  is a validation constant. Therefore, this leads to

$$\delta_{inf} = \delta_L^0 \cdot Q_{\Sigma}/Q^0. \quad (4.47)$$

Subsequently, in order to replicate the behavior of a lowered flame speed, the wrinkling factor  $\mathcal{E}$  is decreased while the portion of the flame surface belongs to the influence zone. More specifically, when the flame surface is trapped in the influence zone, the wrinkling factor of the trapped surface is decreased by multiplying a prescribed factor  $C_{wrk}$  less than unity. The model accordingly developed is

$$A_L = A_{L,in} + C_{wrk}A_{L,out}. \quad (4.48)$$

To this end, the two validation constants,  $Q^0$  and  $C_{wrk}$ , were used in the flame/wall interaction model. Here,  $A_{L,in}$  and  $A_{L,out}$  are the inner and outer flame surfaces, respectively, separated by the demarcation between the influence and inner

zones, which satisfies the relation,  $A_L = A_{L,in} + A_{L,out}$ . The exemplary illustration is shown in Fig. 4.15.

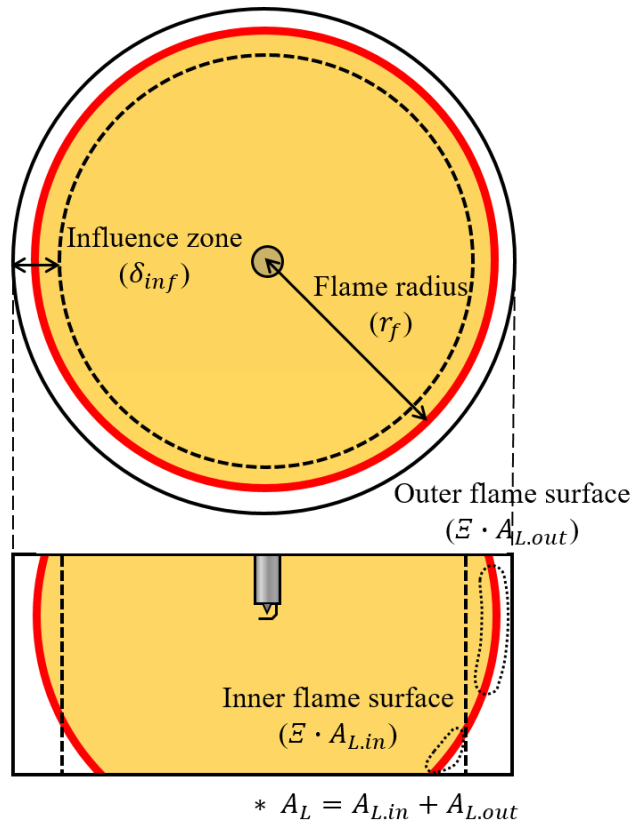


**Figure 4.15** Description of the outer and inner flame surfaces with the boundary of the influence zone.



#### 4.4.2. Hypothesis for the transient behaviors of flame thickness

As discussed in Section 4.4.1, the Zel'dovich flame thickness is of vital importance for evaluating the influence zone thickness. It was found that both the flame thickness and influence zone thickness were comparable in the experimental studies [115, 116], and can be correlated theoretically [117]. Considering this, the accurate estimation of Zel'dovich thickness is essential for the numerical simulations of premixed turbulent flame.

When evoking the strong correlation between the Zel'dovich flame thickness and pressure, the in-cylinder pressure could be a dominant factor for determining the influence zone thickness  $\delta_{inf}$ . Moreover, as the trapped mass within the influence zone accounts for approximately 30–40% of the in-cylinder mass, the burn duration from 50–90%, hereinafter BD5090, hence would be affected by the pressure as a consequence. That is, as the Zel'dovich flame thickness decreases with an increase in pressure, the cases with higher pressure would exhibit shorter BD5090 owing to the thinner  $\delta_{inf}$ .

Figure 4.16(a) shows the correlation between pressure and BD5090. Mass fraction burned (MFB) was used there to present the time of occurrence of mass ratio, which is the ratio of the burned gas to the total in-cylinder mass, during combustion. For instance, MFB50 is the time at which half of the reactant mass is burned. As combustion proceeds, the in-cylinder pressure essentially increases due to the expansion of the burned gas, thereby resulting in a higher pressure in the sequence of MFB00, MFB10, and MFB50 in the figure. All in all, the correlation with pressure

and BD5090 was identified clearly when using the pressure at ignition timing, i.e., MFB00, and gradually vanished when using the pressures obtained thereafter.

To clarify further, the combustion properties obtained from the simulation were used for the analysis. Considering the terms influencing  $\delta_{\text{inf}}$  in Eq. (4.47), the product of the flame power and the Zel'dovich flame thickness,  $Q_{\Sigma} \cdot \delta_L^0$ , were compared with BD5090 in Fig. 4.16(b). Note that the values of  $Q_{\Sigma}$  were acquired at MFB50 while the values of  $\delta_L^0$  were acquired at three different timings: MFB00,

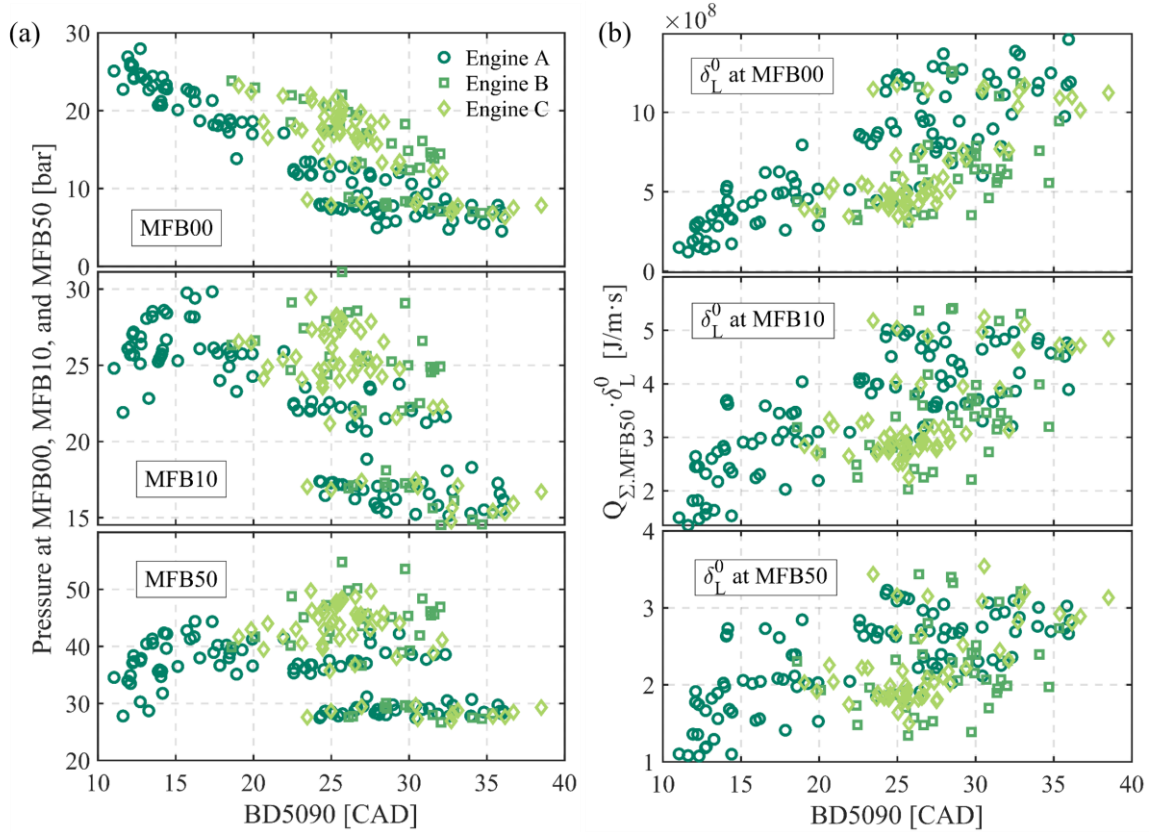


**Figure 4.16** Correlations with BD5090 and combustion properties. (a) Pressures obtained from experiments, (b) products of the flame power at MFB50 and the Zel'dovich flame thicknesses.

MFB10, and MFB50. Similar to the previous analysis, the results of this analysis showed more collapsed data when using the earlier value of  $\delta_L^0$ .

These results pose that the Zel'dovich flame thickness during BD5090 is better represented with the initial thickness at ignition timing than the later values. Therefore, it is hypothesized that the time scale of engine combustion is sufficiently shorter than that of the flame thickness evolution under dynamic thermodynamic conditions. In other words, the evolution of flame thickness according to thermodynamic states is not a quasi-equilibrium process during the engine combustion period and exhibits less change than theoretically expected. As there is no precedent research to verify the authenticity of the proposition, relevant work is expected to be conducted in the future.

However, there has been some evidence regarding the thinning and broadening of flame thickness due to the flame strain rate. Tamadonfar and Gülder [78] experimentally observed the thinner flame front as turbulence increased at the lean methane/air reactants, claiming the role of the strain rate as the thinning mechanism. They also found the broadened flame thicknesses at the flame fronts with large curvatures. Similarly, Wang et al. [79] numerically revealed the evolution mechanism of flame thickness by decomposing and analyzing its associated components and specified the reasons behind flame thinning and broadening as the tangential strain rate and the normal gradient of flame propagation speed at highly curved flame fronts, respectively.

Moreover, a numerical study conducted by Yu et al. [81] showed similar findings, which identified the flame strain rate and effects of flame propagation with curvatures as the mechanisms for flame thinning and broadening, respectively. Additionally, they revealed the transient time evolutions of the flame thickness from

an initial laminar state to a fully-developed turbulent state. Based on the observation of the evolution phase, flame thinning was found to be dominant during the early flame development period due to the high flame stretch rate. They further found that the re-broadening of flame thickness became dominant near the fully-developed state due to the increased counterbalancing effects against the stretch rate. It should be noted that those variances in flame thickness were realized within a relatively short flow time scale, indicating the immediate response from turbulence. Therefore, it is assumed that flame thinning is majorly attributed to the high flame strain rate during the flame development period, instead of the increase of in-cylinder pressure due to combustion.

However, inconsistency still persists between the previous studies associated with the behaviors of flame thickness. For instance, the flame stretch was revealed as the mechanism for flame broadening at the reactant having Lewis number above unity [118]. Since the inconsistency could stem from the diversities of experimental apparatus or the definition of flame thickness, a rigorous study would be required to verify the assumption raised in this study.

As for the evaluations on the inner cutoff scale in the previous modeling, e.g., the usage of the inner cutoff in Eq. (4.42), the existing approach is exploited to reproduce the flame thinning (i.e., thermodynamically quasi-equilibrium process for flame thickness) since there is no quantitative modeling for thinning due to the flame strain rate. In addition, as the reactant burns and expands progressively along with a sufficiently elevated flame strain rate, this method could qualitatively reproduce thinning due to the flame strain rate during the flame development period. Accordingly, only the Zel'dovich flame thickness in Eq. (4.47) was replaced by its value at ignition timing considering the hypothesis in this section, postulating the re-broadening of flame thickness near a wall. Therefore, Eq. (4.47) can be recast as

$$\delta_{\text{inf}} = \delta_{L,\text{ign}}^0 \cdot Q_{\Sigma}/Q^0, \quad (4.49)$$

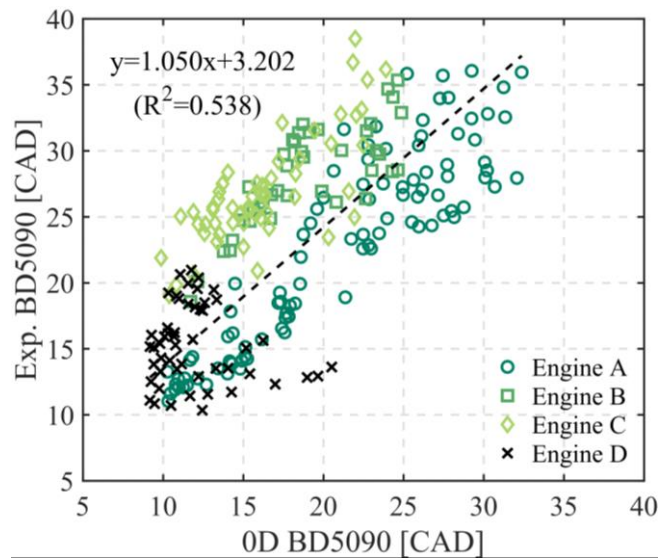
where  $\delta_{L,\text{ign}}^0$  is the Zel'dovich flame thickness at ignition timing.

Figure 4.17 shows the results of BD5090 by embedding all the models proposed in this study. As in the cases of BD0010 and BD1050, the representative point of Engine A was used to match BD5090 with its experimental value to ensure it was within one percent deviation by adjusting the validation constants,  $Q^0$  and  $C_{\text{wrk}}$ . The values of  $Q^0$  and  $C_{\text{wrk}}$  were thus determined as  $112 \cdot 10^3$  and 0.25, respectively. Although each point appeared to be more scattered in terms of  $R^2$  compared to the results of BD0010 and BD1050, several interesting behaviors were found from the acquired results.

First, the predictions of each engine in the stoichiometric points showed a strong agreement with the experimental values, thereby presenting the value of slope near unity. This indicates that the physics of flame/wall interactions were well reproduced in each engine. Second, although each set of stoichiometric points fit linearly with the experimental values, the predicted values of BD5090 were determined to be shorter than the experiment values, exhibiting the offsets with the regression line in the order of Engines A, B, and C. Considering these engines share almost identical specifications but different S/B ratios, it could be inferred that these engines exhibit different heat transfer characteristics, such as the wall temperature. Therefore, these offsets are speculated to be initiated from neglecting the wall heat flux at quenching related to the heat transfer at the cylinder wall.

Lastly, the result of the lean-burn points is analyzed. For the lean-burn points, the overall short burn durations were observed in both experiment and simulation

results. Although one might expect a large influence zone thickness when evoking the relatively large Zel'dovich flame thicknesses at the lean-burn points, the lowered flame powers due to the lean combustion prevailed over the effect of Zel'dovich flame thicknesses, thereby shortening both the influence zone thickness and BD5090. Further, it is worth noting that relatively large deviations between the experimental BD5090s and predicted values were identified compared to the stoichiometric points. The causes for the inaccuracies are supposed to be i) the alteration of flame thickness characteristics at high Karlovitz numbers or ii) insufficient re-broadening process due to the highly wrinkled flame surface.



**Figure 4.17** Comparison of BD5090s obtained from experimental and simulation results.

## 4.5. Result and discussion

Throughout this study, the proposed models have been validated based on the flame propagation speed during combustion, thereby successfully predicting burn durations. Figure 4.18 summarizes all burn duration results obtained so far. Although the results of BD0010 and BD5090 are identical to those presented in each modeling section, there exist slight differences in the result of BD1050 (compare Figs. 4.12 and 18(b)) due to the influence of flame/wall interaction in some exceptional cases.

In addition to the burn durations, several parameters can represent the engine performances. Therefore, in this section, the results of three additional engine performance parameters are presented: the net indicated thermal efficiency, indicated specific fuel consumption (ISFC), and the indicated mean effective pressure (IMEP). Prior to analyzing these parameters, the distinctive characteristics of the operating conditions at the stoichiometric and lean-burn points are first investigated.

In the case of stoichiometric points, the wider operating ranges of average intake pressure and valve timing were explored in the experiment. Additionally, a relatively large portion of the stoichiometric points was operated at the average intake pressure of less than 1 atm. Since the amount of the exhaust backflow during the valve overlap increases rapidly at the intake pressure below the ambient pressure, the stoichiometric points exhibited a broader range of residual mass fraction compared to that of the lean-burn points. Accordingly, the ranges of residual mass fraction calculated from the simulation at stoichiometric points and lean-burn points were 2 to 22% and 3 to 8%, respectively. This characteristic hints at the inaccuracies of performance parameters shown in Fig. 4.19.

For the net indicated thermal efficiency and ISFC, the lean-burn points were successfully predicted while the relatively dispersed results were shown at the stoichiometric points. These deviations could have been originated from the inaccurate predictions of the residual mass fraction. Indeed, reproducing the accurate transient mass transfer with open valves is a challenging problem in the 0D simulation, particularly severe at the points experiencing large amounts of exhaust backflow. As these discrepancies in residual mass fraction could result in inaccurate laminar flame speed values, the results of BD0010 and BD1050 at the stoichiometric points in Fig. 4.18 are more scattered compared to those at the lean-burn points. Due to the inaccurate prediction of work per fuel, the discrepancies thus lead to inaccurate results of net indicated thermal efficiency and ISFC. Conversely, the results of burn durations, in addition to the net indicated thermal efficiency and ISFC, are obtained satisfactorily at lean-burn points where the role of exhaust backflow is relatively minor.

As opposed to the aforesaid performance parameters, highly dispersed lean-burn points were observed in the IMEP result compared to the stoichiometric points. This can be attributed to the absence of pressure-time data at the lean-burn points, in contrast to the stoichiometric points. As the average intake pressure is used for the simulation input instead of the exact intake pressure profile, relatively large deviations of in-cylinder pressure at IVC timing were observed at the lean-burn points, resulting in inaccurate charging efficiencies. Therefore, the deviations of IMEP at the lean-burn points mainly indicate the extent of the inaccuracy of the gross indicated work attributed to the charging efficiency. Nonetheless, it is again noted that the values of the net indicated thermal efficiency and ISFC were successfully predicted since they utilize the value of the work per fuel mass.



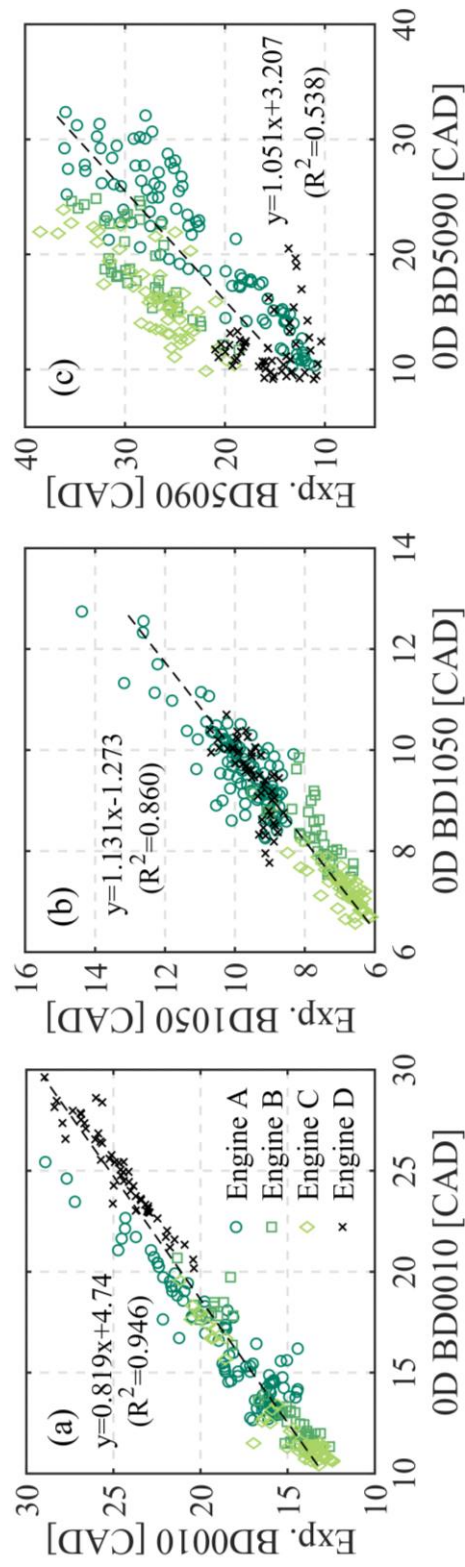


**Figure 4.18** Comparison of the experiment and simulation burn duration results. (a) BD0010, (b) BD1050, and (c) BD5090.

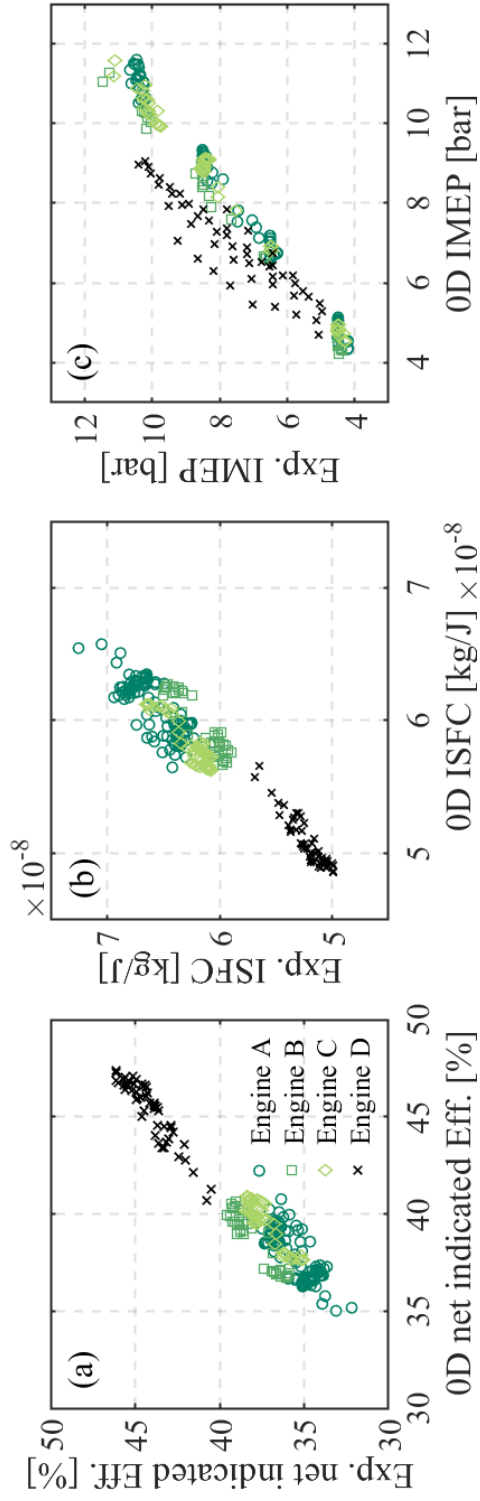


**Figure 4.19** Comparison of the engine performance parameters of the experimental and simulation results. (a) Net indicated thermal efficiency, (b) indicated specific fuel consumption, and (c) indicated mean effective pressure.

# Chapter 5. CRITICAL FACTORS FOR ENGINE COMBUSTION

In this chapter, the several combustion characteristics of SI engines are analyzed with the simulation applying the developed models in Chapters 3 and 4. In order to break down the combustion phenomena based on the flame development phases, the combustion periods are categorized into three parts: BD0010, BD1050, and BD5090, similar to the previous analysis. The independent analyses of the periods proceed in sequence accordingly.

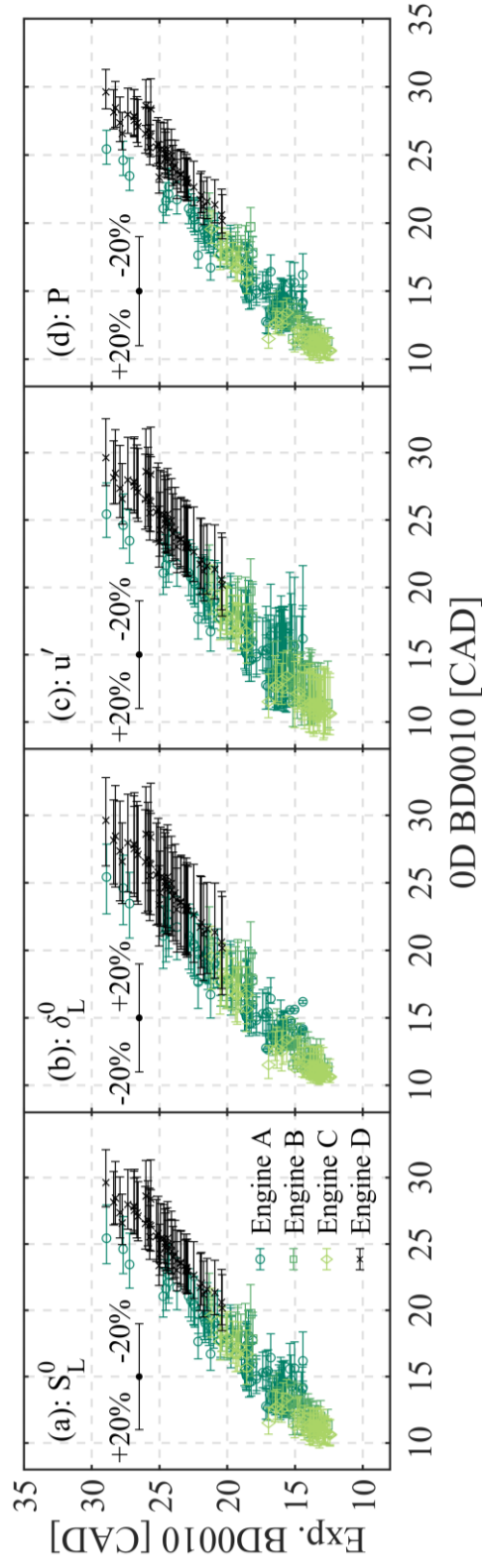
## 5.1. Influencing factors for BD0010

For the early flame development period, represented by BD0010, four factors are concerned in the analysis: planar laminar flame speed  $S_L^0$ , Zel'dovich flame thickness  $\delta_L^0$  (inner cutoff), turbulent intensity  $u'$ , and in-cylinder pressure  $P$ . It is worth noting that in addition to  $u'$ , the cutoff scales are critical for determining the extent of turbulence/flame interaction in that they adjust the efficiency of turbulence. Due to the importance of turbulence/flame interaction during the transitional phase (laminar to turbulent), the cutoff scales are of much significance to BD0010. In that respect, in contrast to the geometrically fixed outer cutoff, the inner cutoff that varies substantially based on the combustion environments are included in the analysis. Furthermore, as the increase in pressure can lower both  $S_L^0$  and  $\delta_L^0$ , the opposite effects for early flame propagation speed,  $P$  was included to identify their combined effect.

Subsequently, in order to quantify the effects of the individual factors, sensitivity analysis was conducted by changing the values of the abovementioned factors by 20%, i.e., 80% or 120% of their values. Although  $S_L^0$  is inversely proportional to  $\delta_L^0$  with a fixed thermal diffusivity, the change in  $S_L^0$  is manipulated so as not to influence the value of  $\delta_L^0$  in the simulation, and vice versa. Therefore, the sole effects of the factors can be identified. In terms of  $P$ , the higher or lower pressure are set arbitrary only when determining the properties associated with the flame propagation during combustion. That is, in all cases, the thermodynamic conditions are solved considering the unperturbed value of  $P$ .

Figure 5.1 shows the results of the sensitivity analysis. The marker indicates the result of the unperturbed values, whereas the edges of the error bar are determined by altering the variable by 20%. It is readily seen that all variables exhibit appreciable effects on BD0010. Meanwhile, the results of  $\delta_L^0$  are intriguing given its intense effect on the relatively longer BD0010 points at the stoichiometric and lean-burn points. It is worth noting the sensitivity of  $\delta_L^0$  is highly pronounced compared to that of  $S_L^0$  at all lean-burn points. It implies that, considering the case where  $S_L^0$  decreases and  $\delta_L^0$  accordingly increases at a fixed thermal diffusivity, the extent of increase in BD0010 is more attributed to the change of  $\delta_L^0$  rather than  $S_L^0$  at lean-burn operation, which in turn underlines the effect of  $\delta_L^0$  on early flame development period.

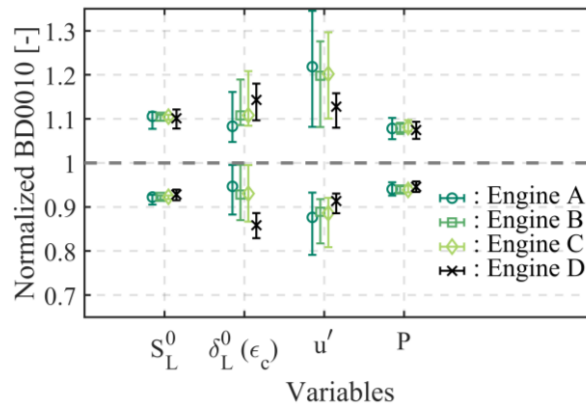
Furthermore, it was observed that an increase (or decrease) in the pressure functions as BD0010 decreased (or increased) in all operating points due to the predominant effect of  $\delta_L^0$  over  $S_L^0$ . That is, provided the rest of the conditions (e.g., residual mass and temperature) remain unchanged, BD0010 can be controlled by



**Figure 5.1** Sensitivity analysis of BD0010 with varying designated variables. (a)  $S_L^0$ , (b)  $\delta_L^0$ , (c)  $u'$ , and (d)  $P$ .

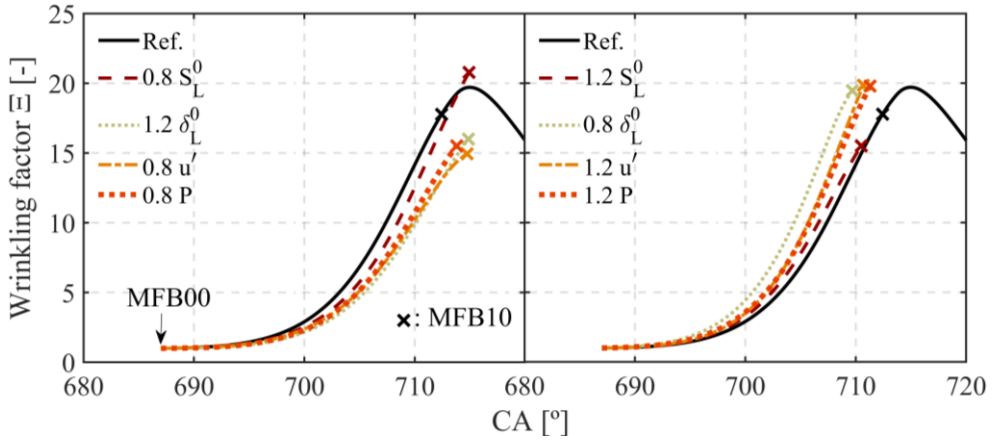
altering the in-cylinder pressure using engine technologies such as a turbocharger, CVVT, and variable compression ratio.

Figure 5.2 shows the results of normalized BD0010 at the unperturbed case. The error bars indicate the maximum and minimum values for the scattered range of the normalized values, whereas the markers indicate the average of normalized values. At the stoichiometric points (Engine A to C), the mean sensitivity of  $u'$  was most prominent, whereas the values of  $S_L^0$  and  $\delta_L^0$  were comparable. However, at the lean-burn points, the mean sensitivities of the variables were intense in the order of  $\delta_L^0$ ,  $u'$ , and  $S_L^0$ . These results are of particular interest to the author in that they pose an entirely new perspective on combustion in SI engines. This is because the conventional wisdom of SI engines concern only two parameters for early flame propagation, i.e.,  $u'$  and  $S_L^0$ . However, owing to the sensitivity analysis, the effects of the combustion parameters on the early flame development were quantified, thereby revealing the importance of inner cutoff, which has a comparable and occasionally predominant effect over  $S_L^0$ .



**Figure 5.2** Normalized BD0010 at the unperturbed case obtained through the sensitivity analysis of four different variables.

In order to comprehend the effects of those factors in detail, one instance of the evolution of the wrinkling factor  $\Xi$  is presented in Fig. 5.3. As discussed earlier, the effects of  $\delta_L^0$ ,  $u'$ , and  $P$  are similar to each other in that they adjust the extent of turbulence/flame interaction. More precisely, while  $\delta_L^0$  and  $P$  are involved in the range of effective turbulence scales on flame wrinkling,  $u'$  is involved in the intensity of turbulence. Similar evolutions of  $\Xi$  with these three parameters were thus observed in the figure, which altered the speed of the wrinkling process. Conversely, in cases with varying  $S_L^0$ , a relatively minor discrepancy was observed in the evolution of  $\Xi$  compared to the reference case due to the weak influence of varying  $S_L^0$  on flame wrinkling. Therefore, this result qualitatively demonstrates the discrete effects of the examined parameters on early flame development.



**Figure 5.3** One instance for the evolution of wrinkling factor during BD0010 with varying  $S_L^0$ ,  $\delta_L^0$ ,  $u'$ , and  $P$  factors. The left and right figures show the variations resulting in enhanced and lowered flame propagation speeds, respectively.

## 5.2. Additional analysis for BD1050 and BD5090

In Section 4.3.2, several factors such as velocity ratio  $u'/S_L^0$ , length ratio  $l_t/\varepsilon_c$ , and preheat zone temperature  $T_{ph}$ , as in Eq. (4.42), are inspected for influencing flame wrinkling. Next, the question is to what extent does the wrinkling factor  $\Xi$  approach the value of  $\Xi_{eq}$ . That is, provided the evolution of  $\Xi$  is closely correlated to  $\Xi_{eq}$ , the factors affecting  $\Xi_{eq}$  should be of direct importance for BD1050.

Figure 5.4(a) shows the normalized values of  $\Xi$  by their equilibrium values  $\Xi_{eq}$ . It can be seen that all cases of Engine A exhibit similar profiles concerning the average profile. More precisely, the normalized values during BD1050 lie in the range  $0.5 < \Xi/\Xi_{eq} < 0.7$ , without exhibiting a large deviation. Considering the maximum values of  $\Xi_{eq}$  during BD1050, ranging from 20.6–36.9 in all cases of

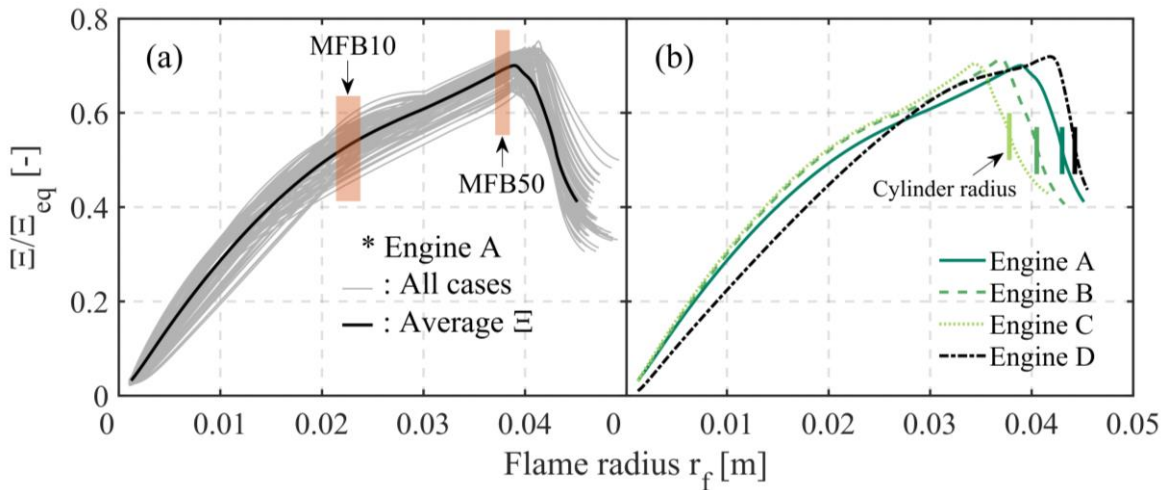


**Figure 5.4** Normalized wrinkling factors by their equilibrium values with the flame radius as the abscissa. (a) All cases of Engine A and their average profile, and (b) average profiles of normalized wrinkling factors.



Engine A, the deviations of  $\mathcal{E}/\mathcal{E}_{eq}$  were insignificant, indicating the strong correlation or attraction of  $\mathcal{E}$  to  $\mathcal{E}_{eq}$ .

It is worth noting that the maximum values of  $\mathcal{E}_{eq}$  in Engine D (lean-burn points) during BD1050 were between 69.4–142.3, which is thrice that of the stoichiometric points. Considering the largely dispersed values of  $\mathcal{E}_{eq}$  in Engine D, the average profile, shown in Fig. 5.4(b), follows closely with the other profiles. Therefore, it can be concluded that the factors discussed in Section 4.3.2 have dominant effects on BD1050 in the simulation, and the extent of their effects is related to the exponents in Eq. (4.42).

Additionally, the location of deflection points along the average profiles is noteworthy. These points are located in the vicinity of cylinder radii and show the influence of flame/wall interaction. Based on this finding, in conjunction with the locations of MFB10 and MFB50, it can be inferred that the flame/wall interaction has a minor influence on BD1050, which further proves the validity of the analysis performed in Section 4.3.2 without the flame/wall interaction model.

As stated earlier, as far as the formula derived by Boust et al. [117] is concerned, the factors influencing the flame/wall interaction or BD5090 are the Zel'dovich flame thickness  $\delta_L^0$ , flame power  $Q_{\mathcal{E}}$ , and the wall heat flux at quenching  $Q_w$ . Due to the difficulty of assessing  $Q_w$  in the numerical simulation,  $Q_{\mathcal{E}}$  and  $\delta_L^0$  are exclusively considered in the analysis, as shown in Eqs. (4.47) and (4.49).

Figure 5.5 shows the Zel'dovich flame thickness at the ignition timing  $\delta_{L,ign}^0$  and the average flame power during BD5090  $\bar{Q}_{\mathcal{E},BD5090}$  at all simulated points in this study. This figure quantitatively describes the distinctive characteristics of the lean-burn points as opposed to the stoichiometric points. For instance, it is readily

identified that the lean-burn points have 2–3 times lower flame powers compared to other points, which results in shorter BD5090s, albeit lengthier  $\delta_{L,ign}^0$ . In most cases, on the other hand, higher BD5090 is exhibited at points with higher  $\delta_{L,ign}^0$  at the stoichiometric points. Therefore, the operating strategies for the affecting parameters of  $\delta_{L,ign}^0$  (e.g., in-cylinder pressure and laminar flame speed) seem to be necessitated for controlling the thicknesses of the influence and quenching zones, and thus BD5090.

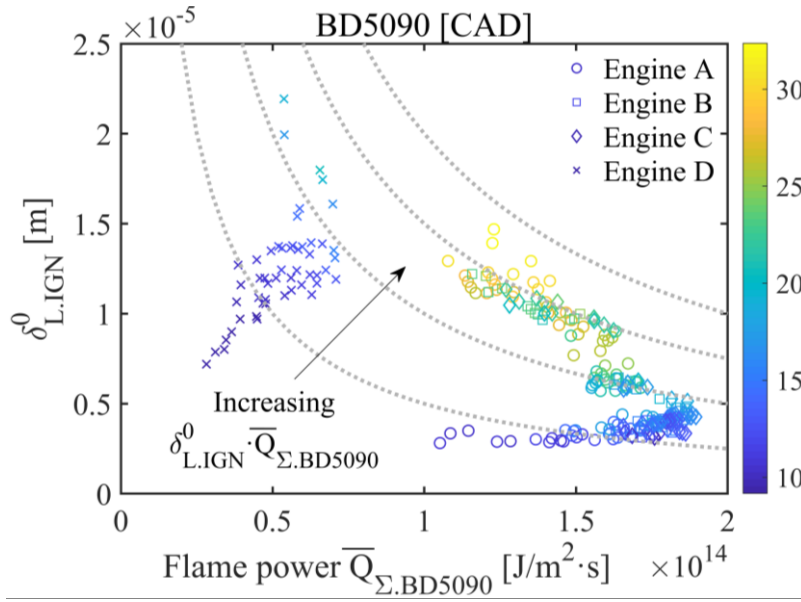


**Figure 5.5** Correlation of BD5090 with the Zel'dovich flame thickness at the ignition timing  $\delta_{L,ign}^0$  and the averaged flame power over BD5090  $\bar{Q}_{\Sigma,BD5090}$ . The dotted lines indicate the contours where the products of  $\delta_{L,ign}^0$  and  $\bar{Q}_{\Sigma,BD5090}$  have identical values.

## Chapter 6. CONCLUSION

This study primarily develops a comprehensive zero-dimensional (0D) model validated through numerous experimental data. The experimental data comprises an extensive range of operating points with four different engines using a continuously variable valve timing module; it also includes lean-burn points whose combustion characteristics differ significantly from the general stoichiometric points, thereby securing the generality of the proposed models.

The turbulence model includes an intake model, a turbulence production model, and a spinning up model, based on the proposed theory of tumble. The intake model reflects the intrinsic attributes, such as discharge coefficient and mass flux fractions at the valve curtain area, characterized by upstream geometries, e.g., port designs and intake valves. The turbulence production model is based on the previous study by Kim et al. [11] while undergoing some modifications on the correcting factor  $n$  and accordingly utilizes a three-dimensional (3D) virtual velocity vector field to reproduce the decaying rate of tumble energy at the designated cylinder geometry. Lastly, the spinning up model, which reproduces the increase in tumble energy during compression, is built upon the kinetic energy theory of tumble. Results showed that the proposed model was able to accurately predict a total of 25 cases, including valve strategies, engine geometries, and operating conditions, without modifying any validation constants. Therefore, the validity of the theory could be further proved in the hydrodynamic phenomena presented in RANS of 3D CFD.

The combustion model is principally based on the 0D flame surface density model proposed by Richard and Veynante [26]. As it is capable of adjusting the efficiencies of the respective turbulences at the specified length and velocity ratios,

the transient turbulence/flame interactions were successfully reproduced in the simulation. In terms of cutoff scales, the inner cutoff is determined by comparing the values of the laminar flame thickness and Kolmogorov length scale, i.e.,  $\varepsilon_c = \max(\delta_L, 8\eta)$ . On the other hand, the outer cutoff was set proportional to the flame radius. Therefore, the proposed model set the turbulence vortices whose sizes are smaller than the inner cutoff or larger than the outer cutoff ineffective for flame wrinkling, thus adjusting the efficiency of turbulence.

To evaluate total burning rates during flame propagation, independent modeling of strained laminar flame speed and the wrinkling factor at equilibrium state  $\mathcal{E}_{eq}$  ( $= (A_T/A_L)_{eq}$ ) was conducted. The formula for strained laminar flame speed was developed based on an experimental study conducted by Weiß et al. [62], and it is further complemented considering the flamelet characteristics of thin and distributed reaction zones proposed by Lapointe et al. [110]. However, a notable difference in the lean-burn points regarding the combustion regimes was not found within this modeling framework. Meanwhile, to determine  $\mathcal{E}_{eq}$ , the previous expressions of fully-developed turbulent flame speed and the analyses thereof are considered to elucidate the factors influencing the wrinkling process. By considering pressure effect and burned gas temperature as the factors, the burn durations of both the stoichiometric and lean-burn points were predicted accurately, thereby proposing the following expression:  $\mathcal{E}_{eq} \sim (u'/S_L^0)^{C_1} (l_t/\varepsilon_c)^{C_2} (T^0/T_{ph})^{C_3}$ .

Lastly, several analyses of the combustion phenomena were performed using a complete simulation with the developed models. First, the role of the inner cutoff during the early flame development period was revealed to be of great importance throughout the sensitivity analysis of BD0010. It was observed that the effect of the inner cutoff is occasionally predominant over that of the planar laminar flame speed

at the early flame development period, which is mostly true for the lean-burn points. Furthermore, the increase in in-cylinder pressure led to the decrease in BD0010 due to the dominant effect of laminar flame thickness over laminar flame speed. Regarding the wall interaction which significantly affects BD5090, the low flame power of the lean-burn points compared to the stoichiometric points was quantitatively demonstrated, thereby providing a possible rationale for a relatively short BD5090s. However, limiting the analysis to the stoichiometric points, a relatively longer BD5090 with a broader Zel'dovich flame thickness at ignition timing was observed, implying the importance of the Zel'dovich flame thickness on the flame/wall interaction.

From the author's viewpoint, there have been numerous modeling uncertainties within the numerical simulations of SI engines. As for 3D simulations, despite the remarkable development of computing power, it is still challenging to validate combustion models using an extensive range of experimental data available. Nonetheless, 3D simulations have become the most reliable numerical simulation for SI engines considering they are advantageous in solving local properties, such as the in-cylinder turbulence. Conversely, although 0D simulations have inherent difficulties in solving local turbulence, they exhibit an incomparably fast computing speed. By enhancing the prediction of turbulence, however, the powerful potentials of 0D simulation were realized in this study by validating the complete simulation with numerous experimental data. As a result, it became possible to analyze combustion phenomena through this 0D simulation, which was considered to be possible only through experiments and 3D simulations. Therefore, the author expects this study to shed light on the development of combustion models and to broaden our understanding of the combustion phenomena in SI engines.

## Bibliography

- [1] C. Borgnakke, V.S. Arpaci, R.J. Tabaczynski, A model for the instantaneous heat transfer and turbulence in a spark ignition engine, SAE Technical Paper, 1980.
- [2] T. Morel, N. Mansour, Modeling of turbulence in internal combustion engines, SAE Technical Paper, 1982.
- [3] S.H. Mansouri, J.B. Heywood, K. Radhakrishnan, Divided-Chamber Diesel Engine, Part I: A Cycle-Simulation which predicts performance and emissions, SAE Transactions (1982) 1101-1132.
- [4] S. Benjamin, A phenomenological model for 'barrel'swirl in reciprocating engines, Proceedings of the Institution of Mechanical Engineers, Part D: Journal of Automobile Engineering 206, (1992) 63-71.
- [5] S. Benjamin, Prediction of barrel swirl and turbulence in reciprocating engines using a phenomenological model, Experimental and predictive methods in engine research and development (1993).
- [6] M. Achuth, P.S. Mehta, Predictions of tumble and turbulence in four-valve pentroof spark ignition engines, Int. J. Engine Res. 2, (2001) 209-227.
- [7] D. Ramajo, A. Zanotti, N. Nigro, Assessment of a zero-dimensional model of tumble in four-valve high performance engine, International Journal of Numerical Methods for Heat & Fluid Flow 17, (2007) 770-787.
- [8] M. Kim, Y. Kim, J. Kim, H.H. Song, Development of quasi-dimensional turbulence model for spark-ignition engine with physical analysis of tumble: Energy-based tumble model focusing on energy intake and turbulence production, Appl. Energy 252, (2019) 113455.

- [9] S. Grasreiner, J. Neumann, C. Luttermann, M. Wensing, C. Hasse, A quasi-dimensional model of turbulence and global charge motion for spark ignition engines with fully variable valvetrains, *Int. J. Engine Res.* 15, (2014) 805-816.
- [10] N. Fogla, M. Bybee, M. Mirzaeian, F. Millo, S. Wahiduzzaman, Development of a K-k- $\epsilon$  Phenomenological Model to Predict In-Cylinder Turbulence, *SAE Int. J. Engines* 10, (2017) 562-575.
- [11] D. Won, A Study on Developing 0-dimensional Turbulence Model Considering Tumble Motion in a Spark-ignited Engine, Seoul National University, 2017.
- [12] F. Bozza, V. De Bellis, P. Giannattasio, L. Teodosio, L. Marchitto, Extension and validation of a 1D model applied to the analysis of a water injected turbocharged spark ignited engine at high loads and over a WLTP driving cycle, *SAE Int. J. Engines* 10, (2017) 2141-2153.
- [13] F. Bozza, L. Teodosio, V. De Bellis, S. Fontanesi, A. Iorio, Refinement of a 0D Turbulence Model to Predict Tumble and Turbulent Intensity in SI Engines. Part II: Model Concept, Validation and Discussion, *SAE Tech. Pap.* (2018).
- [14] Y. Kim, M. Kim, S. Oh, W. Shin, S. Cho, H.H. Song, A new physics-based modeling approach for a 0D turbulence model to reflect the intake port and chamber geometries and the corresponding flow structures in high-tumble spark-ignition engines, *Energies* 12, (2019) 1898.
- [15] M. Kim, H.H. Song, The study of the fundamental characteristics of tumble in a spark-ignition engine via numerical analysis, *SAE Technical Paper*, 2021.
- [16] N.C. Blizard, J.C. Keck, Experimental and theoretical investigation of turbulent burning model for internal combustion engines, *SAE Technical Paper*, 1974.

- [17] V. De Bellis, F. Bozza, D. Tufano, A comparison between two phenomenological combustion models applied to different si engines, SAE Technical Paper, 2017.
- [18] A. Irimescu, S.S. Merola, G. Valentino, Application of an entrainment turbulent combustion model with validation based on the distribution of chemical species in an optical spark ignition engine, *Appl. Energy* 162, (2016) 908-923.
- [19] T. Morel, C.I. Rackmil, R. Keribar, M.J. Jennings, Model for heat transfer and combustion in spark ignited engines and its comparison with experiments, *SAE transactions* (1988) 348-362.
- [20] R.J. Tabaczynski, C.R. Ferguson, K. Radhakrishnan, A turbulent entrainment model for spark-ignition engine combustion, *SAE transactions* (1977) 2414-2433.
- [21] F. Bozza, A. Gimelli, S.S. Merola, B. Vaglieco, Validation of a fractal combustion model through flame imaging, *SAE transactions* (2005) 973-987.
- [22] D.A. Santavicca, D. Liou, G.L. North, A fractal model of turbulent flame kernel growth, *SAE transactions* (1990) 90-98.
- [23] S. Bougrine, S. Richard, D. Veynante, Modelling and Simulation of the Combustion of Ethanol blended Fuels in a SI Engine using a 0D Coherent Flame Model, *SAE Technical Paper*, 2009.
- [24] S. Demesoukas, P. Brequigny, C. Caillol, F. Halter, C. Mounaïm-Rousselle, 0D modeling aspects of flame stretch in spark ignition engines and comparison with experimental results, *Appl. Energy* 179, (2016) 401-412.
- [25] S. Demesoukas, C. Caillol, P. Higelin, A. Boiarciuc, A. Floch, Near wall combustion modeling in spark ignition engines. Part A: Flame–wall interaction, *Energy Convers. Manag.* 106, (2015) 1426-1438.



- [26] S. Richard, D. Veynante, A 0-D flame wrinkling equation to describe the turbulent flame surface evolution in SI engines, *Comptes Rendus Mécanique* 343, (2015) 219-231.
- [27] I. Wiebe, Halbempirische formel für die Verbrennungs-Geschwindigkeit, verlag der Akademie der Wissenschaften der VdSSR, Moscow (1956).
- [28] G. Damköhler, Der einfluss der turbulenz auf die flammengeschwindigkeit in gasgemischen, *Z. Elektrochem. angew. phys. Chem.* 46, (1940) 601-626.
- [29] Y.-C. Lin, P. Jansohn, K. Boulouchos, Turbulent flame speed for hydrogen-rich fuel gases at gas turbine relevant conditions, *Int. J. Hydrog. Energy* 39, (2014) 20242-20254.
- [30] S. Daniele, J. Mantzaras, P. Jansohn, A. Denisov, K. Boulouchos, Flame front/turbulence interaction for syngas fuels in the thin reaction zones regime: turbulent and stretched laminar flame speeds at elevated pressures and temperatures, *J, Fluid Mech.* 724, (2013) 36-68.
- [31] F. Foucher, C. Mounaïm-Rousselle, Fractal approach to the evaluation of burning rates in the vicinity of the piston in a spark-ignition engine, *Combust. Flame* 143, (2005) 323-332.
- [32] Ö. Gülder, G.J. Smallwood, R. Wong, D. Snelling, R. Smith, B. Deschamps, J.-C. Sautet, Flame front surface characteristics in turbulent premixed propane/air combustion, *Combust. Flame* 120, (2000) 407-416.
- [33] Y. Shim, S. Tanaka, M. Tanahashi, T. Miyauchi, Local structure and fractal characteristics of H<sub>2</sub>–air turbulent premixed flame, *Proc. Combust. Inst.* 33, (2011) 1455-1462.

- [34] T. Kulkarni, F. Bisetti, Surface morphology and inner fractal cutoff scale of spherical turbulent premixed flames in decaying isotropic turbulence, *Proc. Combust. Inst.* 38, (2021) 2861-2868.
- [35] O. Chatakonda, E.R. Hawkes, A.J. Aspden, A.R. Kerstein, H. Kolla, J.H. Chen, On the fractal characteristics of low Damköhler number flames, *Combust. Flame* 160, (2013) 2422-2433.
- [36] N. Chakraborty, R. Cant, Turbulent Reynolds number dependence of flame surface density transport in the context of Reynolds averaged Navier–Stokes simulations, *Proc. Combust. Inst.* 34, (2013) 1347-1356.
- [37] F. Charlette, C. Meneveau, D. Veynante, A power-law flame wrinkling model for LES of premixed turbulent combustion Part II: dynamic formulation, *Combust. Flame* 131, (2002) 181-197.
- [38] O. Colin, F. Ducros, D. Veynante, T. Poinso, A thickened flame model for large eddy simulations of turbulent premixed combustion, *Phys. Fluids* 12, (2000) 1843-1863.
- [39] C. Meneveau, T. Poinso, Stretching and quenching of flamelets in premixed turbulent combustion, *Combust. Flame* 86, (1991) 311-332.
- [40] N. Hayashi, A. Sugiura, Y. Abe, K. Suzuki, Development of ignition technology for dilute combustion engines, *SAE Int. J. Engines* 10, (2017) 984-994.
- [41] D. Jung, K. Sasaki, K. Sugata, M. Matsuda, T. Yokomori, N. Iida, Combined effects of spark discharge pattern and tumble level on cycle-to-cycle variations of combustion at lean limits of SI engine operation, *SAE Technical Paper*, 2017.
- [42] K. Nakata, S. Nogawa, D. Takahashi, Y. Yoshihara, A. Kumagai, T. Suzuki, Engine technologies for achieving 45% thermal efficiency of SI engine, *SAE Int. J. Engines* 9, (2016) 179-192.

- [43] I. Bücker, D.-C. Karhoff, M. Klaas, W. Schröder, Engine in-cylinder flow control via variable intake valve timing, SAE Technical Paper 2013-24-0055, 2013.
- [44] T. Wang, D. Liu, B. Tan, G. Wang, Z. Peng, An investigation into in-cylinder tumble flow characteristics with variable valve lift in a gasoline engine, *Flow Turbul. Combust.* 94, (2015) 285-304.
- [45] T. Alger, M. Hall, R.D. Matthews, Effects of swirl and tumble on in-cylinder fuel distribution in a central injected DISI engine, SAE Technical Paper 2000-01-0533, 2000.
- [46] A.R.G.S. Raj, J.M. Mallikarjuna, V. Ganesan, Energy efficient piston configuration for effective air motion—A CFD study, *Appl. Energy* 102, (2013) 347-354.
- [47] C. Arcoumanis, Z. Hu, C. Vafidis, J. Whitelaw, Tumbling motion: a mechanism for turbulence enhancement in spark-ignition engines, *SAE transactions* 99, (1990) 375-391.
- [48] F. Zentgraf, E. Baum, B. Böhm, A. Dreizler, B. Peterson, On the turbulent flow in piston engines: Coupling of statistical theory quantities and instantaneous turbulence, *Phys. Fluids* 28, (2016) 045108.
- [49] M. Buschbeck, N. Bittner, T. Halfmann, S. Arndt, Dependence of combustion dynamics in a gasoline engine upon the in-cylinder flow field, determined by high-speed PIV, *Exp. Fluids* 53, (2012) 1701-1712.
- [50] M. Reeves, M.J. Haste, C.P. Garner, N.A. Halliwell, Barrel swirl breakdown in spark-ignition engines: Insights from particle image velocimetry measurements, *Proceedings of the Institution of Mechanical Engineers, Part D: Journal of Automobile Engineering* 213, (1999) 595-609.

- [51] R. Abdel-Gayed, D. Bradley, M. Hamid, M. Lawes, Lewis number effects on turbulent burning velocity, in Symposium (international) on combustion. (1985).
- [52] G.H. Markstein, Experimental and theoretical studies of flame-front stability, Journal of the Aeronautical Sciences 18, (1951) 199-209.
- [53] Z. Chen, On the extraction of laminar flame speed and Markstein length from outwardly propagating spherical flames, Combust. Flame 158, (2011) 291-300.
- [54] F. Halter, T. Tahtouh, C. Mounaïm-Rousselle, Nonlinear effects of stretch on the flame front propagation, Combust. Flame 157, (2010) 1825-1832.
- [55] A.P. Kelley, G. Jomaas, C.K. Law, Critical radius for sustained propagation of spark-ignited spherical flames, Combust. Flame 156, (2009) 1006-1013.
- [56] Z. Chen, Y. Ju, Theoretical analysis of the evolution from ignition kernel to flame ball and planar flame, Combustion Theory and Modelling 11, (2007) 427-453.
- [57] Z. Chen, M.P. Burke, Y. Ju, On the critical flame radius and minimum ignition energy for spherical flame initiation, Proc. Combust. Inst. 33, (2011) 1219-1226.
- [58] K. Eisazadeh-Far, F. Parsinejad, H. Metghalchi, J.C. Keck, On flame kernel formation and propagation in premixed gases, Combust. Flame 157, (2010) 2211-2221.
- [59] S. Daniele, P. Jansohn, J. Mantzaras, K. Boulouchos, Turbulent flame speed for syngas at gas turbine relevant conditions, Proc. Combust. Inst. 33, (2011) 2937-2944.

- [60] U. Ahmed, N. Chakraborty, M. Klein, Insights into the bending effect in premixed turbulent combustion using the flame surface density transport, *Combust. Sci. Technol.* 191, (2019) 898-920.
- [61] H. Kobayashi, K. Seyama, H. Hagiwara, Y. Ogami, Burning velocity correlation of methane/air turbulent premixed flames at high pressure and high temperature, *Proc. Combust. Inst.* 30, (2005) 827-834.
- [62] M. Weiß, N. Zarzalis, R. Suntz, Experimental study of Markstein number effects on laminar flamelet velocity in turbulent premixed flames, *Combust. Flame* 154, (2008) 671-691.
- [63] R. Yu, A.N. Lipatnikov, Direct numerical simulation study of statistically stationary propagation of a reaction wave in homogeneous turbulence, *Phys. Rev. E* 95, (2017) 063101.
- [64] S. Chaudhuri, F. Wu, C.K. Law, Scaling of turbulent flame speed for expanding flames with Markstein diffusion considerations, *Phys. Rev. E* 88, (2013) 033005.
- [65] N. Fogla, F. Creta, M. Matalon, The turbulent flame speed for low-to-moderate turbulence intensities: Hydrodynamic theory vs. experiments, *Combust. Flame* 175, (2017) 155-169.
- [66] D. Bradley, M. Lawes, K. Liu, M.S. Mansour, Measurements and correlations of turbulent burning velocities over wide ranges of fuels and elevated pressures, *Proc. Combust. Inst.* 34, (2013) 1519-1526.
- [67] L. Jiang, S. Shy, W. Li, H. Huang, M. Nguyen, High-temperature, high-pressure burning velocities of expanding turbulent premixed flames and their comparison with Bunsen-type flames, *Combust. Flame* 172, (2016) 173-182.

- [68] C. Liu, S. Shy, H. Chen, M. Peng, On interaction of centrally-ignited, outwardly-propagating premixed flames with fully-developed isotropic turbulence at elevated pressure, *Proc. Combust. Inst.* 33, (2011) 1293-1299.
- [69] C.-C. Liu, S.S. Shy, M.-W. Peng, C.-W. Chiu, Y.-C. Dong, High-pressure burning velocities measurements for centrally-ignited premixed methane/air flames interacting with intense near-isotropic turbulence at constant Reynolds numbers, *Combust. Flame* 159, (2012) 2608-2619.
- [70] H. Kobayashi, T. Kawahata, K. Seyama, T. Fujimari, J.-S. Kim, Relationship between the smallest scale of flame wrinkles and turbulence characteristics of high-pressure, high-temperature turbulent premixed flames, *Proc. Combust. Inst.* 29, (2002) 1793-1800.
- [71] Ö.L. Gülder, G.J. Smallwood, Inner cutoff scale of flame surface wrinkling in turbulent premixed flames, *Combust. Flame* 103, (1995) 107-114.
- [72] G. Darrieus, Propagation d'un front de flamme, *La Technique Moderne* 30, (1938) 18.
- [73] L. Landau, On the theory of slow combustion, *Acta Physicochim Urs* 19, (1944) 77-85.
- [74] C. Law, C. Sung, Structure, aerodynamics, and geometry of premixed flamelets, *Prog. Energy Combust. Sci.* 26, (2000) 459-505.
- [75] S.D. Tse, D. Zhu, C.K. Law, Morphology and burning rates of expanding spherical flames in H<sub>2</sub>/O<sub>2</sub>/inert mixtures up to 60 atmospheres, *Proc. Combust. Inst.* 28, (2000) 1793-1800.
- [76] A. Lipatnikov, W. Li, L. Jiang, S. Shy, Does density ratio significantly affect turbulent flame speed?, *Flow Turbul. Combust.* 98, (2017) 1153-1172.

- [77] A.W. Skiba, T.M. Wabel, J. Temme, J.F. Driscoll, Experimental assessment of premixed flames subjected to extreme turbulence, in 54th AIAA aerospace sciences meeting. (2016).
- [78] P. Tamadonfar, Ö.L. Gülder, Experimental investigation of the inner structure of premixed turbulent methane/air flames in the thin reaction zones regime, *Combust. Flame* 162, (2015) 115-128.
- [79] H. Wang, E.R. Hawkes, J.H. Chen, B. Zhou, Z. Li, M. Aldén, Direct numerical simulations of a high Karlovitz number laboratory premixed jet flame—an analysis of flame stretch and flame thickening, *J. Fluid Mech.* 815, (2017) 511-536.
- [80] Z. Wang, B. Zhou, S. Yu, C. Brackmann, Z. Li, M. Richter, M. Aldén, X.-S. Bai, Structure and burning velocity of turbulent premixed methane/air jet flames in thin-reaction zone and distributed reaction zone regimes, *Proc. Combust. Inst.* 37, (2019) 2537-2544.
- [81] R. Yu, T. Nillson, X.-S. Bai, A.N. Lipatnikov, Evolution of averaged local premixed flame thickness in a turbulent flow, *Combust. Flame* 207, (2019) 232-249.
- [82] B. Savard, G. Blanquart, An a priori model for the effective species Lewis numbers in premixed turbulent flames, *Combust. Flame* 161, (2014) 1547-1557.
- [83] B. Savard, G. Blanquart, Broken reaction zone and differential diffusion effects in high Karlovitz n-C<sub>7</sub>H<sub>16</sub> premixed turbulent flames, *Combust. Flame* 162, (2015) 2020-2033.
- [84] B. Savard, B. Bobbitt, G. Blanquart, Structure of a high Karlovitz n-C<sub>7</sub>H<sub>16</sub> premixed turbulent flame, *Proc. Combust. Inst.* 35, (2015) 1377-1384.

- [85] CONVERGE CFD Software (Version 2.4), Convergent Science, Inc., Madison, WI, 2018.
- [86] V. Yakhot, S. Orszag, S. Thangam, T. Gatski, C. Speziale, Development of turbulence models for shear flows by a double expansion technique, *Physics of Fluids A: Fluid Dynamics* 4, (1992) 1510-1520.
- [87] S. Das, J. Dent, Simulation of the mean flow in the cylinder of a motored 4-valved spark ignition engine, SAE Technical Paper 952384, 1995.
- [88] K.Y. Kang, J.H. Baek, LDV measurement and analysis of tumble formation and decay in a four-valve engine, *Experimental Thermal and Fluid Science* 11, (1995) 181-189.
- [89] Y. Li, H. Zhao, Z. Peng, N. Ladommatos, Analysis of tumble and swirl motions in a four-valve SI engine, *SAE Transactions* 110, (2001) 2226-2241.
- [90] X. Baby, A. Floch, Investigation of the in-cylinder tumble motion in a multi-valve engine: effect of the piston shape, SAE Technical Paper 971643, 1997.
- [91] Y. Kim, M. Kim, J. Kim, H.H. Song, Y. Park, D. Han, Predicting the Influences of Intake Port Geometry on the Tumble Generation and Turbulence Characteristics by Zero-Dimensional Spark Ignition Engine Model, SAE Tech. Pap. (2018).
- [92] N. Kim, I. Ko, K. Min, Development of a zero-dimensional turbulence model for a spark ignition engine, *Int. J. Engine Res.* 20, (2019) 441-451.
- [93] F. Mollo, S. Luisi, F. Borean, A. Stroppiana, Numerical and experimental investigation on combustion characteristics of a spark ignition engine with an early intake valve closing load control, *Fuel* 121, (2014) 298-310.



- [94] S. Oh, S. Cho, W. Shin, C. Song, E. Seol, K. Min, H.H. Song, B. Lee, J. Son, S. Woo, An experimental study on the effect of stroke-to-bore ratio of Atkinson DISI engines with variable valve timing, *SAE Int. J. Engines* 11, (2018) 1183-1194.
- [95] G. Woschni, A universally applicable equation for the instantaneous heat transfer coefficient in the internal combustion engine, *SAE Technical paper*, 1967.
- [96] M. Mehl, W.J. Pitz, C.K. Westbrook, H.J. Curran, Kinetic modeling of gasoline surrogate components and mixtures under engine conditions, *Proc. Combust. Inst.* 33, (2011) 193-200.
- [97] D. Lapalme, R. Lemaire, P. Seers, Assessment of the method for calculating the Lewis number of H<sub>2</sub>/CO/CH<sub>4</sub> mixtures and comparison with experimental results, *Int. J. Hydrog. Energy* 42, (2017) 8314-8328.
- [98] J. Bechtold, M. Matalon, The dependence of the Markstein length on stoichiometry, *Combust. Flame* 127, (2001) 1906-1913.
- [99] S. Jerzembeck, N. Peters, P. Pepiot-Desjardins, H. Pitsch, Laminar burning velocities at high pressure for primary reference fuels and gasoline: Experimental and numerical investigation, *Combust. Flame* 156, (2009) 292-301.
- [100] U. Müller, M. Bollig, N. Peters, Approximations for burning velocities and Markstein numbers for lean hydrocarbon and methanol flames, *Combust. Flame* 108, (1997) 349-356.
- [101] R. Amirante, E. Distaso, P. Tamburrano, R.D. Reitz, Laminar flame speed correlations for methane, ethane, propane and their mixtures, and natural gas

- and gasoline for spark-ignition engine simulations, *Int. J. Engine Res.* 18, (2017) 951-970.
- [102] A. Kelley, A. Smallbone, D. Zhu, C. Law, Laminar flame speeds of C5 to C8 n-alkanes at elevated pressures: Experimental determination, fuel similarity, and stretch sensitivity, *Proc. Combust. Inst.* 33, (2011) 963-970.
- [103] S. Hann, M. Grill, M. Bargende, Reaction Kinetics Calculations and Modeling of the Laminar Flame Speeds of Gasoline Fuels, SAE Technical Paper, 2018.
- [104] J.B. Heywood, Internal combustion engine fundamentals, McGraw-Hill Education, 2018.
- [105] R.J. Blint, The relationship of the laminar flame width to flame speed, *Combust. Sci. Technol.* 49, (1986) 79-92.
- [106] S. Bougrine, S. Richard, O. Colin, D. Veynante, Fuel composition effects on flame stretch in turbulent premixed combustion: Numerical analysis of flame-vortex interaction and formulation of a new efficiency function, *Flow Turbul. Combust.* 93, (2014) 259-281.
- [107] R. Abdel-Gayed, D. Bradley, M. Lawes, Turbulent burning velocities: a general correlation in terms of straining rates, *Proc. R. Soc. A* 414, (1987) 389-413.
- [108] P. Senecal, E. Pomraning, K. Richards, T. Briggs, C. Choi, R. McDavid, M. Patterson, Multi-dimensional modeling of direct-injection diesel spray liquid length and flame lift-off length using CFD and parallel detailed chemistry, *SAE transactions* (2003) 1331-1351.
- [109] D. Bradley, A. Lau, M. Lawes, F. Smith, Flame stretch rate as a determinant of turbulent burning velocity, *Philos. Trans. R. Soc. A* 338, (1992) 359-387.

- [110] S. Lapointe, B. Savard, G. Blanquart, Differential diffusion effects, distributed burning, and local extinctions in high Karlovitz premixed flames, *Combust. Flame* 162, (2015) 3341-3355.
- [111] S. Lapointe, G. Blanquart, Fuel and chemistry effects in high Karlovitz premixed turbulent flames, *Combust. Flame* 167, (2016) 294-307.
- [112] M. Matalon, The Darrieus–Landau instability of premixed flames, *Fluid Dyn. Res.* 50, (2018) 051412.
- [113] A. Attili, R. Lamioni, L. Berger, K. Kleinheinz, P.E. Lapenna, H. Pitsch, F. Creta, The effect of pressure on the hydrodynamic stability limit of premixed flames, *Proc. Combust. Inst.* 38, (2021) 1973-1981.
- [114] H. Kolla, N. Swaminathan, Influence of turbulent scalar mixing physics on premixed flame propagation, *Journal of Combustion* 2011, (2011).
- [115] T. Poinso, D.C. Haworth, G. Bruneaux, Direct simulation and modeling of flame-wall interaction for premixed turbulent combustion, *Combust. Flame* 95, (1993) 118-132.
- [116] P. Zhao, L. Wang, N. Chakraborty, Effects of the cold wall boundary on the flame structure and flame speed in premixed turbulent combustion, *Proc. Combust. Inst.* 38, (2021) 2967-2976.
- [117] B. Boust, J. Sotton, S. Labuda, M. Bellenoue, A thermal formulation for single-wall quenching of transient laminar flames, *Combust. Flame* 149, (2007) 286-294.
- [118] L. De Goeij, T. Plessing, R. Hermanns, N. Peters, Analysis of the flame thickness of turbulent flamelets in the thin reaction zones regime, *Proc. Combust. Inst.* 30, (2005) 859-866.

## 국문 초록

끊임없는 불꽃 점화 엔진 기술의 발전에도 불구하고 실린더 내부의 물리 현상들은 오늘날까지도 명확하게 밝혀지지 않았다. 현재까지 개발된 다양한 연소 기술들은 그러한 현상들에 대한 물리적 고찰을 더욱이 어렵게 하고 있다. 작금의 상황 속에서 불꽃 점화 엔진의 근본적인 거동을 기본으로 한 모델은 큰 중요성을 갖는다. 이러한 기초 물리성을 근간으로 한 시뮬레이션은 엔진 내부 현상의 이해를 확장시킬 수 있으며, 이를 토대로 엔진 설계나 운전 영역의 최적화 과정에 기여할 수 있다.

하지만 불꽃 점화 엔진의 수치 해석 시뮬레이션은 여전히 많은 불확실성을 내포하고 있다. 일례로 3 차원 시뮬레이션의 경우 놀랄만한 계산 속도의 개선에도 불구하고 넓은 운전 영역에서의 검증은 아직 어려운 실정이다. 반면 0 차원 시뮬레이션은 난류 예측이 가능하다는 전제 하에 빠른 계산 속도를 바탕으로 내부 모델들을 수많은 실험 데이터로 검증할 수 있다는 강력한 장점을 갖는다. 이에 본 연구는 선행 연구들의 직접 수치 시뮬레이션과 실험 결과를 통해 입증된 물리 기반 모델들을 0 차원 시뮬레이션에 접목하여 실린더 내부의 물리 현상을 파악하고자 한다. 본고는 총 세 부분으로 구성되며 난류 모델, 연소 모델, 엔진 연소 분석의 순서로 진행된다.

이 중 난류 모델은 텀블의 운동에너지 분석에 기반하여 만들어졌으며, 이는 기존의 각운동량 관점의 0 차원 난류 모델과는 확연히 다른 방식이다. 본문에서는 모델을 제시하기 앞서 텀블의 특성들에 대한 분석이 선행된다. 그런 다음, 해당 분석들을 토대로 다양한 흡기 매니폴드 형태를 반영할 수 있는 흡기 모델이 제안된다. 마지막으로

실린더 내부 난류에 지대한 영향을 미치는 텀블의 주요 특성인 vortex breakdown 과 spinning up 을 반영하는 모델들이 차례로 제안된다. 그리하여 본 연구에서는 어떠한 검증 상수의 변화 없이 엔진의 다양한 조건들에 대해 예측할 수 있는 물리 기반의 난류 모델을 구축할 수 있었다. 이 연구에서 살펴본 엔진 조건들은 흡기 밸브 전략, 엔진 디자인의 변화, 운전 조건의 변화 등이 있다.

한편, 연소 모델은 현재까지 여러 연구들에서 밝혀진 다양한 연소 현상들을 고려하고 있으며 그 현상들은 차등 확산 (differential diffusion), 화염의 불안정성 (flame instabilities), 컷오프 스케일 (cutoff scales), 분산 반응 (distributed reaction) 등이 있다. 또한 본 연구는 화염 구김의 다양한 인자들을 조사하여 난류 화염 속도의 새로운 표현식을 제시한다. 최종적으로 난류 모델과 연소 모델을 결합한 시뮬레이션은 네 개의 다른 형상의 엔진의 희박 연소를 포함한 총 245 개의 운전 지점의 연소를 성공적으로 예측한다. 더욱이 가변 밸브 타이밍 모듈을 이용함으로써 광범위한 열역학적 상태의 운전 지점들을 모델 검증에 사용할 수 있었다. 미연소 가스의 점화 시기에서, 압력과 계산된 온도는 각각 4.5 bar 에서 28.6 bar 그리고 559 K 에서 794 K 에 달한다.

마지막으로 위 시뮬레이션을 이용하여 엔진 연소에 대한 분석을 실시함으로써 이론 공연비 연소와 희박 연소의 몇 가지 독특한 특성을 추가적으로 알아본다. 해당 분석은 화염 전파 양상에 따라 세 가지 시기로 분류하여 개별적으로 진행되며 각 시기의 연소에 중요한 인자들에 대해 조사한다. 무엇보다도 본 연구는, 기존 통념과는 다르게, 초기 화염 전파에 영향을 미치는 주요 인자로 층류 화염 속도와 난류 강도 뿐만 아니라 내부 컷오프에 대해 알아보며, 그 영향이 층류 화염 속도와 비슷하거나 혹은 더 우세함을 밝힌다.